

Efficient digital beamforming for medical ultrasound imaging

Gao, Changqing

2008

Gao, C. (2008). Efficient digital beamforming for medical ultrasound imaging. Doctoral thesis, Nanyang Technological University, Singapore.

<https://hdl.handle.net/10356/3483>

<https://doi.org/10.32657/10356/3483>

Nanyang Technological University

Downloaded on 24 Aug 2022 15:55:19 SGT



**NANYANG
TECHNOLOGICAL
UNIVERSITY**

EFFICIENT DIGITAL BEAMFORMING FOR
MEDICAL ULTRASOUND IMAGING

GAO CHANGQING

**EFFICIENT DIGITAL BEAMFORMING FOR
MEDICAL ULTRASOUND IMAGING**

GAO CHANGQING

**SCHOOL OF ELECTRICAL & ELECTRONIC
ENGINEERING**

2008

2008

Efficient Digital Beamforming for Medical Ultrasound Imaging

Gao Changqing

School of Electrical & Electronic Engineering

A thesis submitted to the Nanyang Technological University
in fulfillment of the requirement for the degree of
Doctor of Philosophy

2008

Statement of Originality

I hereby certify that the content of this thesis is the result of work done by me and has not been submitted for a higher degree to any other University or Institution.

.....

Date

.....

Gao Changqing

ACKNOWLEDGEMENTS

First and foremost, I would like to express my gratitude to my supervisor, Associate Professor Wong Moon Chung Eddie. It has been a great pleasure to work under a kind and inspiring tutor. His constant encouragement and persistent patience throughout the entire course of this work have been a major incentive for me to make an extra effort.

I am also grateful to Associate Professor Koh Liang Mong for his particular help and stimulating suggestions in a wide variety of aspects.

I would like to thank Professor Yongmin Kim, Mr. Yang Mo Yoo, Mr. Anup Agarwal and Mr. Fabio K. Schneider at the University of Washington for their help and instructive discussion.

Gratitude is also due to Associate Professor Lam Ying Hung Yvonne, Assistant Professor Tiew Kei Tee, Ms. Yu Jianhong and my dear friends, Mr. Ong Biow Hiew, Mr. Zhang Lichen, Mr. Cao Ji, Mr. Zhang Fan, Mr. Vinay S. Sawant, Mr. Cheong Jia Hao, Mr. Song Pengyu. It is my pleasure to carry out this work in a research group with kind and cooperative team members.

Finally, I would like to give my special thanks to my mother, Liu Man. Her selfless affection and trust have enabled me to complete this work.

List of Symbols

$A_n(t)$	Echo envelope signal in the n-th channel
c	Sound speed
d_n	Delta-sigma modulator output
e_n	White noise source
$E(z)$	z-transform of the white noise source
$D(z)$	z-transform of the modulator output
f_0	Transducer center frequency
f_B	Ultrasound band width
f_{BF}	Beamforming frequency
f_{BFmin}	Minimum beamforming frequency
f_{eff}	Effective sampling frequency in interpolation beamforming
f_H	Upper band of the ultrasound signal
f_L	Lower band of the ultrasound signal
F_r	Frame rate
f_N	Nyquist frequency
f_s	Sampling rate of ADC in receive channel
$I_n(t)$	In-phase component in the n-th channel
K_m	Accumulative factor in CORDIC rotation
N_a	Number of accumulator required in each channel in block based $\Delta\Sigma$ beamforming
N'_a	Number of accumulator required in each channel in block based $\Delta\Sigma$ beamforming with reduced beamforming frequency
N_b	Number of beams

N_{ch}	Number of active channels in receive beamforming
N_{interp}	Interpolation factor
N_r	Tap number of reconstruction filter
N_s	Number of samples digitized by ADC in the receive channel along a scanline
N_{st}	Number of stages of the CORDIC rotator
$N_{TF}(z)$	Noise transfer function
$Q_n(t)$	Quadrature component in the n-th channel
ROI	Region of interest
R_s	Radial distance along the scanline
$R_{s,max}$	Maximal imaging depth
$S_{TF}(z)$	Signal transfer function
T_{ts}	Minimum controllable pulse duration provided by the pulser in transmit
T_b	Time for acquiring a beam
$x(n)$	Delta-sigma modulator input
x_{nt}	Ultrasound signal in the n-th receive channel
$x'_n(t)$	n-th channel phase compensated signal in analog IF beamforming
$x''_n(t)$	n-th channel signal ready for summation in analog IF beamforming
$X(z)$	z-transform of the modulator input
$\tilde{x}_n(t)$	Baseband ultrasound signal in the n-th receive channel
β	Required angle in CORDIC rotation
$\Delta\Sigma$	Delta-sigma
$\Delta\tau_n$	Relative time delay applied in the n-th Rx-channel
λ	wavelength corresponding to the center frequency
ω_0	Angular frequency corresponding to the transducer center frequency

ω_r	Local oscillator angular frequency in heterodyning PRB
$\phi_n(t)$	Echo instantaneous phase angle in the n-th channel
$\phi'_n(t)$	Residual delay in heterodyning PRB
$\Phi_{resb,n}(t)$	Phase angle corresponding to the residual delay in BBPRB
$\Phi_{totalb,n}(t)$	Phase angle corresponding to the total delay in BBPRB
θ_i	scanning angle along the i-th scanline in phased array imaging
$\tau_{n,abs}$	Absolute time delay applied in the central Rx-channel
$\tau_{n,abs}$	Absolute time delay applied in the n-th Rx-channel
ζ	ratio of number of tap of the FIR filter using in interpolation beamformer to interpolation factor

List of abbreviations

ADC	Analog-to-digital converter
ADUM	Asynchronous delay update method
BBPRB	Baseband phase rotation beamformer
CFI	Color flow imaging
CIC	Cascaded integrator comb
CNR	Contrast-to-noise-ratio
CORDIC	Coordinate rotation digital computer
DAC	Digital-to-analog converter
DAS	Delay-and-sum
DOF	Depth of field
DR	Dynamic range
DSP	Digital signal processor
FFT	Fast Fourier transform
FIR	Finite impulse response
FIFO	First-in-first-out
FOV	Field of view
FPGA	Field programmable gate array
HDRM	Half delay resolution method
HUS	Home ultrasound system
IF	Intermediate frequency
LE	Logic elements
LPF	Low pass filter
LPM	Library of parameterized modules

LUT	Look-up-table
MRI	Magnetic resonance imaging
MUX	Multiplexer
NRZ DAC	Non-return-to-zero DAC
OSR	Oversampling ratio
PRB	Phase rotation beamformer
RF	Radio frequency
Rx-channel	Receive channel
RZ DAC	Return-to-zero DAC
SCG	Sampling clock generator
SQNR	Signal to quantization noise ratio
VLSI	Very large scale integration

Contents

Summary	i
List of Figures	iii
List of Tables	ix
1 Introduction	1
1.1 Motivation	1
1.2 Contributions	3
1.3 Thesis outline	5
2 Ultrasonic imaging principle	6
2.1 Imaging modes	6
2.2 Array transducer	8
2.3 Ultrasonic beamformation	10
2.3.1 Near-field beamformation	11
2.3.2 Digital beamforming techniques	14
2.4 Image quality characterization	19
3 Digital phase rotation beamforming	22
3.1 Digital baseband phase rotation beamformer	22

3.1.1	Principle and architecture	23
3.1.2	Baseband phase rotation using CORDIC	27
3.2	Digital heterodyning phase rotation beamformer	34
3.2.1	Prior art	34
3.2.2	Fully digital embodiment	37
3.2.3	Image quality evaluation	40
3.2.4	Computational requirement	46
3.3	Conclusion	50
4	Oversampled $\Delta\Sigma$ beamforming	53
4.1	Overview	53
4.1.1	$\Delta\Sigma$ modulation	54
4.1.2	Beamformer architecture	57
4.1.3	Dynamic focusing artifacts	59
4.2	Compensated $\Delta\Sigma$ modulator with zero feedback	63
4.2.1	Inverse insertion and zero feedback	64
4.2.2	Image quality evaluation	66
4.2.3	Return-to-zero DAC implementation	67
4.3	Beamforming with asynchronous delay update	70
4.3.1	The asynchronous delay update method	71
4.3.2	Image quality evaluation	72
4.3.3	An implementation issue	73
4.4	Modified zone-based dynamic focusing	77
4.4.1	Boundary artifacts	78
4.4.2	The solution	81
4.4.3	Image quality evaluation	82

4.4.4	Implementation structure	82
4.5	Hardware resources	86
4.6	Conclusion	97
5	Digital beamforming based on the bandpass sampling principle	101
5.1	Bandpass sampling principle	101
5.2	Application in ultrasonic beamformation	104
5.2.1	The modified approach	106
5.2.2	Embodiment in a $\Delta\Sigma$ beamformer	108
5.3	Conclusion	110
6	Conclusion and suggested future work	113
6.1	The preferred front-end solution	113
6.2	Future work	115
6.2.1	Low voltage coded excitation system for compact front-end design	115
6.2.2	Efficient transmit apodization	117
	Bibliography	121
A	Derivation of equation 2.3	127
B	Derivation of equation 3.23	129

Summary

Ultrasonic imaging has been widely used as a non-invasive diagnostic tool to acquire structural and functional information of the human body being examined. In order to obtain a favorable image quality, modern ultrasound machines usually employ a receive beamformer to produce an enhanced signal by coherently combining the tissue reflected echoes. The associated beamforming performance executes a direct impact on the amount and quality of the extractable information for diagnostic purpose.

In this thesis, several efficient digital beamforming techniques are explored for potential development of a cost effective front-end of a home based ultrasonic imaging system. Dedicated efforts have been made to reduce the system computational complexity and hardware resources with respect to three aspects.

Firstly, phase rotation beamforming techniques are investigated to develop an economic front-end system based on multi-bit Nyquist ADCs. To avoid separate processing of the in-phase and quadrature components, a digital heterodyning phase rotation beamformer is proposed to fulfill the required phase compensation in a partial demodulation stage. The resulting scheme realizes the phase compensation by performing only one multiplication. Further cost reduction in practice is achievable by incorporating the channel apodization into the same multiplication by using merely one digital multiplier in each receive channel.

Secondly, three approaches are proposed to minimize/eliminate the signal distortion due to the dynamic receive focusing in an oversampled post-reconstruction delta-sigma ($\Delta\Sigma$) beamformer. In the first approach, a compensated $\Delta\Sigma$ modula-

tor with zero feedback is developed to take into account the inserted sample which has the opposite sign of its previous sample, thus ensuring the reconstruction filter to produce a faithful interpretation of the modulator output. The second approach, namely the asynchronous delay update method, enables proper stretching of the sample stream without compromise of the delay resolution. It allows consecutive insertion of ± 1 in the same Rx-channel by updating the channel relative delay at appropriate instances. The modified zone-base dynamic focusing technique substantially reduces the memory requirement for delay information storage by updating the relative delay on occasion when the imaging point enters into a new focal zone. It also avoids utilization of unfaithful filter outputs for final image formation by accounting for the group delay of the reconstruction filter. All these approaches qualify a $\Delta\Sigma$ beamformer to produce premium image quality based on the single-bit signal alignment.

Finally, digital beamforming techniques based on the bandpass sampling principle are explored to reduce the data processing rate. It is revealed that by applying the bandpass sampling principle, a pre-reconstruction $\Delta\Sigma$ beamformer with block-based delay can achieve 50 % hardware cost savings of the accumulator in each receive-channel.

List of Figures

1.1	Block diagram of a typical diagnostic ultrasound system	2
2.1	1-D linear array	9
2.2	Different scanning methods of 1-D linear array	10
2.3	Far-field and near-field beamforming schemes	11
2.4	Delay computation for receiving beamforming	12
2.5	Time delay update in dynamic receive focusing	13
2.6	Schematics of interpolation beamforming	15
2.7	Schematics of digital beamforming based on quadrature sampling .	16
2.8	Schematics of non-uniform sampling digital beamforming	17
2.9	Schematics of phase rotation beamforming	18
3.1	Diagram of a pre-filtering baseband PRB	25
3.2	Diagram of a post-filtering baseband PRB	27
3.3	Gray scale images with 70 dB dynamic range produced by (a) the interpolation beamformer, (b) post-filtering baseband PRB (BBPRB) with accurate angle rotation and (c) post-filtering BBPRB with approximated angle rotations by using 4-stage CORDIC rotators . . .	30

3.4	Lateral and axial profiles of the 2nd wire target (from the top) in the post-filtering baseband PRB with (a) (b) accurate angle rotation and approximated angle rotations by using CORDIC rotators with 2 to 5 stages (c)-(j)	33
3.5	Diagram of single stage CORDIC rotator	33
3.6	Schematics of analog IF beamforming	34
3.7	Schematics of hybrid IF beamforming	36
3.8	Block diagram of a digital heterodyning PRB	37
3.9	Replicative spectrum in a common low pass signal sampling scheme (a), a digital heterodyning PRB (b), and a digital heterodyning PRB with an increased sampling rate (c) with dark lines representing the spectrum of the original analog signal and gray lines representing the replicative spectra due to discrete time sampling .	39
3.10	Gray scale images of point targets by (a) interpolation beamformer (b) pre-filtering BBPRB (c) post-filtering BBPRB and (d) heterodyning PRB	41
3.11	Simulation results of axial and lateral profiles of the point target at 30 mm with 60 % -6 dB transducer fractional bandwidth	42
3.12	Simulation results of axial and lateral profiles of the point target at 30 mm with 45% -6 dB transducer fractional bandwidth	42
3.13	Simulation results of axial and lateral profiles of the point target at 30 mm with 30 % -6 dB transducer fractional bandwidth	42
3.14	Gray scale images of a cyst by (a) interpolation beamformer (b) pre-filtering PRB (c) post-filtering PRB and (d) heterodyning PRB	44
3.15	Gray scale image with 70 dB dynamic range produced by the heterodyning PRB	45

3.16	Axial (a) and lateral (b) profile of the third wire target (from the top)	46
3.17	Phantom study results by the heterodyning PRB (left column), post-filtering BBPRB (mid-column), and interpolation beamformer (right column) in (a) and (b), zoomed axial plot along the scanline passing through the fifth wire target (from the top) (c) and zoomed lateral profile of the same target (d)	48
4.1	Diagram and linear model of a second-order $\Delta\Sigma$ modulator	56
4.2	Noise shaping effect in $\Delta\Sigma$ modulation	57
4.3	Diagram of a post-reconstruction $\Delta\Sigma$ beamformer	58
4.4	Diagram of a pre-reconstruction $\Delta\Sigma$ beamformer	59
4.5	Sample selection in a digital beamformer with real time dynamic focusing	60
4.6	Field II simulation results produced by a $\Delta\Sigma$ beamformer employing dynamic focusing with pre-reconstruction (a) and post-reconstruction strategy (b), and employing static receive focusing with post-reconstruction strategy (c)	62
4.7	Stretch the sample stream by repeating the previous sample (a), and inserting an effective zero sample (b)	63
4.8	Field II simulation results produced by a $\Delta\Sigma$ beamformer with the insert-zero technique	63
4.9	Schematics of the compensated $\Delta\Sigma$ modulator with 2-X buffer . . .	64
4.10	Stretch the sample stream by repeating and inserting the inverse of the previous sample	65
4.11	Schematics of the compensated $\Delta\Sigma$ modulator with zero feedback .	66

4.12 Field II simulation results by $\Delta\Sigma$ beamforming with the 2-X buffer $\Delta\Sigma$ modulator	67
4.13 Field II simulation results by $\Delta\Sigma$ beamforming with the zero feed- back $\Delta\Sigma$ modulator	67
4.14 Emulation results by $\Delta\Sigma$ beamforming using 2-X buffer modulator with repeated samples (left), zero-feedback modulator with inverted samples (mid) and uncompensated modulator with repeated sam- ples (right)	68
4.15 Generated pulses by NRZ, RZ and controlled RZ DACs	69
4.16 Schematic implementation of the zero feedback by a RZ DAC	70
4.17 Stretch the sample stream in the ADUM and the repeat technique .	72
4.18 Sample selection in the ADUM and the repeat technique	73
4.19 Field II simulation results by $\Delta\Sigma$ beamforming with various insert ± 1 techniques	74
4.20 Phantom study results by applying various insert ± 1 techniques . .	76
4.21 Delay update in zone-based dynamic focusing	78
4.22 Sample selection in a particular Rx-channel in zone-based dynamic focusing with a zone depth of 5 mm	79
4.23 Direct sharing of reconstruction filter in the conventional zone-based dynamic focusing	80
4.24 Appending samples in modified zone-based dynamic focusing	81
4.25 Emulation results by the conventional (left column) and modified (right column) zone-based dynamic focusing	83
4.26 Field II simulation results by applying zoned-based dynamic focus- ing with a zone depth of 5 mm	85

4.27	Diagram of the $\Delta\Sigma$ beamformer employing the modified zone-based dynamic focusing technique	86
4.28	Implementation of a pre-reconstruction $\Delta\Sigma$ beamformer	88
4.29	Implementation of $\Delta\Sigma$ beamformer with symmetrical holding	90
4.30	Implementation of a CIC filter	90
4.31	Implementation of a $\Delta\Sigma$ beamformer with block based selection . .	91
4.32	Implementation of a $\Delta\Sigma$ beamformer with modified zone-based dynamic focusing	92
5.1	Spectra of discrete-time signals with dark lines representing the spectrum of the original analog signal and the gray lines representing the spectral replications due to discrete time sampling	103
5.2	Phantom study results produced by the modified quadrature sampling technique	106
5.3	Schematics of a $\Delta\Sigma$ beamformer with block-based delay	109
5.4	Phantom study results produced by a pre-reconstruction $\Delta\Sigma$ beamformer with a reduced beamforming frequency. Interpolation, Pre-recon DS with LP and Pre-recon DS with BP represent respectively the interpolation beamforming, block-based DS beamforming proposed by Han <i>et al.</i> and the Han's method at a reduced beamforming frequency with bandpass sampling principle being applied . . .	111
6.1	Diagram of a $\Delta\Sigma$ based coded excitation system with pre-compression & post-reconstruction	117
6.2	Diagram of a $\Delta\Sigma$ based coded excitation system with post-compression & post-reconstruction	117
6.3	Apodization by amplitude weighting	118

6.4	Apodization by changing the pulse width	118
6.5	Generation of (c) the encoded excitation signal by convolving (a) the coding kernel and (b) the base sequence	120
6.6	Generation of (c) the encoded excitation signal by changing the duration of (b) base sequence while keeping (a) the coding kernel unaltered	120
A.1	Delay computation for receive beamforming	127
B.1	Spectrum of the partial demodulated signal in heterodyning PRB with dark lines representing the spectrum of the original analog signal and gray lines representing the replicative spectra due to discrete time sampling	129

List of Tables

3.1	CORDIC angles	28
3.2	Preliminary hardware evaluation results	31
3.3	CNR value from the simulated cyst phantom	43
3.4	Required number of multiplications and additions	49
3.5	Computational requirement in percentage with reference to other beamforming techniques	50
4.1	New coding theme in the insert-zero technique	61
4.2	Parameters used in the estimation of hardware resources	87
4.3	Estimated hardware resources for pre-reconstruction $\Delta\Sigma$ beamformer	89
4.4	Estimated hardware resources for $\Delta\Sigma$ beamformer with symmetrical holding	93
4.5	Estimated hardware resources for $\Delta\Sigma$ beamformer with block based selection	94
4.6	Estimated hardware resources for $\Delta\Sigma$ beamformer with modified zone-based dynamic focusing	95
4.7	Summary of hardware resources	96
4.8	Memory requirement in change of number of focal zone	96

4.9	Summary of various $\Delta\Sigma$ beamforming techniques with dynamic re-	
	ceive focusing	99

Chapter 1

Introduction

1.1 Motivation

Since the introduction of medical ultrasound in 1950s, diagnostic ultrasound has progressed from simple A-mode imaging to nowadays more complicated B-mode, Doppler and 3-D imaging applications. Meanwhile, the image quality has undergone a significant improvement over the last two decades benefited from the advance in modern VLSI technology. Diagnostic ultrasound imaging today has become a popular imaging modality, providing real time diagnostic information in a non-invasive way.

At present, there is a growing awareness that decentralization of medical care will be a central theme in development of biomedical technology in the new century. The trend in miniaturization and cost reduction of biomedical instruments is also an outgrowth of the challenges in distributed home healthcare. Modern ultrasound machine takes the advantage of relatively low cost and higher portability in comparison to other imaging modalities, such as computed tomography and magnetic resonance imaging (MRI). Ultrasound imaging thereby presents the highest potential for home-based imaging among various diagnostic imaging modalities [1].

1.1. Motivation

Figure 1.1 illustrates the block diagram of a typical diagnostic ultrasound system. The front-end receive beamformer, as highlighted, has a direct impact on the resulting image quality. Due primarily to the huge data volume prior to front-end beamformation, state-of-the-art ultrasound machines usually employ high speed, complicated circuits to perform computationally demanding signal processing tasks in real time. Thus, further miniaturization and cost reduction of front-end system can be an unending process promoted by advances in modern circuit design technology as well as signal processing techniques.

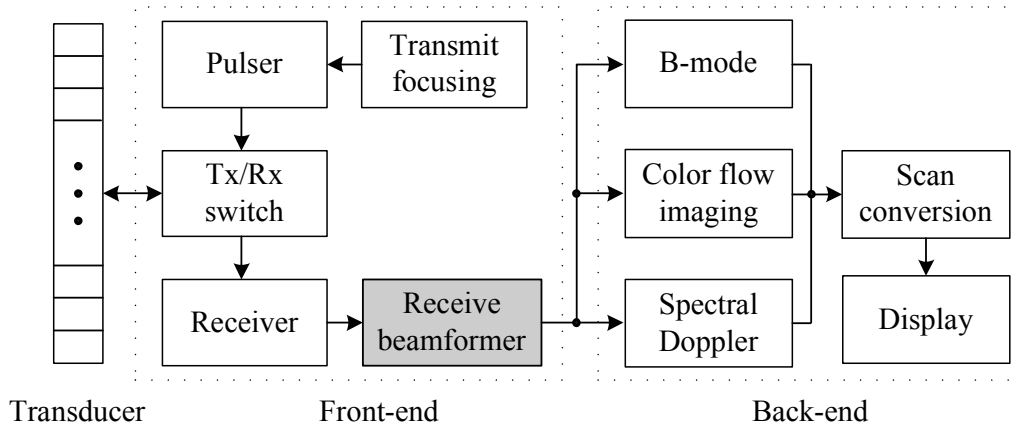


Figure 1.1: Block diagram of a typical diagnostic ultrasound system

A collaborative project between the University of Washington and Nanyang Technological University is being carried out to develop a low-cost and easy-to-use home ultrasound system (HUS). The prospective HUS would be initially used by current users (e.g., sonographers), followed by primary care clinicians in performing routine examinations or annual checkups (e.g., breast cancer screening, coronary artery disease detection and assessing stroke risk) including visiting nurses. Afterwards, with further cost reduction, improved ease of use and demonstrated efficacy, it could move down to the users at home.

The goal of this work is to investigate a cost effective front-end solution, more

1.2. Contributions

specifically, a low-cost digital receive beamformer. The desirable front-end solution would produce images, yielding adequate diagnostic information with reduced hardware cost and/or computational requirement. As a result, the proposed structure and configuration of the front-end beamformer could be potentially employed in the development of the proposed HUS.

1.2 Contributions

This thesis makes several significant contributions towards future research and development of low cost digital beamformers as a cost effective front-end solution in HUS, including:

- Propose a fully digital heterodyning phase rotation beamformer with simplified data path logic consisting of merely one digital multiplier and necessary digital buffers per receive-channel (Rx-channel).
- Propose a compensated delta-sigma ($\Delta\Sigma$) modulator with zero-feedback that restores the image quality in a post-reconstruction $\Delta\Sigma$ beamformer with dynamic delays.
- Propose the asynchronous delay update method to eliminate the dynamic focusing artifacts in a post-reconstruction $\Delta\Sigma$ beamformer.
- Propose the modified zone-based dynamic focusing technique to substantially reduce the memory requirement for delay information storage in a $\Delta\Sigma$ beamformer.

1.2. Contributions

- Applying the bandpass sampling principle to the $\Delta\Sigma$ beamformer with block-based delay to achieve around 50 % cost savings on the accumulator in each Rx-channel.

Findings reported in this thesis have been published or are being prepared for publication in the following papers:

- C. Gao, L. Zhang and E. M. C. Wong, “Design of a digital phase shift beamformer for ultrasonic imaging,” in Proceeding of IEEE International Workshop on Biomedical Circuits & Systems, December 2004, pp. S2.2, 13-16.
- C. Gao, J. Zhou, L. M. Koh and E. M. C. Wong, “Oversampled delta-sigma beamformer with modified zone-based dynamic focusing,” in Proceeding of IEEE International Symposium on Biomedical Imaging, April 2006, pp. 892-895.
- C. Gao, L. M. Koh and E. M. C. Wong, “Equalized delta-sigma ultrasound beamforming” submitted to *Ultrasonics*.
- C. Gao and E. M. C. Wong, “Oversampled delta-sigma beamformer with asynchronous delay update” to be submitted to *Ultrasonics*.
- C. Gao, L. M. Koh and E. M. C. Wong, “A digital heterodyning phase rotation beamformer for very low cost ultrasound imaging” to be submitted to *Ultrasonics*.

1.3 Thesis outline

Chapter 1 presents the motivation of this work followed by a list of the achieved significance and contributions.

Chapter 2 briefly reviews the principle and functionality of medical ultrasonic imaging. More details are provided to describe the evolution of digital beamforming techniques in the past two decades.

Chapter 3 demonstrates the efficient implementation of a baseband phase rotation beamformer with simplified phase rotator using CORDIC. A digital heterodyning phase rotation beamformer is proposed to achieve an economic data path logic comprising a digital multiplier and necessary digital buffers per Rx-channel.

Chapter 4 investigates the potential to use an oversampled $\Delta\Sigma$ beamformer in the envisioned HUS. Three efficient approaches are proposed to restore the image quality in a cost effective post-reconstruction $\Delta\Sigma$ beamformer with dynamic delays.

Chapter 5 is specifically related to applying the bandpass sampling principle in medical ultrasound beamforming. Its theoretical basis as well as practical embodiments are presented.

Chapter 6 discusses the preferred front-end solution for envisioned HUS as a conclusive summary of this work. It concludes with the suggested future research work for HUS.

Chapter 2

Ultrasonic imaging principle

This chapter reviews the principle of medical ultrasonic imaging. The evolution of various efficient digital beamforming techniques is delivered as literature review in more detail.

2.1 Imaging modes

In medical ultrasound imaging, a transducer sends ultrasonic waves into the human body under examination. At the interface between two types of tissue, part of the wave will be reflected back and detected by a receive transducer. The rest of the wave continues deeper into the body, and will be reflected from the surface of tissues lying further inside the body. The echoes' physical characteristics, such as intensity, traveling time as well as frequency shift, contain the structural and functional information of the object being examined. A diagnostic ultrasound machine has been used to extract this information by performing required signal processing and display it in a number of ways.

Nowadays, brightness mode or B-mode is the most commonly used imaging

2.1. Imaging modes

mode, in which the intensity of the echo signal is mapped into the brightness of the pixel for display. In a prevalent pulse-echo system, pulse waves are typically transmitted along a particular direction to form a beam (or termed scanline). Amplitudes of the associated echoes are then coded in the gray scale, with stronger echoes being represented in higher brightness, to yield an A-line pattern. This operation is repeated by transmission of the waves along quite a few different directions sequentially. After the beams sweep over a planar imaging field, the acquired scanlines are used to produce a two-dimensional (2-D) echo intensity image, displaying a cross-sectional view of the imaging object [2].

Another popular imaging mode utilizes the wave Doppler effect for measurement of the blood flow velocity. In this Doppler application, multiple firing of ultrasonic wave in a particular direction is usually required to obtain the frequency shift caused by object motion. Based on the narrow band auto-correlation technique [3], modern ultrasound systems employing color flow imaging (CFI) are able to produce a 2-D color-coded map of Doppler shifts in real time. The mapping of flow velocity is then superimposed onto a B-mode gray scale image to highlight the location and direction of moving scatterers, referred to as duplex scanning. Besides, spectral Doppler processing based on the fast Fourier transform (FFT) is used to obtain an exquisite flow measurement in a small sample volume. Since echoes generated by the moving scatterers, *i.e.* red blood cells, are typically around 40 dB below those of the neighboring static tissue [4], a higher system dynamic range (DR), as compared to the B-mode, is usually required in the Doppler application.

There are other advanced imaging modes (applications) such as strain imaging, B-flow and three-dimensional (3-D) imaging supported by the state-of-the-art high-end machines. Fortunately, the beamforming principle is essentially the same for

2.2. Array transducer

all these applications, which in practice may ease the design and development of a digital beamformer applicable in various operation modes.

2.2 Array transducer

Transducers utilizing piezoelectricity have been widely used in commercial diagnostic ultrasound systems. With dual function, the piezoelectric crystal changes its physical dimension when exposed to an electric field, and on the other hand it creates an electric field (voltage signal) across itself when deformed by external pressure. Namely, the piezoelectric transducer converts ultrasonic waves into electrical waves and vice versa as follows:

$$\text{electrical pulse} \Leftrightarrow \text{mechanical oscillation} \Leftrightarrow \text{ultrasonic wave}$$

In principle, the transducer can be either a continuous aperture or a discrete array, which consists of multiple transducer elements. Array transducers are prevailing today due to their ease in beam steering and focusing through electronic beamforming. Figure 2.1 depicts a widely used one-dimensional (1-D) linear array transducer, which comprises multiple elements distributed in one row. As there is merely one single element in elevation, electronic steering and focusing can be only performed in the azimuth (lateral) direction. 2-D arrays containing multi-row elements are able to perform focusing in both azimuth and elevation. However, there are fundamental problems in construction and use of 2-D dense arrays due to their excessively large number of elements, *e.g.* accurate dicing of the piezoelectric material, exorbitant front-end resources and demanding processing requirement. Therefore, there exist 4D ultrasound systems employing a 1-D linear array with mechanical rotation in elevation to perform the real-time 3-D imaging.

2.2. Array transducer

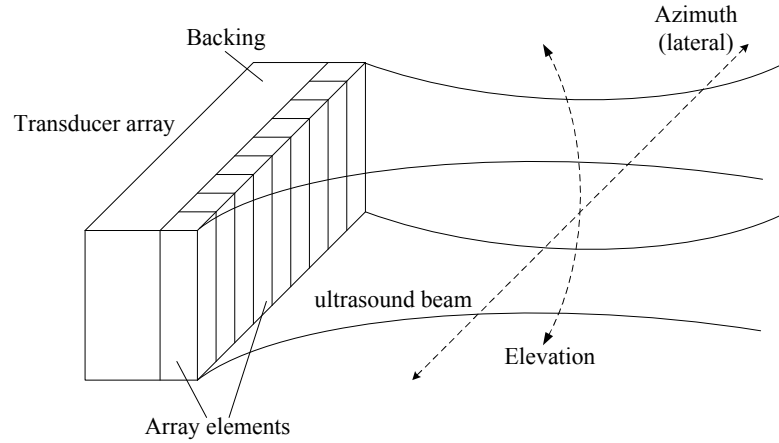


Figure 2.1: 1-D linear array

Figure 2.2 shows the three types of scanning method of a 1-D linear array. In particular, phased arrays consist of relatively small number of elements and usually activate all their elements for transmission as well as reception. Through electronic beamformation, they typically produce sector images by steering the beam across a range of angles. As array elements are essentially uniformly spaced electrical sensors used to sample the incoming wave signal, phased arrays usually have approximately $\lambda/2$ pitch size, with λ being the wavelength, to avoid grating lobes [5]. Because of their small aperture size, phased arrays are often used in applications with restricted acoustic window, *e.g.* the intercostal cardiac imaging. A switched linear array involves running an active sub-aperture across a large number of available transducer elements. Individual beams perpendicular to the array aperture are formed by each sub-aperture to produce a 2-D rectangular image. Since switched arrays perform electric focusing without steering, a wider element spacing is usually permitted, thereby enabling a simpler array construction. In addition, the associated beamforming is of less complexity in that identical delay sets are applied for the respective scanlines. The third type of linear array, *i.e.* convex array, consists of elements mounted on an arc-shaped aperture. Its operation mode is essentially the same with the switched linear array except that a

2.3. Ultrasonic beamformation

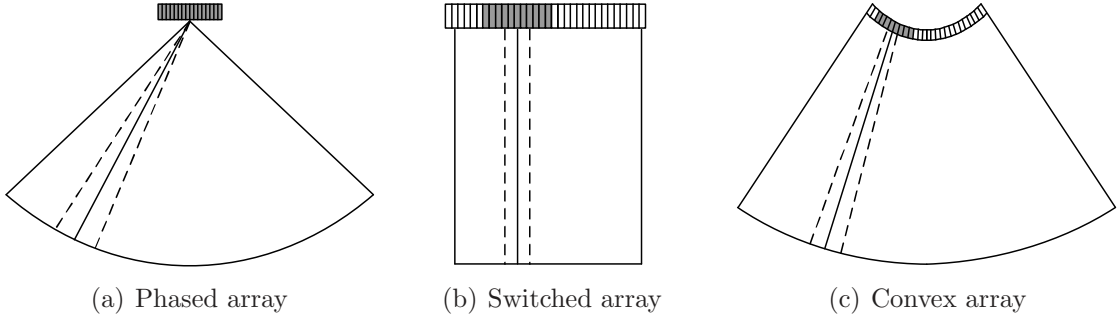


Figure 2.2: Different scanning methods of 1-D linear array

sector image with wider field of view (FOV) can be achieved as depicted in Figure 2.2(c).

In a pulse-echo imaging system, the same transducer array is almost always used for both transmission and reception of the ultrasonic wave. Echoes received by the n -th element in such kind of system can be modeled as a bandpass signal $x_n(t)$ given by [6]:

$$x_n(t) = A_n(t) \cdot \cos(\omega_0 t + \phi_n(t)) , \quad (2.1)$$

in which $A_n(t)$ is the echo envelope, $\phi_n(t)$ is the instantaneous phase angle and $\omega_0 = 2\pi f_0$ is the angular frequency with f_0 being the transducer resonance frequency.

2.3 Ultrasonic beamformation

The echo $x_n(t)$ received by the array element is delayed by an appropriate amount and then combined with signals received by the other elements. This procedure, referred to as receive beamforming, is conducive to a high quality image formation by producing an enhanced echo signal arriving from a particular focal point or direction. The applied time delays ensure that signals arriving from the desired location will sum coherently, whereas signals arriving from other locations

2.3. Ultrasonic beamformation

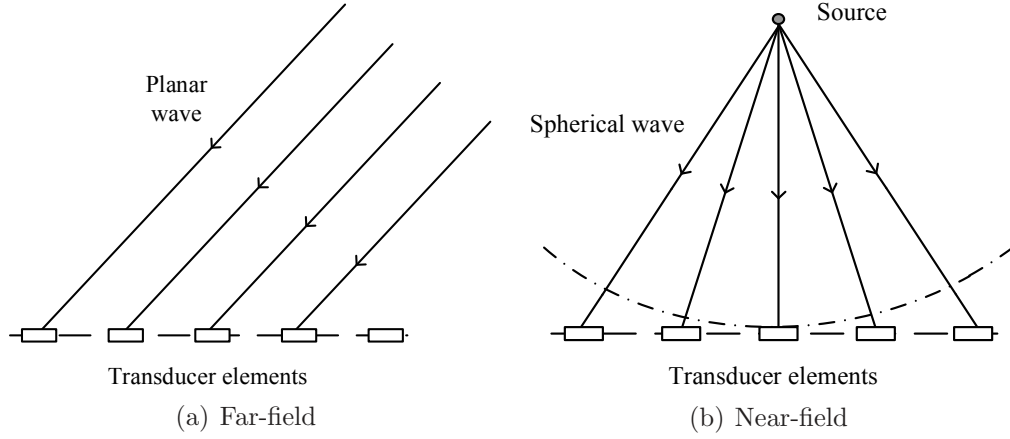


Figure 2.3: Far-field and near-field beamforming schemes

will experience partial or complete cancellation. Hence, the summation output (the formed beam) ideally contains only the indicative information of the examination object along the current scanline. Accordingly, 2-D imaging with minimum interference from neighboring objects can be accomplished in this way.

In this text, beamforming would exclusively refer to receive beamforming unless otherwise explicitly specified, whilst the operation of applying time delay in the transmission stage is denoted as transmit focusing.

2.3.1 Near-field beamformation

A wide variety of applications, *e.g.* radar, sonar and ultrasonic imaging, perform beamforming to obtain an improved system performance. The diagnostic ultrasound beamforming has the distinctive feature of its near-field operation. Figure 2.3 illustrates the far-field and near-field beamforming schemes in which the sensor's received signals are modeled as planar and spherical waves respectively.

Assuming that the time starts when the firing of the last element for transmission is completed, the absolute time applied in the n -th Rx-channel, as illustrated

2.3. Ultrasonic beamformation

in Figure 2.4, is given by:

$$\tau_{n,abs} = (R_s + \sqrt{dz^2 + (R_s \cdot \sin \theta_i - dx_n)^2})/c, \quad (2.2)$$

in which R_s is the radial distance along the i -th scanline, dz is the distance along the z -axis, dx_n is the x -coordinate of the n -th element and c is the wave mean velocity in the human body. Based on the parabolic approximation as well as the large f -number assumption, equation 2.2 can be simplified to [7]:

$$\tau_{n,abs} = (-x_n \cdot \sin \theta_i + \frac{x_n^2 \cos^2 \theta_i}{2R_s} + 2R_s)/c, \quad (2.3)$$

in which the first and second items represent the steering and focusing delay respectively (see Appendix A).

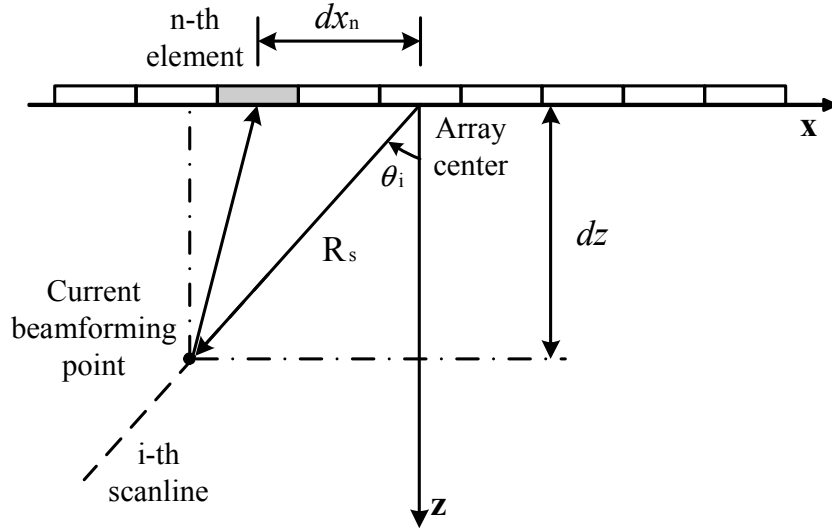


Figure 2.4: Delay computation for receiving beamforming

It is apparent that the ideal time delay is range dependent, *i.e.* a function of time denoted as $\tau_{n,abs} = \tau_{n,abs}(t)$. Therefore, dynamic receive focusing, which enables each beamformed sample in flawless focusing, has been widely used to obtain superior image quality. In an ultrasound machine employing dynamic receive fo-

2.3. Ultrasonic beamformation

cusing, the corresponding delays applied in individual Rx-channels are constantly being updated as the imaging point penetrates into deeper area. Figure 2.5 shows a typical delay profile applied to the scanline perpendicular to the aperture. Using the center element as reference, computation based on equation 2.2 indicates that the relative time delay of the n -th channel, $\Delta\tau_n(t) = \tau_{n,abs}(t) - \tau_{c,abs}(t)$ with $\tau_{c,abs}$ being the absolute time delay applied to the center element, will decrease as the wave exploring into the deeper area (as the time increases). That is easily understandable since the relative delay $\Delta\tau_n$ would ultimately approach zero when the scanline extends to the infinite depth, *i.e.* evolved into far-field beamformation. In spite of an increased system complexity introduced by the time-variant delay update, the receiving dynamic focusing in practice is essential to achieve a premium image quality.

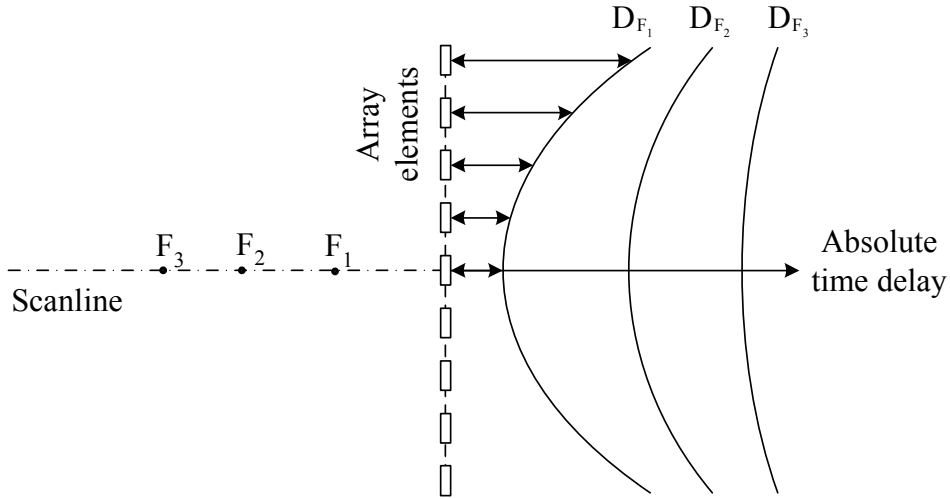


Figure 2.5: Time delay update in dynamic receive focusing

2.3. Ultrasonic beamformation

2.3.2 Digital beamforming techniques

To fulfill the required time delay, beamforming systems employing analog delay lines suffer from the poor channel-to-channel matching problem, thus resulting in a limited dynamic range. With the advent of in modern VLSI technology, particularly in design of analog to digital converters (ADCs) and application specific integrated circuits (ASICs), digital beamforming techniques have been widely used in today's commercial ultrasonic imaging systems, yielding precise and reliable time delay.

For digital implementation of the classic digital delay-and-sum (DAS) beamforming, reflected echoes are typically sampled by an ADC and stored in digital memory in individual Rx-channel. Appropriate echo samples are selected to fulfill the time delay and then coherently combined together to produce the beamformed sequence. In practice, the time delay in equation 2.2 is quantized to units of sampling interval T_s and therefore a sufficiently high sampling rate is required in a digital DAS beamformer so as to yield a favorable delay resolution. It is commonly agreed that a minimum delay resolution of $1/(16 \times f_0)$ is required for high performance digital beamformation [8,9]. However, equipment which uses a high speed ADC in each Rx-channel apparently lacks design efficiency. An interpolation based technique was thereby proposed to ease the demanding sampling speed in a digital DAS beamformer [10]. By performing zero padding and the subsequent low pass filtering, the digital linear interpolation obtains an effective sampling rate of f_{eff} given by:

$$f_{eff} = N_{interp} \times f_s , \quad (2.4)$$

in which f_s is the real sampling rate and N_{interp} is an integer, denoting the interpolation factor. Thus, this approach achieves a high delay resolution $1/f_{eff}$ by

2.3. Ultrasonic beamformation

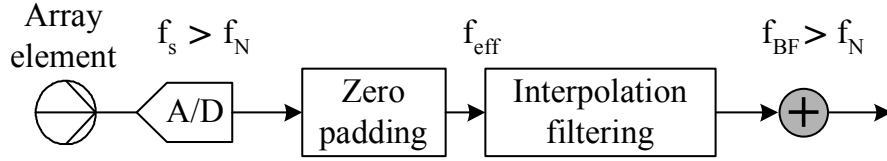


Figure 2.6: Schematics of interpolation beamforming

actually sampling at a low frequency complying with the Nyquist criteria. Notice that the data rate of the beamforming output, defined as the beamforming frequency f_{BF} , needs to be no less than the Nyquist rate f_N [11]. Applying poly-phase decomposition in the interpolation beamformer can greatly reduce the computation load for digital filtering as well as delay calculation. The delay interpolator beamformer disclosed in [12] is a particularly efficient implementation of this concept. Delays in this beamformer are fulfilled in two steps, namely a rough delay and a fine delay. The rough delay is directly applied on the echo samples with a delay resolution of $1/f_s$, whereas a fine delay is realized by a finite impulse response (FIR) filter with fractional delay, *i.e.* group delay less than the sampling interval T_s . The sum of fine delay and rough delay would approximate the ideal time delay as specified in equation 2.2. The underlying principle of the delay interpolator beamformer can be understood as a simplified interpolation beamformer, which avoids multiplications involving the padded zeros and computes only those samples for the final beam output. Additionally, a set of optimized filter coefficients, taking the form of $1 = 2^p$ with p being an integer, was also disclosed. This in practice enables an efficient implementation of the digital filter by simple binary digit shift and summation. However, this approach is limited in its flexibility and encounters difficulty in synthesizing simple filter coefficients to yield a delay less than quarter of the sampling period [13].

In order to further reduce the sampling rate requirement, Powers *et al.* pro-

2.3. Ultrasonic beamformation

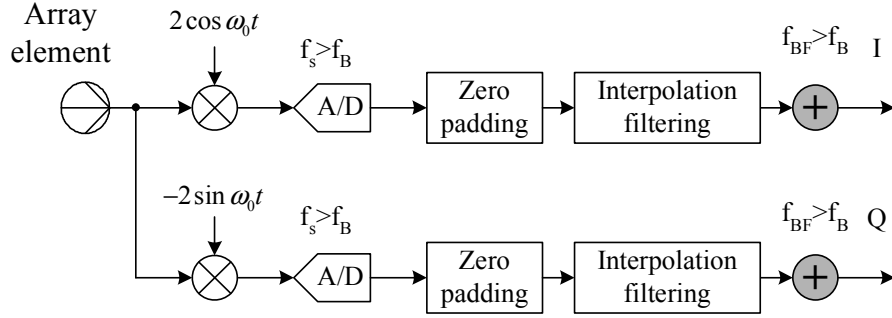


Figure 2.7: Schematics of digital beamforming based on quadrature sampling

posed a digital beamforming technique based on the quadrature sampling approach [14]. Figure 2.7 illustrates the scheme of this quadrature beamforming technique, which is essentially a special case of the shifted side band beamformer proposed in [15]. In particular, received echoes are demodulated to baseband prior to digitization by an analog oscillator in each Rx-channel. A sampling rate compatible with the signal bandwidth f_B , rather than the signal's highest frequency component $f_0 + f_B/2$, is permitted to sample the baseband in-phase (I) and quadrature (Q) components. In addition, the delay resolution is generally less demanding in quadrature beamforming since quantized delays are applied to the baseband I/Q signals, which are less rapidly varying functions of time. Based on a relatively narrow band assumption, Powers *et al.* also suggested a second-order sampling approach to eliminate the analog oscillator and low pass filter in individual Rx-channel. More specifically, I/Q signals are obtained by directly sampling the bandpass echoes with a time difference of one quarter of the carrier period, *i.e.* $1/(4 \cdot f_0)$. Coherent summation of I/Q signals are separately obtained and then the envelope signal can be computed. Later researchers proposed multi-order sampling approach to account for the wide band nature of echoes in diagnostic imaging applications [16]. Unfortunately, to achieve a prescribed delay resolution, the complicated digital interpolation is still unavoidable.

2.3. Ultrasonic beamformation

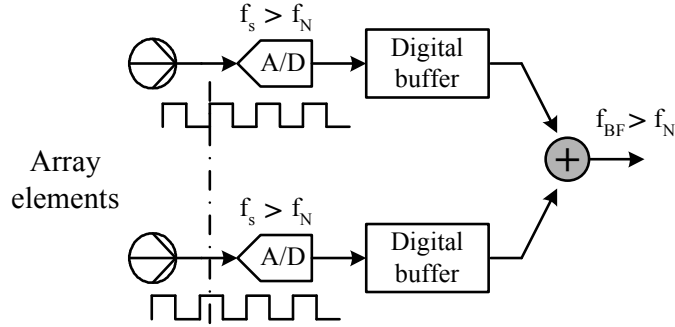


Figure 2.8: Schematics of non-uniform sampling digital beamforming

In fact, the aforementioned implementation of the DAS beamforming trades the digital signal processing task, *i.e.* digital interpolation, with the ADC sampling rate. A wiser implementation applies beamforming relative delays to the sampling clocks driving the ADCs rather than manipulates the channel digital sample streams [17]. A sampling clock generator (SCG), containing a high frequency master clock and look-up-table (LUT) storing the delay information, was used to control the respective channel sampling instances, thus providing necessary delay accuracy as shown in Figure 2.8. This non-uniform sampling technique can be relatively simple since the digital filtering can be obviated. Nonetheless, a very careful layout of the VLSI circuit is necessary as the clock skew might introduce undesirable delay errors.

Unlike time domain DAS beamforming, another general kind of beamforming technique utilizes signal phase adjustment to fulfill the channel coherent summation. Figure 2.9 illustrates the schematics of the earliest fully digital phase rotation beamformer proposed by O'Donnell *et al.* [18]. The echoes are sampled directly by an ADC working above the Nyquist rate followed by digital mixing and low pass filtering. The baseband sequences, namely I/Q signals, can be accurately delayed, rotated and summed at a reduced operation frequency, which only needs to be above the signal bandwidth f_B . The total time delay are fulfilled in two steps

2.3. Ultrasonic beamformation

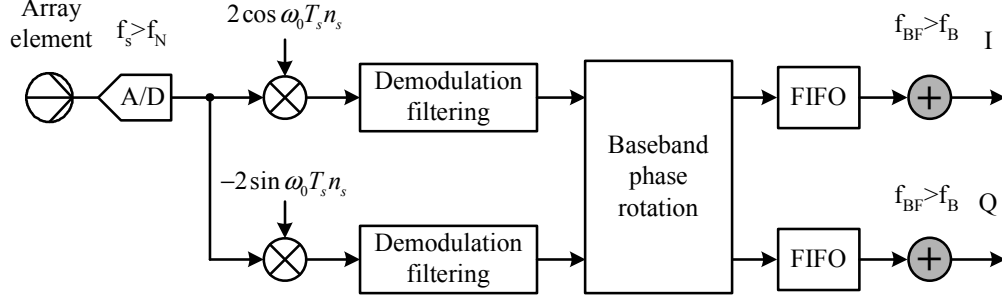


Figure 2.9: Schematics of phase rotation beamforming

similar with the delay interpolator beamformer in [12] except that the fine delay is realized by baseband phase rotation. Subsequently, a phase-error-free quadrature sampling technique was proposed by Chang *et al.* to eliminate the unwanted phase error in this design [19]. Ranganathan *et al.* proposed a simplified implementation, termed direct sampled I/Q beamforming, by employing the second-order sampling technique to remove the digital mixer and low pass filter in each Rx-channel [6]. As compared to the interpolation beamformer running at the Nyquist rate, the phase rotation beamformer is more appealing for the design of a cost effective system by allowing a relatively lower beamforming frequency. The detailed configuration and implementation of the phase rotation beamformer as well as its efficient variants will be discussed later in Chapter 3.

All three beamforming techniques presented above, including interpolation, non-uniform sampling and baseband phase rotation, have been used in various forms in commercial systems. Benefited from the high precision and low noise merits of digital electronics, beamformation with favorable performance can be achieved. Subsequently, a variety of signal processing operations, such as envelope detection, auto-correlation and FFT, are applied to the beamformed sample stream in order to generate high quality gray scale, color flow as well as spectral Doppler images.

2.4. Image quality characterization

In general, the time domain DAS beamforming techniques are more robust to broadband processing since all the containing frequency components could be accurately delayed. However, phase rotation beamforming might be more economic by allowing a lower beamforming frequency. Recently, a novel DAS beamforming technique based on the $\Delta\Sigma$ modulation has been proposed to dramatically reduce the size and complexity of front-end electronics, which will be discussed in detail in Chapter 4.

2.4 Image quality characterization

Precise diagnosis relies heavily on the obtained image quality, which can be characterized in terms of spatial resolution, contrast resolution, depth of field and frame rate. Meanwhile, these parameters also provide the criteria on which the beamforming performance can be evaluated.

Spatial resolution

Spatial resolution is defined as the minimum distance between two points that can be distinguished as separate objects. It must be considered in two aspects, *i.e.* axial and lateral resolution. Axial resolution is the minimum separation between two interfaces located in a direction parallel to the beam so that they can be imaged as two different interfaces. In a pulse-echo imaging system, it is determined by the pulse length, which is the product of the wavelength and the number of cycles in the pulse. Existing systems usually emit broadband short pulses, consisting of one to two cycles, to obtain a favorable axial resolution. Similarly, lateral resolution describes the minimum separation of two interfaces aligned along the direction

2.4. Image quality characterization

perpendicular to the ultrasound beam. For 1-D linear arrays, a larger aperture size, usually comprised of more transducer elements, can provide better lateral resolution.

Contrast resolution

The contrast resolution describes the ability to detect small variations in the intensity of the backscattered signal from targets that are close to each other. It can be defined as the ratio between the amplitude of the echo signal around the cyst to the signal from reverberations inside the cyst. The main limitation of the contrast resolution is the noise caused by the sidelobes (due to imperfect beamforming) and multiple reflections of the ultrasonic waves. A high delay resolution for accurate beamforming is indispensable to obtain a favorable contrast resolution. In addition, electronic component noise in the receiver will also limit the contrast resolution [20].

Depth of field (DOF)

The DOF of an ultrasound imaging system is generally defined as the axial region over which the system response is uniform within some predetermined limit [21]. Transmit apodization, dynamic receive aperture and dynamic receive focusing have been widely used in commercial systems to cope with the beam diffraction and scattering effects. On the other hand, as ultrasonic waves undergo significant attenuation as the pulse travels through the human tissues, the coded excitation technique has been proposed to greatly enhance the penetration depth with minimum compromise of the spatial resolution by transmitting temporally encoded pulses (*e.g.* Golay and chirp) and performing corresponding pulse compression in

2.4. Image quality characterization

receive [22].

Frame rate

The frame rate F_r is defined as the number of formed images per second. In a 2-D imaging system, the time to generate an image is equal to the time per beam T_b multiplied by the number of beams N_b . The system has to wait at least for $2 \times R_{s,\max}/c$ to collect the echo from the maximum imaging depth $R_{s,\max}$ before transmission of the pulse for the next beam. To make sure that the signal from the preceding pulse is sufficiently attenuated, an extra period of time T_e has to be taken into account. The frame rate thus is given by [20]:

$$F_r = \frac{1}{N_b \cdot T_b} = \frac{1}{N_b \cdot (2R_{s,\max}/c + T_e)} , \quad (2.5)$$

which is a parameter of much concern in the real time cardiac imaging.

In fact, factors affecting image quality are not independently determined by some specific beam parameters. For instance, to obtain an exquisite axial resolution, higher frequency waves are desirable whereas they suffer more significant attenuation when travelling through the human tissues, thus causing a decrease in DOF. Trade-off also exists between the contrast and lateral resolution, *i.e.* sufficient sidelobes depression can yield a high contrast resolution while this usually incurs lateral resolution loss due to an increased mainlobe width. Trading the image quality parameters thus relies much on the application specific requirements and the configuration of the conceived beamformer system should also be adjusted accordingly.

Chapter 3

Digital phase rotation beamforming

This chapter presents the principle and configuration of the phase rotation beamformer as well as a variety of its embodiments. A fully digital heterodyning phase rotation beamformer is developed to simplify the beamformer data path to a simple digital multiplier with necessary digital buffers in each Rx-channel.

3.1 Digital baseband phase rotation beamformer

It is recognized that delaying an arbitrary signal in the time domain is equivalent to performing a corresponding phase shift (rotation) in the frequency domain. In this chapter, phase rotation beamforming refers to any beamforming technique, which employs the echo phase rotation (compensation) to fulfill the coherent summation in receive beamforming. This section is specifically related to the principle and efficient implementation of the baseband phase rotation beamforming technique. Another efficient approach, *i.e.* the intermediate frequency (IF) phase rotation beamforming or termed heterodyning phase rotation beamforming, will

3.1. Digital baseband phase rotation beamformer

be presented later in Section 3.2.

3.1.1 Principle and architecture

The digital baseband phase rotation beamformer (PRB) was initially disclosed by O'Donnell *et al.* in early 1990s [8, 18]. In order to circumvent the demanding sampling rate in a DAS beamformer, the developed beamformer employs baseband phase rotation to fulfill the accurate time delay. As described in Chapter 2, the prescribed time delay is accomplished in two steps: fulfillment of the rough delay through sample selection and fine delay through baseband phase rotation. The rough delay is applied with a low delay resolution $1/f_s$, in which the sampling rate f_s is slightly above the Nyquist rate. The sum of rough and fine delay is equal to the prescribed time delay for a particular Rx-channel. The preferred embodiment, as redrawn in Figure 3.1, indicates that the fine delay is applied first followed by the rough delay. In addition, each Rx-channel is equipped with two finite impulse response (FIR) filters to remove the sum frequency components produced by the digital mixing, referred to as pre-filtering baseband PRB. Consequently, the disclosed beamformer enables a reduced beamforming frequency without spectral aliasing by mixing the bandpass echo signal down to baseband. The minimum beamforming frequency, given by $f_{BF_{min}} = f_B$, only needs to comply with the Nyquist criteria for the down-mixed baseband signals. Assuming that the echo in the n -th channel, with reference to the signal $x_c(t)$ received by the central element, undergoes a time lag of $\Delta\tau_n(t)$, which is a function of imaging depth (or time) for

3.1. Digital baseband phase rotation beamformer

the near field beamforming, the received echoes can be characterized as:

$$x_c(t) = A_c(t) \cos(\omega_0 t + \phi_c(t)) = x_n(t + \Delta\tau_n(t)), \quad (3.1)$$

$$x_n(t) = A_n(t) \cos(\omega_0(t - \Delta\tau_n(t)) + \phi_n(t)), \quad (3.2)$$

in which $A_c(t) = A_n(t + \Delta\tau_n)$ and $\phi_c(t) = \phi_n(t + \Delta\tau_n)$. Without loss of generality, the initial phase of the local oscillator is assumed to be zero and thus the baseband complex signal $\tilde{x}_n(t)$ in the n -th Rx-channel is given by:

$$\tilde{x}_n(t) = I_n(t) + j \cdot Q_n(t), \quad (3.3)$$

$$I_n(t) = A_n(t) \cos(\phi_n(t) - \omega_0 \Delta\tau_n), \quad (3.4)$$

$$Q_n(t) = A_n(t) \sin(\phi_n(t) - \omega_0 \Delta\tau_n), \quad (3.5)$$

where $I_n(t)$ and $Q_n(t)$ denote the baseband in-phase and quadrature components respectively. Through appropriate sample selection, the digital delay line is capable of fulfilling a rough time delay $\Delta\tau'_n(t)$, which is a multiple of the sampling interval T_s , given by:

$$\Delta\tau'_n(t) = \text{INT} \left[\frac{\Delta\tau_n}{T_s} \right] \cdot T_s = k_n \cdot T_s, \quad (3.6)$$

where $\text{INT}[\cdot]$ denotes the operation of rounding a number to its nearest integer k_n and t indicates a function of time, which will not be shown hereafter for denotation simplicity. As the rough delay can be implemented by sample selection. The residual phase angle corresponds to the residual time delay (that has not yet been fulfilled) is given by:

$$\Phi_{resb,n}(t) = \omega_0(\Delta\tau_n - \Delta\tau'_n). \quad (3.7)$$

3.1. Digital baseband phase rotation beamformer

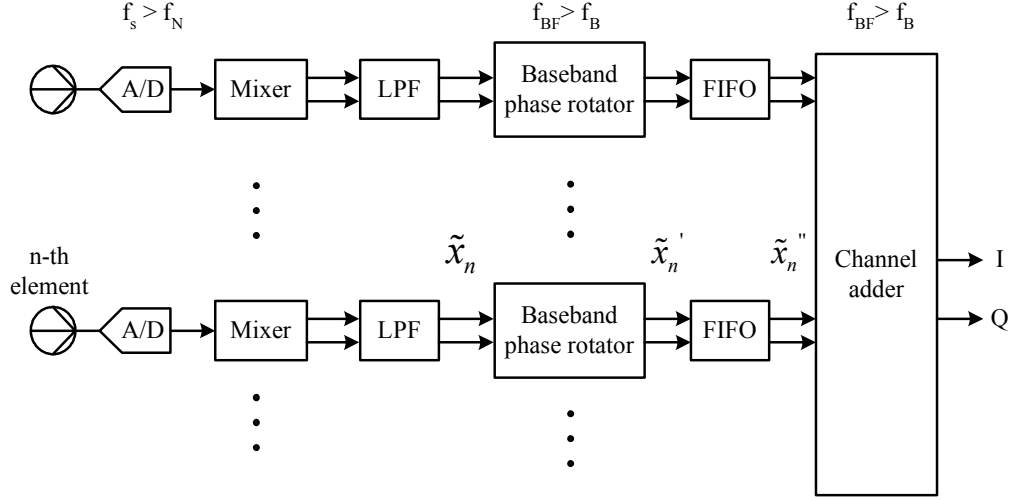


Figure 3.1: Diagram of a pre-filtering baseband PRB

If $\Phi_{resb,n}(t)$ is added to the baseband complex signal, the signal in the n -th Rx-channel ready for beamsum $\tilde{x}_n''(t)$, as depicted in Figure 3.1, can be expressed as:

$$\tilde{x}_n''(t) = I_n''(t) + j \cdot Q_n''(t) , \quad (3.8)$$

$$I_n''(t) = A_n(t + \Delta\tau_n') \cos[\phi_n(t + \Delta\tau_n') - \omega_0 \Delta\tau_n + \Phi_{resb,n}(t)] , \quad (3.9)$$

$$Q_n''(t) = A_n(t + \Delta\tau_n') \sin[\phi_n(t + \Delta\tau_n') - \omega_0 \Delta\tau_n + \Phi_{resb,n}(t)] . \quad (3.10)$$

However, Chang *et al.* pointed out that the phase difference among all Rx-channels for perfect focusing should be zero. Therefore, instead of $\Phi_{resb,n}(t)$ given by 3.7, the required rotation angle for phase compensation in the n -th Rx-channel should be:

$$\Phi_{totalb,n}(t) = \omega_0 \cdot \Delta\tau_n , \quad (3.11)$$

3.1. Digital baseband phase rotation beamformer

thus yielding:

$$I_n''(t) = A_n(t + \Delta\tau_n') \cos[\phi_n(t + \Delta\tau_n')] , \quad (3.12)$$

$$Q_n''(t) = A_n(t + \Delta\tau_n') \sin[\phi_n(t + \Delta\tau_n')] . \quad (3.13)$$

Using time delay $\Delta\tau_n'$ given in equation 3.6 to approximate the ideal required delay $\Delta\tau_n$ can be easily tolerated for both $A_n(t)$ and $\phi_n(t)$ as they are slow varying functions of time. In the following discussion, the phase compensation angle as given by equation 3.11 will be always considered for the baseband phase rotation.

The pre-filtering baseband PRB might be lack of efficiency in terms of hardware complexity since two complicated digital FIR filters are required in each Rx-channel. Agarwal *et al.* suggested the rearrangement of the demodulation filtering and beamforming delay [23], referred to as the post-filtering baseband PRB depicted in Figure 3.2. In this scheme, the number of low pass FIR filters required for quadrature demodulation is significantly reduced by a factor of N_e , with N_e being the number of array elements. Despite the fact that the time variant operation involved in dynamic receive focusing introduces asynchronous artifacts, they demonstrated that the post-filtering configuration can yield a comparable image quality to the quadrature sampling based pre-filtering PRB. Nonetheless, to avoid spectral aliasing, a higher beamforming frequency, which is above the Nyquist frequency (*i.e.* $f_{BF} \geq f_N$), is required as the mixed sum frequency persists in the sample stream immediately after beamforming summation [23].

3.1. Digital baseband phase rotation beamformer

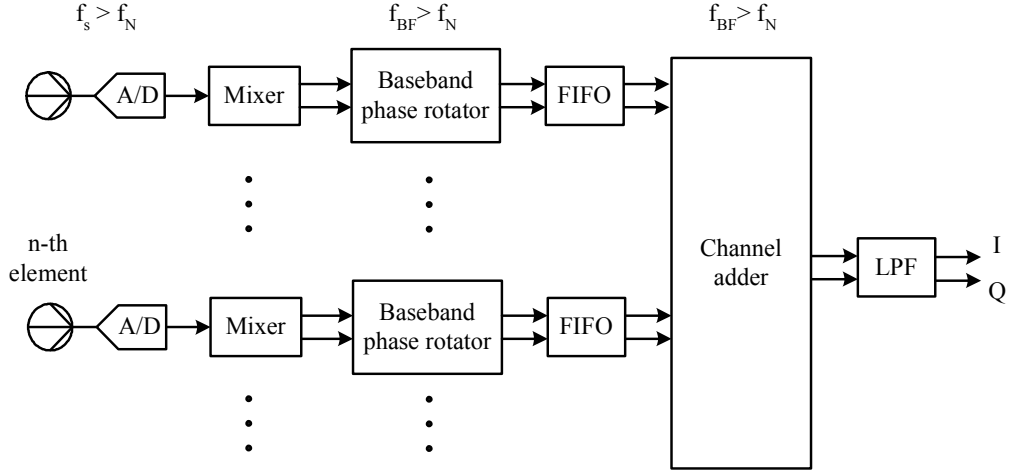


Figure 3.2: Diagram of a post-filtering baseband PRB

3.1.2 Baseband phase rotation using CORDIC

Notice that the phase compensated baseband signal $x'_n(t)$ is given by:

$$\tilde{x}'_n(t) = \tilde{x}_n(t) \cdot e^{j \cdot \Phi_{totalb,n}(t)} , \quad (3.14)$$

which essentially rotates the baseband complex signal $\tilde{x}_n(t)$ by an angle of $\Phi_{totalb,n}(t)$. O'Donnell *et al.* suggested that the CoOrdinate Rotation Digital Computer (CORDIC) can be used to realize the baseband phase rotation. Since the phase compensation principle is different from that earlier disclosed in [18], this section investigates the tolerance of CORDIC approximation for obtaining a favorable beamforming performance, particularly in a post-filtering baseband PRB.

CORDIC algorithm

CORDIC is primarily a method for computing elementary functions using minimal hardware [24], in which the rotation of a complex number by an angle β is executed in several steps. Each step completes a small part of the rotation β_m . The sum of

3.1. Digital baseband phase rotation beamformer

all iteration angles is equal to the required rotation angle, namely,

$$\beta = \sum_{m=1}^M S_m \cdot \beta_m , \quad (3.15)$$

in which $S_m = \{+1, -1\}$. Thus, the phase compensated baseband signal can be denoted as:

$$\begin{bmatrix} I_{n,m} \\ Q_{n,m} \end{bmatrix} = \cos \beta_m \begin{bmatrix} 1 & -S_m \tan \beta_m \\ S_m \tan \beta_m & 1 \end{bmatrix} \begin{bmatrix} I_{n,m-1} \\ Q_{n,m-1} \end{bmatrix} , \quad (3.16)$$

in which $I_{n,m}$ and $Q_{n,m}$ represent the I/Q components after the m -th iteration respectively. By appropriate selection of β_m given by $\beta_m = \tan^{-1}(1/2^{m-1})$, as presented in Table 3.1, operations on real and imaginary parts are merely binary digit shifts and additions except for an accumulative factor

$$K_M = \prod_{m=1}^M \cos \beta_m , \quad (3.17)$$

defined as the aggregate factor. In practice, K_M can be executed once and possibly absorbed in the receive apodization stage.

Table 3.1: CORDIC angles

index	1	2	3	4	5	...
β_m	45.0°	26.6°	14.0°	7.1°	3.6°	...

The CORDIC algorithm converges within the range given by [25]:

$$\sum_{m=1}^{\infty} \tan^{-1} \frac{1}{2^{m-1}} \approx 1.7433 \text{ rad} = 99.88^\circ . \quad (3.18)$$

Hence, a preprocessor is required to fulfill the rotation angle larger than 90° .

3.1. Digital baseband phase rotation beamformer

Notice that rotation by multiples of 90° (e.g. 90° and 180°) is performed by merely inverse and swap operation on real and imaginary parts of the complex number. The CORDIC rotator is thereby capable of accomplishing the baseband phase rotation without multiplication.

Image quality evaluation

To investigate the effects on image quality due to the approximation of the phase rotation CORDIC angle, a wire target phantom, consisting of six wires in a water tank, is used for performance evaluation. The pre-beamformed radio-frequency (RF) raw data, available at <http://bul.eecs.umich.edu>, were acquired using a 128-element, 3.5 MHz phased array transducer (Acuson, Model #V328). A 10-bit ADC was used in each Rx-channel to sample the echo signals at 13.9 MHz with synthetic aperture. Using the synthetic aperture data, the transmit focusing was simulated at 60 mm with a transmit f -number of 2. This set of data is hereafter referred to as the Acuson data set. The results obtained by an interpolation beamformer, with an interpolation factor of 8 (i.e. $f_{eff} = 8 \times f_s = 111.1$ MHz), were plotted for comparison as shown in Figure 3.3. As reflected in Figure 3.4, a consistently better beamforming performance in terms of lateral and axial resolution can be achieved as the number of iterations (CORDIC stages) increases from 2 to 5. In addition, it is found that the axial profile achieved by the 4-stage CORDIC rotator is very close to that of the accurate angle rotation, as shown in Figure 3.4(h). The margin for further performance improvement is thus small.

3.1. Digital baseband phase rotation beamformer

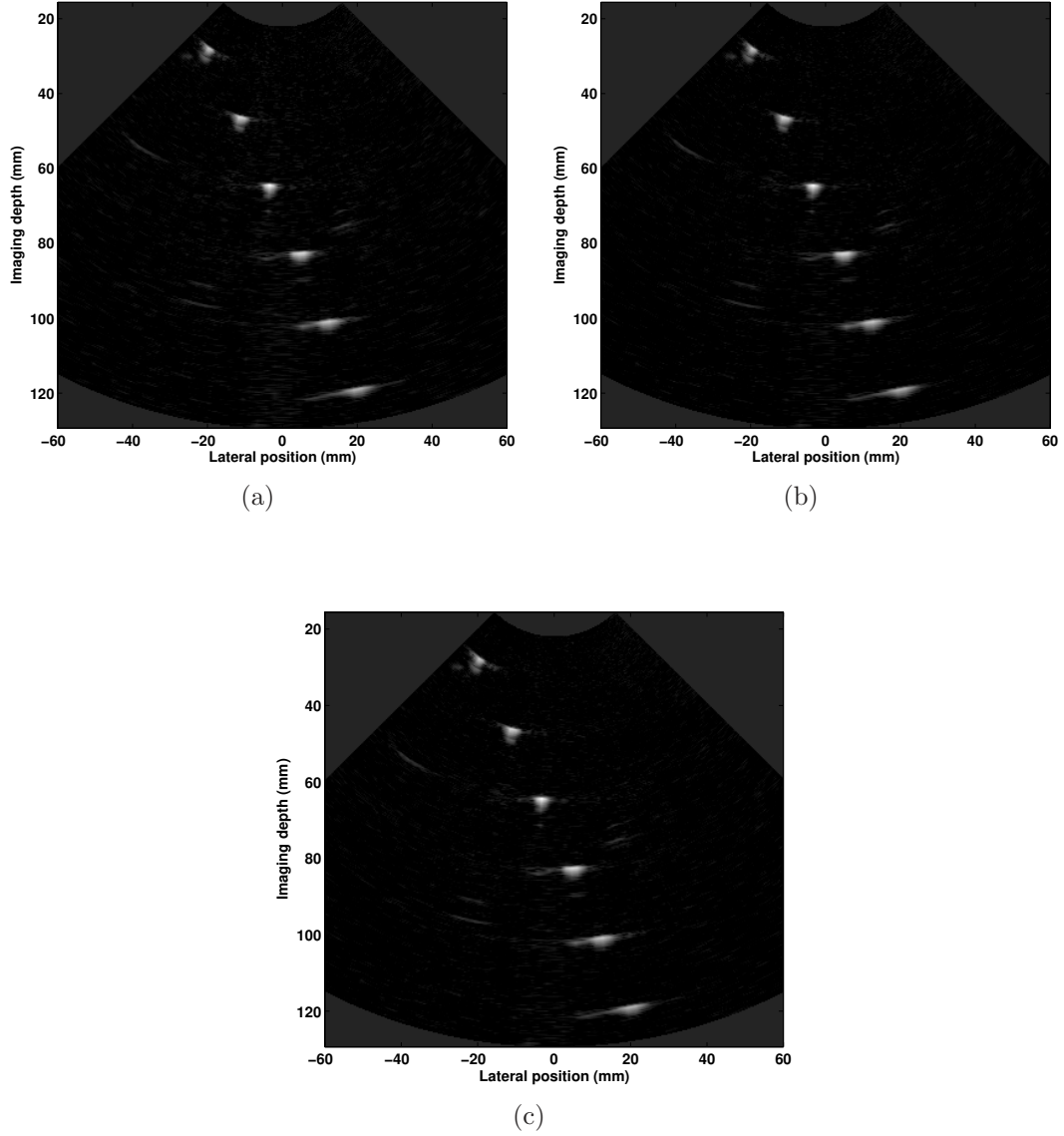


Figure 3.3: Gray scale images with 70 dB dynamic range produced by (a) the interpolation beamformer, (b) post-filtering baseband PRB (BBPRB) with accurate angle rotation and (c) post-filtering BBPRB with approximated angle rotations by using 4-stage CORDIC rotators

3.1. Digital baseband phase rotation beamformer

Table 3.2: Preliminary hardware evaluation results

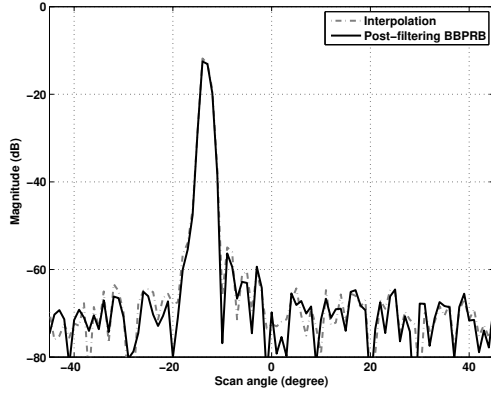
implementation	CORDIC rotator number of stages				complex multiplier
	2	3	4	5	
number of LE	100	152	181	215	530
resources (%)	18.9	28.7	34.2	40.6	100

Hardware evaluation

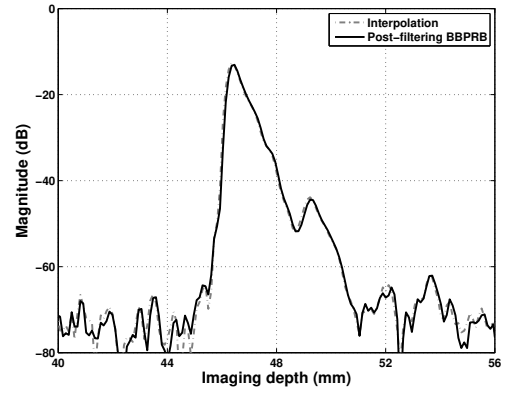
A pipelined CORDIC rotator is designed using Altera Stratix® FPGA (model EP1S10F484C5) to investigate the hardware cost by employing the CORDIC rotator and complex number multiplier for baseband phase rotation respectively. Figure 3.5 illustrates the block diagram of an arbitrary stage of a CORDIC rotator, which is essentially the hardware embodiment of equation 3.16 without accounting for the factor $\cos \beta_m$. Notice that β'_m here denotes the angle that has not yet been fulfilled while the CORDIC angle for the m -th iteration β_m is stored in LUT. By means of sign-bit extraction, β'_m determines the value of S_m (e.g. $S_m = 1$ for a positive β'_m and $S_m = -1$ for a negative β'_m), based on which appropriate additions/subtractions are performed to accomplish the multiply-less angle rotation of β_m . In addition, β'_m is being updated at the same time, ready for the input of the next stage.

Table 3.2 presents the estimated hardware cost in terms of consumed logic elements (LE) for a 10-bit input CORDIC rotator. The 4-stage CORDIC rotator takes 34.2 % hardware resources in terms of used logic elements as compared to a complex multiplier comprising 4 digital multipliers (10-bit input, 20-bit output designed by the library of parameterized modules (LPM) provided by Altera) and 2 adders (20-bit input, 21-bit output designed by LPM).

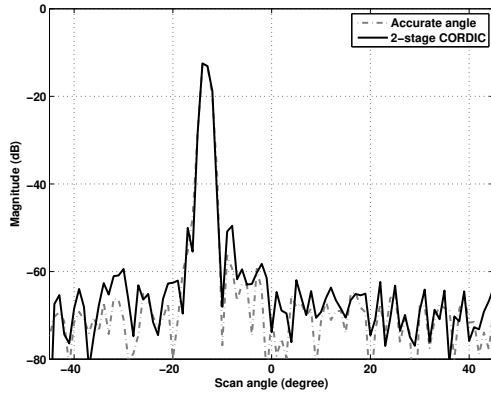
3.1. Digital baseband phase rotation beamformer



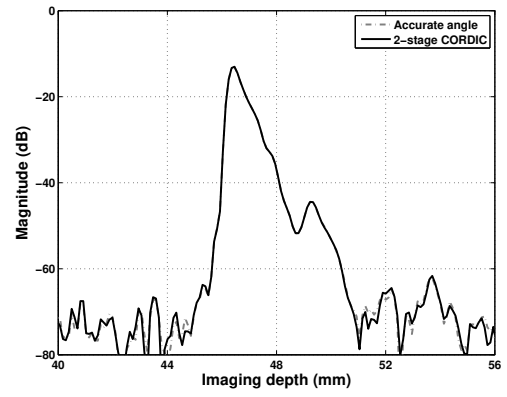
(a)



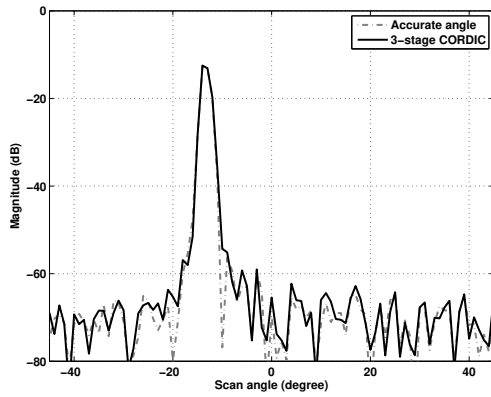
(b)



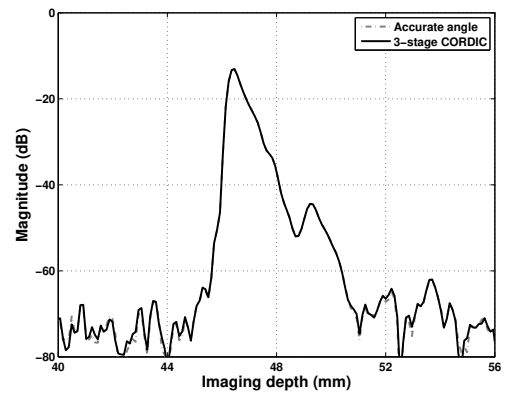
(c)



(d)



(e)



(f)

3.1. Digital baseband phase rotation beamformer

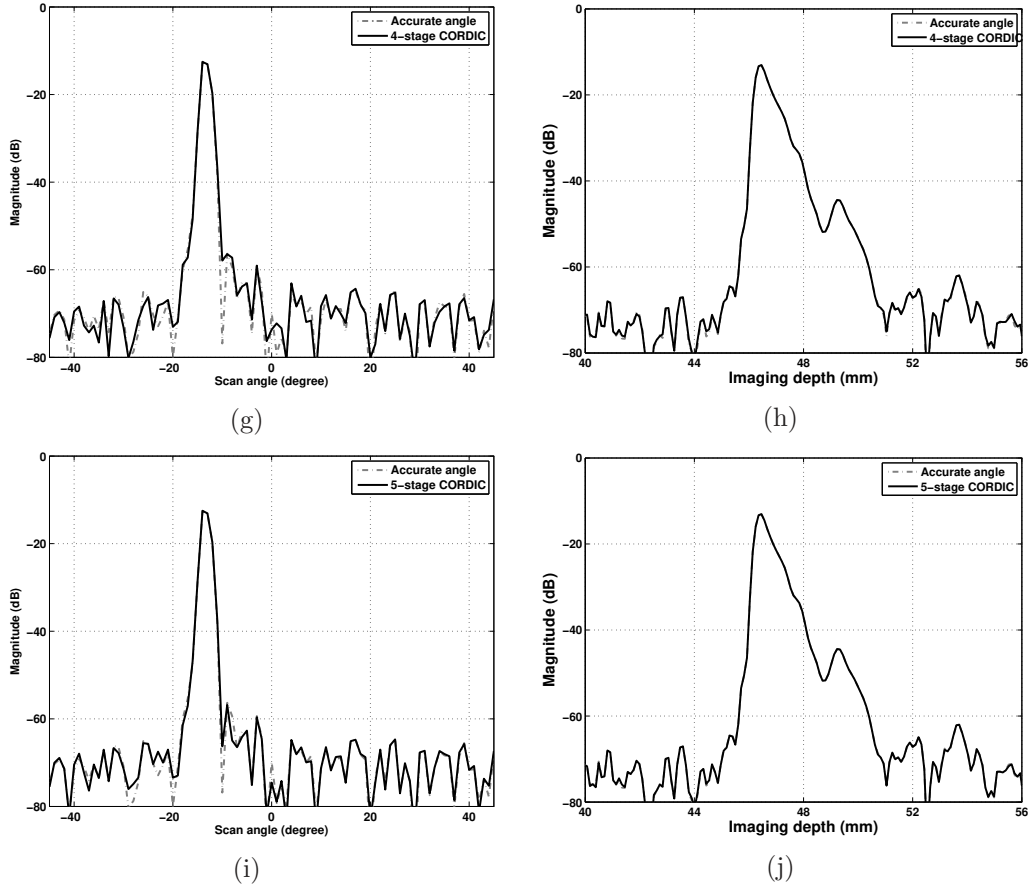


Figure 3.4: Lateral and axial profiles of the 2nd wire target (from the top) in the post-filtering baseband PRB with (a) (b) accurate angle rotation and approximated angle rotations by using CORDIC rotators with 2 to 5 stages (c)-(j)

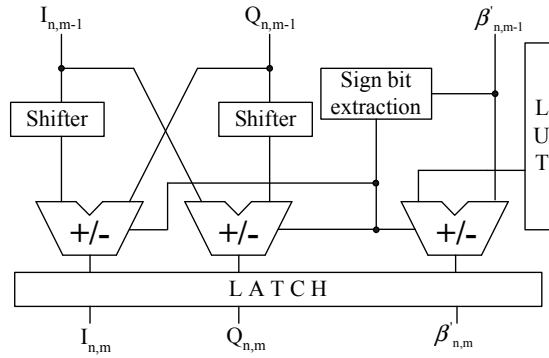


Figure 3.5: Diagram of single stage CORDIC rotator

3.2 Digital heterodyning phase rotation beamformer

Section 3.1.1 has shown that the required phase compensation for $x_n(t)$ in the baseband phase rotation beamforming does not correspond to the residual delay $\Delta\tau'_n$ that has yet been fulfilled, but the total required time delay $\Delta\tau_n$. In fact, the concept of two-step delay fulfillment originated from the heterodyning PRB, or termed intermediate frequency (IF) beamformer, disclosed by Maslak *et al.* [26–28]. This section demonstrates that to fulfill the residual delay through phase rotation is valid for the heterodyning PRB. A digital heterodyning PRB (digital IF beamformer) based on this principle is thereafter developed to simplify the beamformer data path logic to merely one digital multiplier with necessary digital buffers per channel.

3.2.1 Prior art

In 1979, Maslak disclosed an analog beamformer capable of performing dynamic focusing without involving the expensive analog tap selectors [26]. The synchronous dynamic focusing beamformer proposed later by Manes *et al.* essentially employed the same principle [29]. Figure 3.6 illustrates the scheme of this IF beamforming technique. In particular, a local oscillator of frequency f_r , with $\omega_r = 2\pi f_r$ being

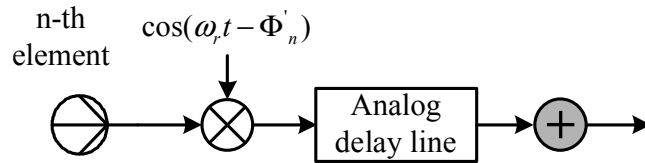


Figure 3.6: Schematics of analog IF beamforming

3.2. Digital heterodyning phase rotation beamformer

the angular frequency, is used in each Rx-channel to mix the echo down to an IF signal, whilst the accompanying phase adjustment $\Phi'_n(t)$ ensures that the heterodyned IF signal $x'_n(t)$ in the n -th Rx-channel is properly phase compensated to achieve the desirable phase coherence. The phased compensated signal $x'_n(t)$ is given by:

$$\begin{aligned} x'_n(t) = & A_n(t) \cos(\omega_0(t - \Delta\tau_n) + \phi_n(t) + \omega_r(t - \Delta\tau_n) + \Phi'_n(t)) \\ & + A_n(t) \cos(\omega_0(t - \Delta\tau_n) + \phi'_n(t) - \omega_r(t - \Delta\tau_n) - \Phi'_n(t)) . \end{aligned} \quad (3.19)$$

Assuming that the difference frequency component, *i.e.* the 2nd item in equation 3.19, (the sum frequency component, *i.e.* the 1st item in equation 3.19, is also applicable) is used for final image formation and the subsequent analog delay line would apply a rough delay of $\Delta\tau'_n$, the signal $x''_n(t)$ ready for beamforming summation is given by:

$$x''_n(t) = A_n(t + \Delta\tau'_n) \cos((\omega_0 - \omega_r)t - (\omega_0 - \omega_r)(\Delta\tau'_n - \Delta\tau_n) + \phi_n(t + \Delta\tau'_n) - \Phi'_n(t)) , \quad (3.20)$$

in which the sum frequency component has been removed (filtered by the analog delay line). To achieve optimum phase coherence, it is apparent that the required phase angle should be dynamically updated as:

$$\Phi'_n(t) = -(\omega_0 - \omega_r) \cdot (\Delta\tau_n - \Delta\tau'_n) , \quad (3.21)$$

thus yielding:

$$x''_n(t) = A_n(t + \Delta\tau'_n) \cdot \cos((\omega_0 - \omega_r)t + \phi_n(t + \Delta\tau'_n)) . \quad (3.22)$$

3.2. Digital heterodyning phase rotation beamformer

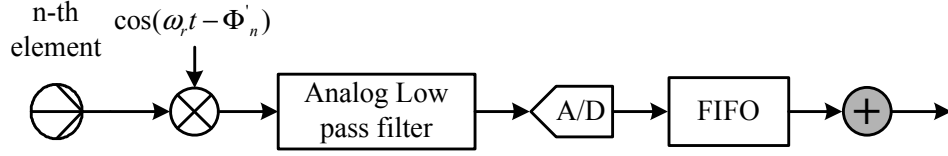


Figure 3.7: Schematics of hybrid IF beamforming

As compared to equation 3.11, the carrier frequency for phase angle computation is heterodyned to $\omega_r - \omega_0$ and the phase compensation only needs to take account of the residual delay, *i.e.* $\Delta\tau_n - \Delta\tau'_n$.

In order to minimize the noise caused by tap switching transient, Maslak suggested that only one tap setting could be used for the analog delay line (*i.e.*, the analog delay line fulfills a static time delay). Additionally, dynamic focusing is achieved by performing the phase adjustment $\Phi'_n(t)$ dependent on the time t (or image depth). However, changing the phase angle $\Phi'_n(t)$ continuously so as to provide perfect phase coherence for all ranges would be very expensive. Maslak claimed that phase coherence within 22.5° might have been satisfactory [26].

A later disclosed embodiment achieved an improved dynamic range by replacing the analog delay line with digital delay elements [27, 28]. Therefore, the system is capable of performing noiseless dynamic rough delay as depicted in Figure 3.7. However, to remove the sum frequency component produced in the heterodyning stage, an analog low pass filter with sharp roll-off response is required in each Rx-channel to avoid spectral aliasing. In addition, the signal has to pass through 2 dynamic range limiting components, *i.e.* an imperfect mixer as well as an analog filter. The combination of these two devices in practice would yield a smaller dynamic range, as compared to a fully digital system using one ADC per channel only [8].

3.2. Digital heterodyning phase rotation beamformer

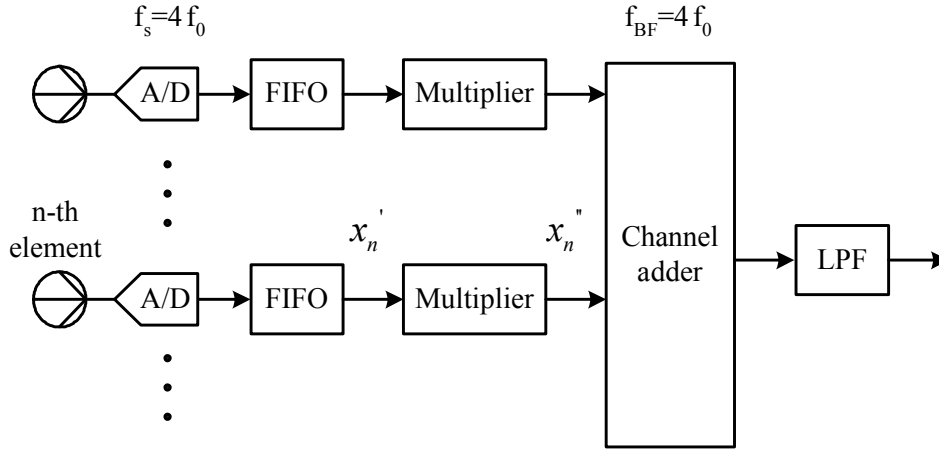


Figure 3.8: Block diagram of a digital heterodyning PRB

3.2.2 Fully digital embodiment

To achieve a favorable system dynamic range, a fully digital heterodyning PRB is developed to overcome limitations of the systems so-far disclosed. In the proposed system as shown in Figure 3.8, the echoes are sampled by an ADC above the Nyquist frequency f_N in individual Rx-channel immediately after the required pre-processing (*e.g.* analog amplification and anti-aliasing filtering). The digital delay line realizes the rough delay through appropriate sample selection, followed by the phase fine delay residing in the heterodyning stage. Thus, the phase angle $\Phi'_n(t)$ can be updated in real time and maintained at high accuracy using a digital multiplier. The dynamic range of the present system will be primarily affected by the intrinsic ADC quantization effects only. After beamforming summation, the output sequence is then passed through a digital low pass filter to remove the dummy sum frequency component produced in the partial demodulation stage. As a result, only one low pass FIR filter is required for the whole beamformer system.

It is well established that ADCs need to sample an arbitrary continuous time signal above f_N so as to avoid spectral aliasing. Figure 3.9(a) depicts the resulting

3.2. Digital heterodyning phase rotation beamformer

spectrum when a minimum sampling rate of $f_s = 3 \cdot f_0$ is used to sample the received echo being of 100 % fractional bandwidth, *i.e.* $f_B/f_0 = (f_H - f_L)/f_0 = 1$. In a fully digital heterodyning beamformer, the involved partial demodulation, which yields the sum and difference frequency components, requires a slightly higher sampling rate to avoid aliasing. In particular, to make full use of the available frequency band, the local oscillation frequency is configured to be $f_r = 1.5 \cdot f_0$ so that the mixed components would butt against each other at the zero frequency. A sampling rate of $f_s = 4 \cdot f_0$ can favorably avoid the aliasing as shown in Figure 3.9(b). More generally, the sampling rate f_s should comply with (See Appendix B):

$$2 \cdot (f_0 + f_B) \leq f_s \leq 4 \cdot f_0 , \quad (3.23)$$

subject to $f_H \leq 3 \cdot f_L$ (*i.e.* a fractional bandwidth no larger than 100 %), which can be usually satisfied in the state-of-the-art systems. Alternatively, an increased sampling rate, given by:

$$f_s \geq 4 \cdot f_0 + 2 \cdot f_B , \quad (3.24)$$

is also capable of performing the partial demodulation free of aliasing. Figure 3.9(c) illustrates a particular example of this theme in which $f_B = f_0$.

Unlike its analog embodiment, the digital heterodyning PRB fulfills the rough delay through digital sample selection prior to the fine delay realized by phase compensation. This rearrangement in principle is of particular significance in a digital heterodyning PRB, which essentially enables each beamformed sample to be in perfect focusing. Notice that the relative time delay $\Delta\tau_n$ decreases as the image depth increases and the fulfilled delays through sample selection in a digital beamformer are always quantized to units of sampling period as reflected in equation 3.6. Thus, a digital sample is said to be repeated when the quantized

3.2. Digital heterodyning phase rotation beamformer

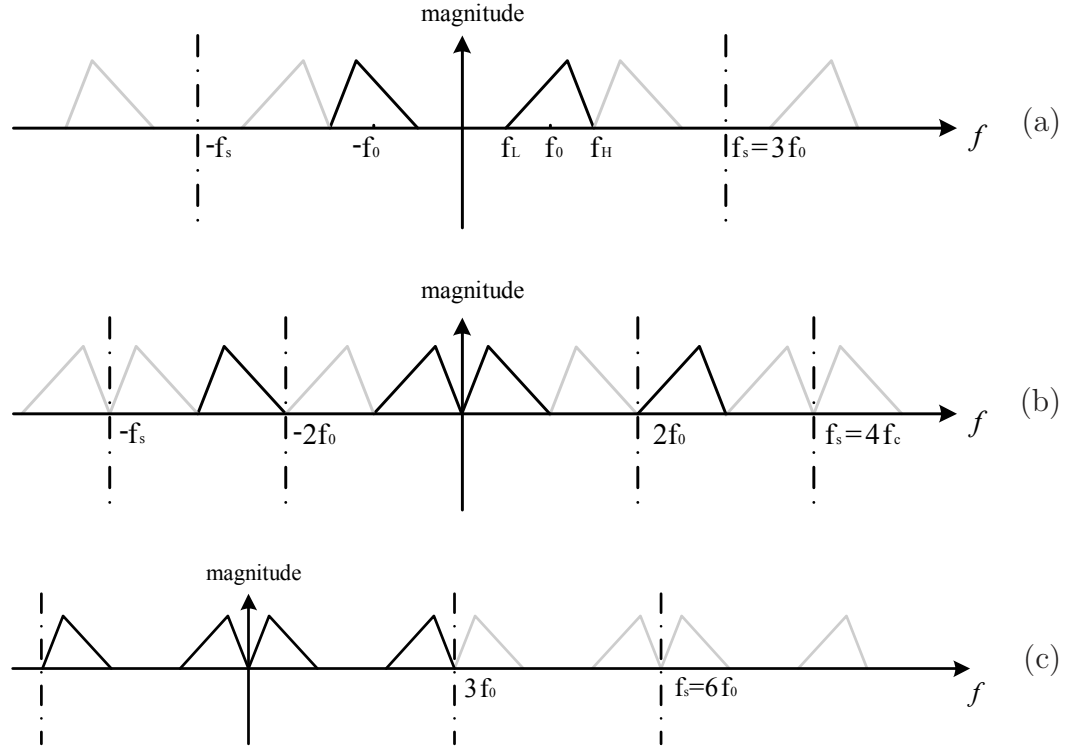


Figure 3.9: Replicative spectrum in a common low pass signal sampling scheme (a), a digital heterodyning PRB (b), and a digital heterodyning PRB with an increased sampling rate (c) with dark lines representing the spectrum of the original analog signal and gray lines representing the replicative spectra due to discrete time sampling

relative time delay keeps unchanged as the time t increases [30,31]. In other words, an echo sample might be used twice for generation of the beamforming output sequence. Consequently, the relative rough delays applied on these two occurrences take on a difference of T_s (*i.e.*, $\Delta\tau'_n$ in equation 3.21 decreases by an amount of T_s), yet the difference in their required relative delays is not necessarily to be T_s (*e.g.*, $\Delta\tau_n$ in equation 3.21 decreases by an amount of $0.5 \times T_s$ as specified by the beamforming delay update). According to equation 3.21, different phase delays, *i.e.*, $\Phi'_n(t_1)$ and $\Phi'_n(t_2)$ should be applied on these two occurrences respectively. Such operation in practice can be easily realized by updating the multiplicand of the channel digital multiplier for each beamformed sample. On the other hand,

3.2. Digital heterodyning phase rotation beamformer

however, it is necessary to bear in mind that the rough delay is restricted to multiples of T_s and thereby of less flexibility. By performing fine delay first would incur difficulty in accurately updating the rough delays for both of these two occurrences. Assuming that, for a particular sample, the phase delay $\Phi'_n(t_1)$ is configured to compensate the phase lag of its first occurrence, it would be infeasible through sample selection for its second occurrence, having undergone a phase delay of $\Phi'_n(t_1)$, to accurately fulfill the residual time delay given by $\Delta\tau(t_2) - \Phi'_n(t_1)/(\omega_r - \omega_0)$, which in practice is unnecessarily to be multiples of T_s .

Notice that the heterodyned IF signal is of a lower carrier frequency $f_r - f_0$ and therefore the phase coherence can be more easily tolerated in case $\Phi'_n(t)$ is not real time updated. Alternatively, in a preferred embodiment, the instantaneous value of the local oscillation signal can be pre-calculated and stored in a LUT so that perfect phase coherence can be achieved for each sample throughout the whole imaging range. In addition, the receive apodization in practice can be absorbed in the same multiplier to further reduce the hardware cost.

3.2.3 Image quality evaluation

Simulation and phantom studies were carried out to analyze the performance of the proposed heterodyning PRB.

Simulation results

The simulation model was developed by utilizing the commonly used software Field II [32]. The simulated pre-beamformed RF data were generated by using a 3.5 MHz, linear transducer using 64 active elements for both transmit and receive.

3.2. Digital heterodyning phase rotation beamformer

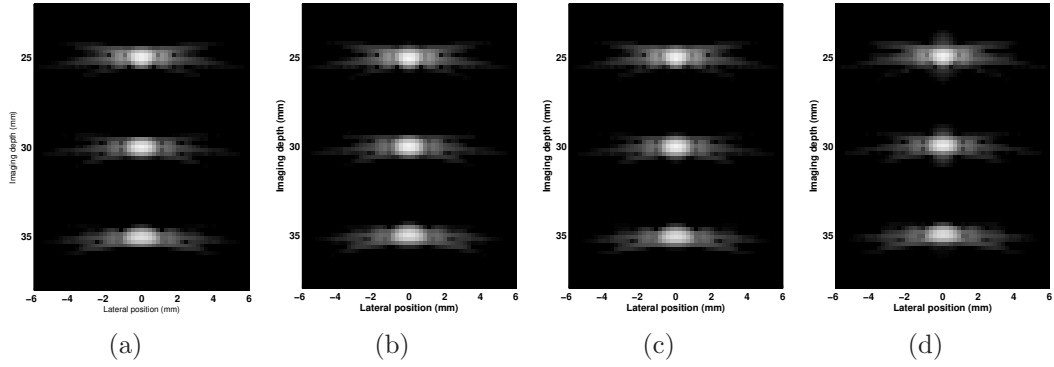


Figure 3.10: Gray scale images of point targets by (a) interpolation beamformer (b) pre-filtering BBPRB (c) post-filtering BBPRB and (d) heterodyning PRB

The - 6 dB fractional bandwidth is 60 % and transmit focusing was applied at 30 mm, which has an f -number of two. The received data were sampled at a rate of 14 MHz. Rectangular apodization was used in both transmit and receive. The sound speed is 1540 m/s. Figure 3.10 shows the simulation results when different beamforming algorithms were applied.

Figure 3.11(b) shows that as compared to other 3 methods, there is no significant degradation in lateral resolution incurred for the heterodyning PRB. The axial resolution of heterodyning PRB is affected due to its restriction on the limited bandwidth. Transducers with -6 dB fractional bandwidth down to 45 % and 30 % were used in the simulation to investigate the bandwidth effects on the beamforming performance. With other parameters unchanged, Figure 3.12 and 3.13 show that the difference in axial profile between heterodyning PRB and the interpolation beamformer becomes less as the transducer bandwidth decreases. In addition, the absolute axial resolution is degraded as a result of the reduced echo bandwidth.

Using the same parameter, a simulated cyst phantom was used to examine the contrast performance of the heterodyning PRB. An anechoic cyst with a radius

3.2. Digital heterodyning phase rotation beamformer

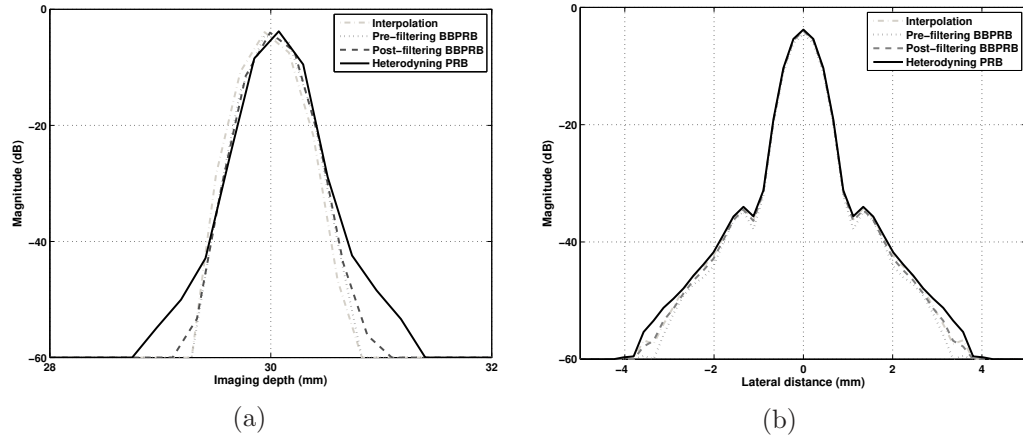


Figure 3.11: Simulation results of axial and lateral profiles of the point target at 30 mm with 60 % -6 dB transducer fractional bandwidth

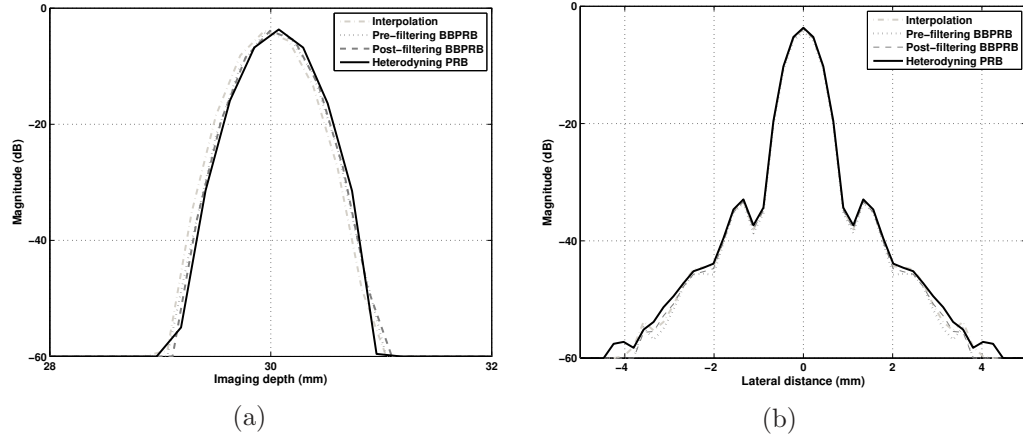


Figure 3.12: Simulation results of axial and lateral profiles of the point target at 30 mm with 45% -6 dB transducer fractional bandwidth

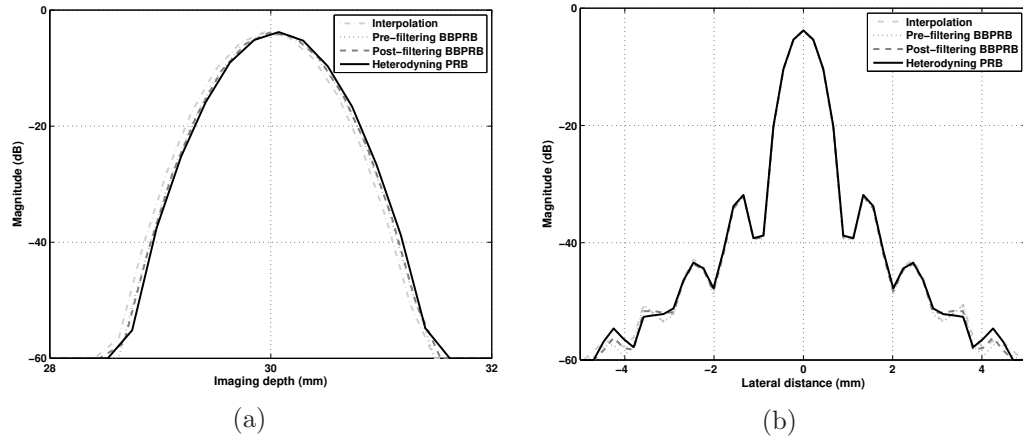


Figure 3.13: Simulation results of axial and lateral profiles of the point target at 30 mm with 30 % -6 dB transducer fractional bandwidth

3.2. Digital heterodyning phase rotation beamformer

of 6 mm was placed at 30 mm in front of the transducer. The results are shown in Figure 3.14. To quantitatively compare the performance, the contrast-to-noise-ratio (CNR) was computed by [33,34]:

$$CNR = \frac{|\mu_1 - \mu_2|}{\sqrt{\sigma_1^2 + \sigma_2^2}}, \quad (3.25)$$

where μ_1 and σ_1^2 are the mean and variance of intensities of pixels in a region of interest (ROI), i.e., the squared region 12 by 12 pixels centered at the center of the cyst, and μ_2 and σ_2^2 are the mean and variance of intensities of pixels in a background region that locates at the same depth and has the same size as the ROI to be compared with. Table 3.3 presents the CNR values for different methods. The heterodyning PRB presents a CNR loss of 6.8 % as compared to the interpolation beamformer.

Table 3.3: CNR value from the simulated cyst phantom

Method	CNR	Normalized CNR
Interpolation beamformer	9.83	1.000
Pre-filtering BBPRB	9.25	0.941
Post-filtering BBPRB	9.74	0.991
Heterodyning PRB	9.16	0.932

Phantom studies

To perform phantom study, the same set of wire-target phantom data is used to evaluate the performance of the proposed digital heterodyning PRB. The local oscillator frequency is set to be $f_r = 1.5 \times f_0 = 5.25$ MHz for partial demodulation, which implies that the fractional bandwidth of the echo signal is less than 100 %. Figure 3.15 shows the resulting image displayed with a 70 dB dynamic range. The difference in lateral and axial resolution as measured by the obtained - 6 dB beam

3.2. Digital heterodyning phase rotation beamformer

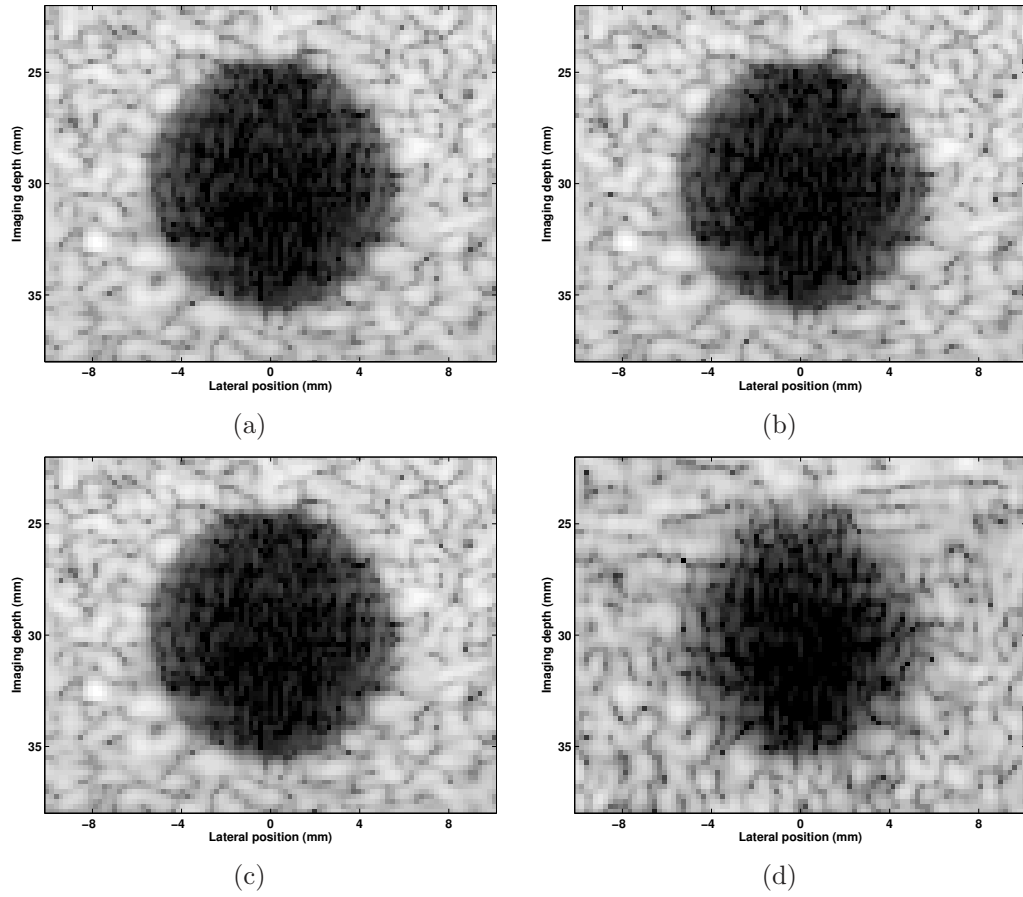


Figure 3.14: Gray scale images of a cyst by (a) interpolation beamformer (b) pre-filtering PRB (c) post-filtering PRB and (d) heterodyning PRB

3.2. Digital heterodyning phase rotation beamformer

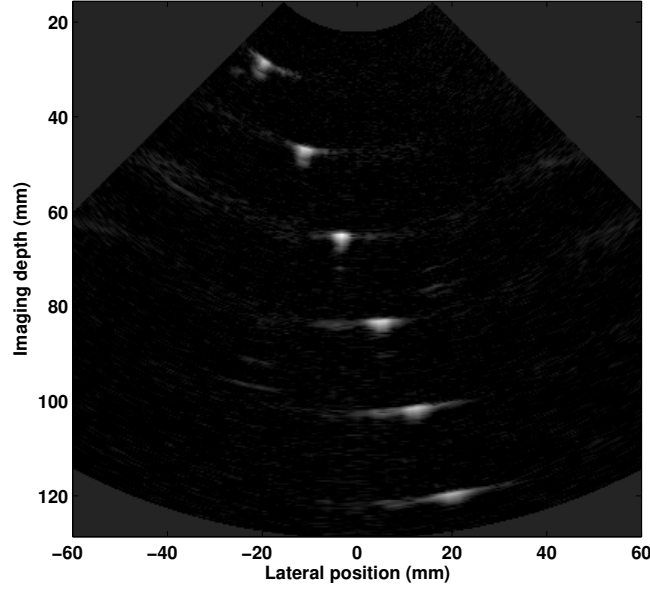


Figure 3.15: Gray scale image with 70 dB dynamic range produced by the heterodyning PRB

width between heterodyning PRB and the interpolation beamformer is negligible as reflected in 3.16. However, it has a broader beam width below - 40 dB which may affects the contrast resolution.

Phantom study was performed by using another set of multipurpose phantom (Model #539, ATS Laboratories, U.S.A.) data, collected by a 192-element 3.5 MHz convex array. An 8-bit ADC was used in each channel to sample the echo at 61.6 MHz. To better investigate the phase compensation effects on beamforming performance, the sample stream is decimated by a factor of two and thus the effective sampling rate in emulation is $f_s = 8.8 \times f_0 = 30.8$ MHz. Figure 3.17 indicates that the heterodyning PRB obtains a close axial profile in comparison to the interpolation beamformer and post-filtering BBPRB.

3.2. Digital heterodyning phase rotation beamformer

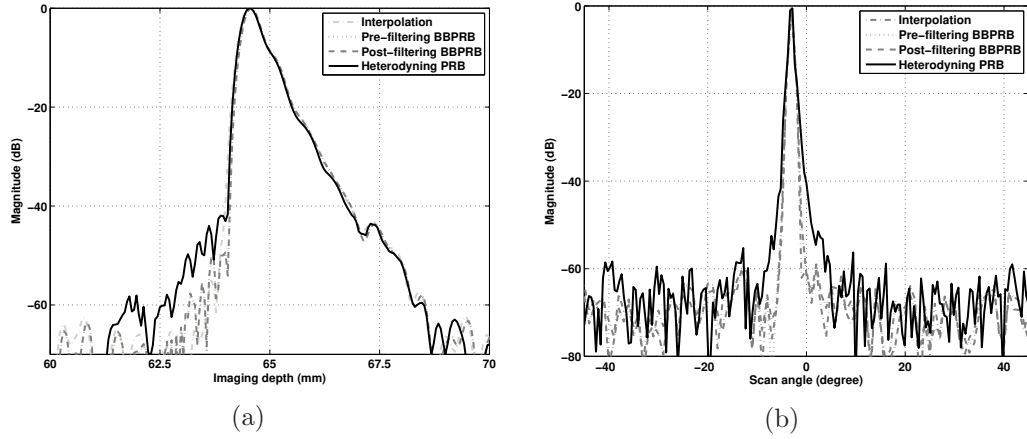


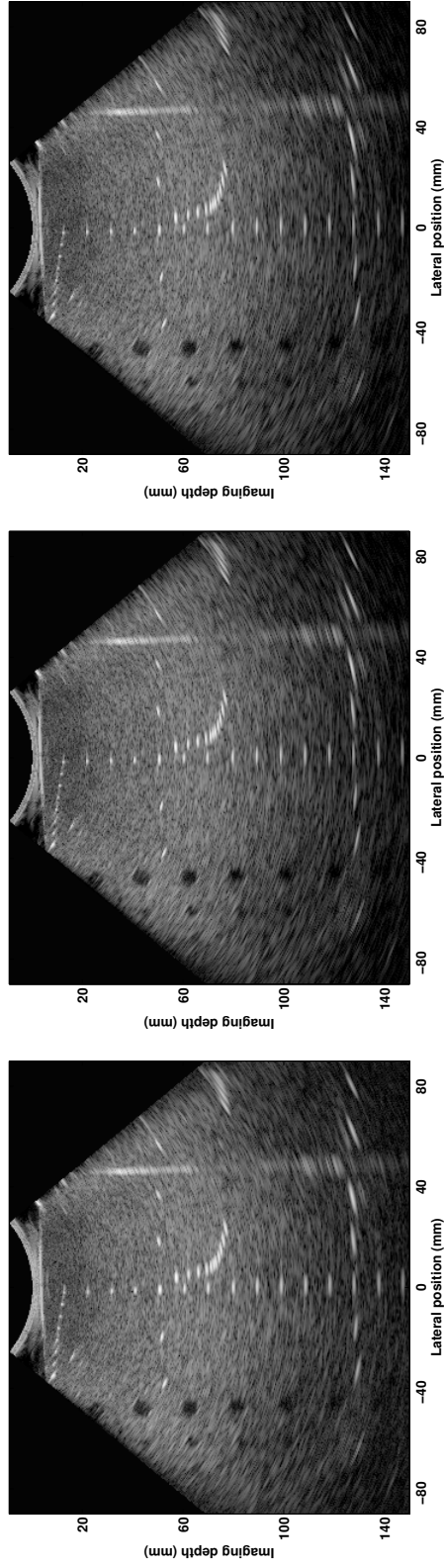
Figure 3.16: Axial (a) and lateral (b) profile of the third wire target (from the top)

3.2.4 Computational requirement

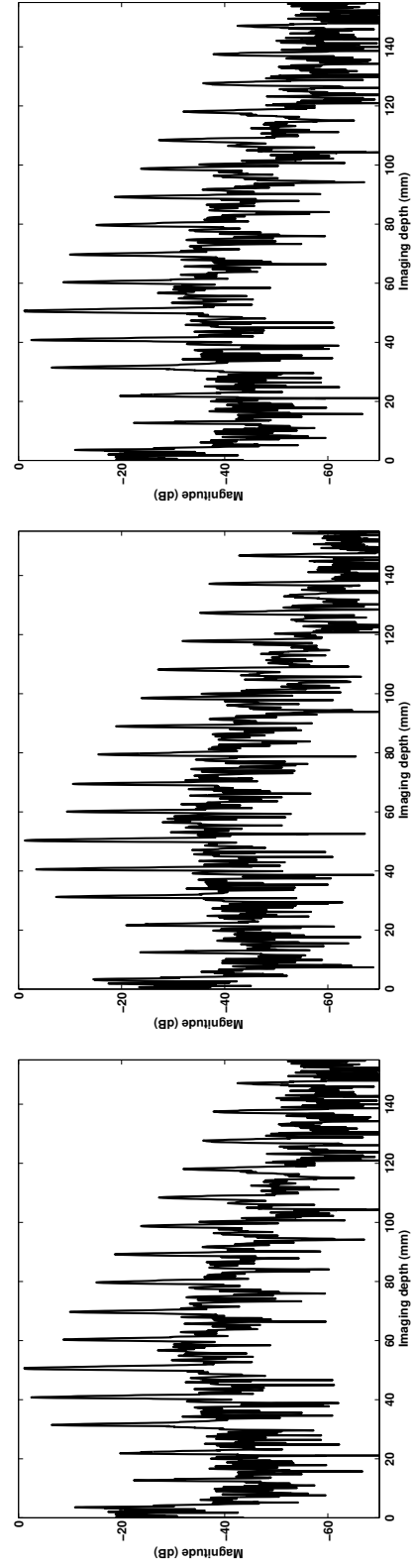
Table 3.4 lists the computational requirement of each processing function in the four beamforming methods. It is assumed that the ADC sampling frequency is equal to the beamforming frequency. By trading addition with multiplication, the post-filtering BBPRB employing 4-stage CORDIC rotators is also included for comparison. The phase adjustment in the interpolation beamformer refers to the upsampling (by zero-padding and low-pass interpolation filtering) and select the appropriate sample for coherent summation. In this analysis, $N_s = 2,048$ is the number of sample in each receive channel; $J = 16$ is the tap number of the demodulation filter; $\zeta = 5$ is the ratio of tap number of the interpolation filter to the interpolation factor [11]; $N_{ch} = 64$ is the number of active receive channel.

It is found that the heterodyning PRB can dramatically reduce the number of multiplications and additions as compared to the other three existing methods. Table 3.5 lists the heterodyning PRB's required number of multiplication and addition in percentage when different methods are used as references, e.g., the number of multiplication required with reference to the interpolation beamformer

3.2. Digital heterodyning phase rotation beamformer



(a) Gray-scale images with 70 dB dynamic range



(b) Central line A-mode plot

3.2. Digital heterodyning phase rotation beamformer

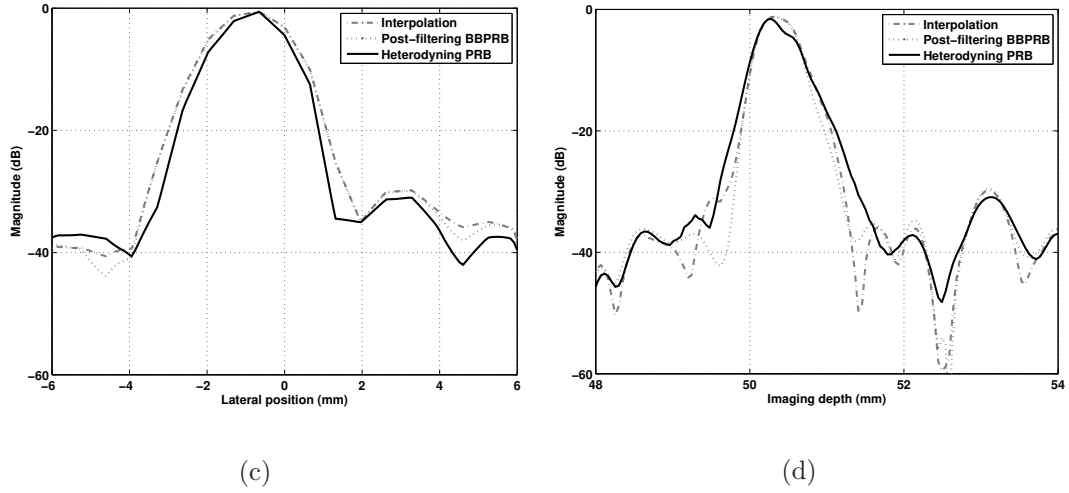


Figure 3.17: Phantom study results by the heterodyning PRB (left column), post-filtering BBPRB (mid-column), and interpolation beamformer (right column) in (a) and (b), zoomed axial plot along the scanline passing through the fifth wire target (from the top) (c) and zoomed lateral profile of the same target (d)

is $200,704/724,992 = 27.7\%$.

3.2. Digital heterodyning phase rotation beamformer

Table 3.4: Required number of multiplications and additions

Operation		Mixing	Demodulation filtering	Phase adjustment	Total
Interpolation beamformer	Multiplications	$2N_s$	$2JN_s$	$\zeta N_{ch} N_s$	724,992
	Additions	-	$2(J-1)N_s$	$(\zeta-1)N_{ch} N_s$	585,728
Pre-filtering BBPRB	Multiplications	$2N_{ch} N_s$	$2JN_{ch} N_s$	$4N_{ch} N_s$	4,980,736
	Additions	-	$2(J-1)N_{ch} N_s$	$2N_{ch} N_s$	4,194,304
Post-filtering BBPRB	Multiplications	-	$2JN_s$	$4N_{ch} N_s$	589,824
	Additions	-	$2(J-1)N_s$	$2N_{ch} N_s$	323,584
Post-filtering BBPRB using CORDIC	Multiplications	-	$2JN_s$	-	65,536
	Additions	-	$2(J-1)N_s$	$2N_{st} N_{ch} N_s$	1,110,016
Heterodyning PRB	Multiplications	$2N_s$	$2JN_s$	$N_{ch} N_s$	200,704
	Additions	-	$2(J-1)N_s$	-	61,440

3.3. Conclusion

Table 3.5: Computational requirement in percentage with reference to other beamforming techniques

Reference	Required number of multiplication	Required number of addition
Interpolation beamforming	27.7%	10.5%
Pre-filtering BBPRB	4.0%	1.5%
Post-filtering BBPRB	34.0%	19.0%
Post-filtering BBPRB using CORDIC	306.3%	5.5%

3.3 Conclusion

Phase rotation beamforming is a general kind of frequency domain beamforming technique, which employs phase adjustment to achieve the required phase coherence for spatial filtering. As compared to the interpolation beamformer, the pre-filtering BBPRB allows a reduced beamforming frequency. The post-filtering BBPRB disclosed by Agarwal *et al.* achieves a comparable image quality to the pre-filtering BBPRB with a significantly reduced hardware cost and/or computational requirement. The only imperfection is that it requires separate processing of the I/Q signals involved with complex number multiplication. By trading additions with multiplications, phase rotation by using a CORDIC rotator avoids the complex multiplication by iterative approximation. However, the increase in required number of additions may undermine its competence in terms of the overall number of operation. The negligible performance degradation in post-filtering

3.3. Conclusion

BBPRB facilitate the development of the high channel count systems in which reduction in the computational complexity with minimal compromise of the image quality is critical [23].

The proposed fully digital heterodyning PRB requires only one digital multiplier and digital buffers in an arbitrary Rx-channel. The echo phase coherence among respective Rx-channels is achieved by the phase compensation residing in the heterodyning stage. Therefore, ADCs in respective Rx-channels are allowed to sample the echo signal slightly above the Nyquist rate for high performance digital beamforming, provided that the fractional bandwidth of transducer is no more than 100 %. Simulation and phantom study results show that it can produce reasonable gray scale image quality in terms of spatial (measured by - 6 dB beamwidth) and contrast resolution with dramatically reduced computational complexity. In addition, the performance degradation is lowered when a narrower band transducer is used. Computational requirement analysis also shows that the heterodyning PRB can dramatically reduce the number of multiplications and additions as required by the three existing methods. Hence, the heterodyning PRB may have the potential for development of low-end ultrasound systems, in which the requirement for substantial reduction in cost, power is needed, and a small degradation in image quality would be tolerable [23]. In addition, more systematic image quality assessment, e.g., *in-vivo* data emulations, may be needed before its clinical use.

In fact, the phase tolerances for both the interpolation and phase rotation beamformer are consistent with each other. For instance, an interpolation beamformer with $f_{eff} = 32 \cdot f_0$ can yield a phase coherence within $360^\circ/32/2 = 5.625^\circ$. A baseband PRB employing 4-stage CORDIC rotators can achieve a close phase coherence within 7.1° , as presented in Table 3.1. In principle, a baseband PRB can

3.3. Conclusion

achieve a better phase coherence by performing the accurate angle phase rotation, however, it is unable to align the envelope $A_n(t)$ and the instantaneous angle $\phi_n(t)$ as well as an interpolation beamformer due primarily to a poorer delay resolution. Fortunately, past experience and extensive simulation results indicate that they can ultimately yield comparable beamforming performances.

In conclusion, benefited from its compact structure and dramatically reduced computational complexity, the digital heterodyning PRB is particularly competitive in development of a low cost front-end system and therefore presents the potential to be employed in the envisioned HUS, provided that the obtained image quality is qualified for the home-based imaging applications.

Chapter 4

Oversampled $\Delta\Sigma$ beamforming

This chapter reviews the principle of oversampling A/D conversion followed by discussion on alternative configurations of the $\Delta\Sigma$ beamformer. Further analysis points out the image degradation problem related to dynamic focusing in a post-reconstruction $\Delta\Sigma$ beamformer. The subsequent sections, namely 4.2 to 4.4, present four efficient approaches to suppress the unfriendly dynamic focusing artifacts. Both Field II software simulation and real ultrasound data emulation are carried out to illustrate and qualify their effectiveness. This chapter concludes with some practical concerns for the use of $\Delta\Sigma$ beamformer.

4.1 Overview

Recently, more efforts have been made to develop a cost effective digital beamforming system based on the oversampling $\Delta\Sigma$ A/D converters [35–40]. Unlike multi-bit Nyquist ADCs in a conventional system, the $\Delta\Sigma$ ADC usually employs a simple one-bit (single-bit) quantizer operating at very high speed to achieve the required signal to quantization noise ratio (SQNR). Owing to the merely two quantization levels, oversampling $\Delta\Sigma$ ADCs take the advantage of their ro-

4.1. Overview

bustness to circuit imperfections. The accompanying analog anti-aliasing filter in each Rx-channel can be considerably simplified benefited from the particularly high sampling rate. Apart from that, the oversampling $\Delta\Sigma$ ADC also provides sufficient delay resolution for high performance digital beamforming so that the complicated interpolator or phase rotator in a conventional beamformer can be obviated. The proposed $\Delta\Sigma$ beamformer thus presents a potential to dramatically reduce the size and complexity of the frond-end circuitry. However, the resulting image produced by the $\Delta\Sigma$ beamformer with an economic post-reconstruction strategy suffers from significant artifacts directly related to the dynamic receive focusing [7]. Miscellaneous techniques have been proposed to suppress the associated error, thus producing qualified images based on the single-bit digital sample alignment.

4.1.1 $\Delta\Sigma$ modulation

A/D converters transform a continuous analog signals into digital series, which are discrete both in time and amplitude, by sampling and quantization. Assuming the associated quantization noise being white, a multi-bit ADC can achieve a maximum SQNR given by [41]:

$$SQNR_{max} = 6.02 \cdot N_b + 1.76 + 10 \cdot \log(OSR), \quad (4.1)$$

where N_b is the number of quantization bits and OSR is the oversampling ratio, defined as the ratio of the sampling rate to the Nyquist rate f_N of input signal. In general, Nyquist ADCs achieve an SQNR gain by increasing N_b in equation 4.1. Unfortunately, component matching requirements double with every bit increase in resolution, which applies to flash, successive approximation or pipelined

4.1. Overview

ADCs. Therefore, the increased resolution, e.g., $N_b > 12$ would potentially lead to a demanding requirement on component matching. On the contrary, oversampling ADCs usually employ less number of bits but sample at a frequency much faster than f_N , namely a large OSR, to fulfill the required SQNR. Single-bit quantizer in practice has been widely used due to its inherent linearity. Equation 4.1 implies that straight oversampling offers an SQNR improvement of 3 dB for every doubling of the sampling rate. A single-bit oversampling ADC thus needs to sample $2^{14} = 16384$ times faster than a 8-bit ADC operating at f_N to achieve a roughly equivalent SQNR of 48 dB. Consequently, for echo bandwidth ranging from 3 to 10 MHz in a typical ultrasound machine, straight oversampling would require a highly impractical sampling rate with the state-of-the-art VLSI technology.

$\Delta\Sigma$ modulation, which shapes quantization noise through the use of feedback, is the key to success of oversampling ADCs. Figure 4.1(a) illustrates the block diagram of the second-order $\Delta\Sigma$ modulator selected for the recently proposed ultrasound beamformer [7]. The discrete time integrator has an infinite DC gain, which enables the average value of modulator output $d(n)$ tracks the average value of input $x(n)$. Assuming again that the quantizer introduces white noise source $e(n)$, which is independent of $x(n)$ as depicted in Figure 4.1(b), the linear model second-order $\Delta\Sigma$ modulator can be characterized by the Z-domain system function as [41]:

$$S_{TF}(z) = \frac{D(z)}{X(z)} = z^{-1} \quad (4.2a)$$

$$N_{TF}(z) = \frac{D(z)}{E(z)} = (1 - z^{-1})^2 \quad (4.2b)$$

It is apparent that the signal transfer function $S_{TF}(z)$ is simply a unit time delay, whereas the noise transfer function $N_{TF}(z)$ describes a discrete time high pass

4.1. Overview

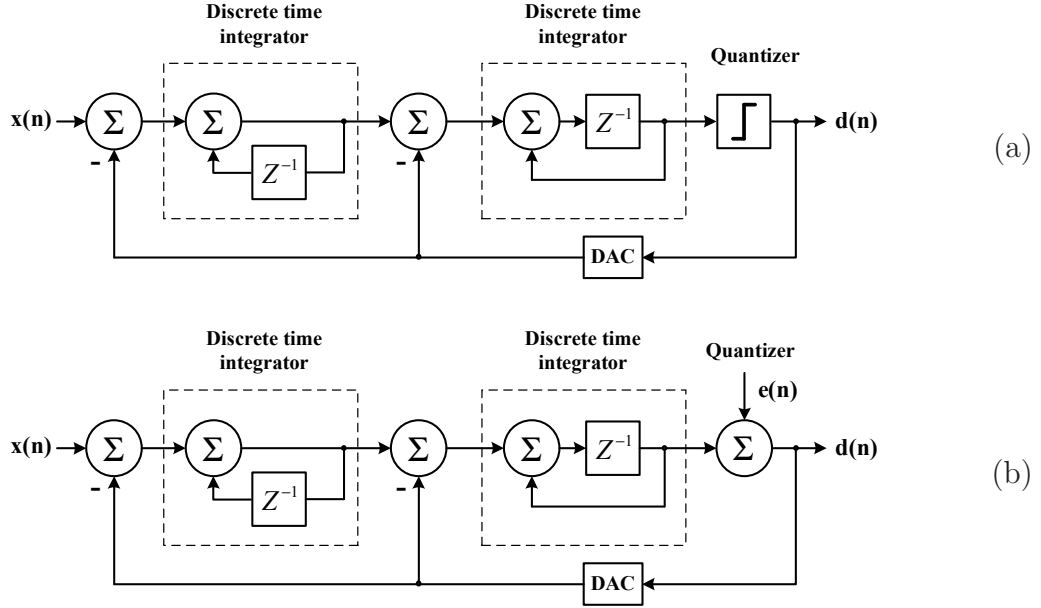


Figure 4.1: Diagram of a second-order $\Delta\Sigma$ modulator (a) and its linear model (b)

filter. Supposing that the sampling rate keeps increasing, band edge of the input signal would approach the discrete time zero frequency, where $N_{TF}(z)$ has its null. Namely, the input signal band is shifted into stop-band of the high pass filter $N_{TF}(z)$, in which the quantization noise is substantially suppressed, by an increased OSR. Therefore, the $\Delta\Sigma$ modulator can provide extra SQNR improvement within the band of input signal by pushing much of the quantization noise into higher frequency band. Figure 4.2 illustrates this noise shaping effect. After removal of the out-of-band noise by subsequent low pass filtering, a single-bit second-order $\Delta\Sigma$ modulator can achieve an optimum SQNR given by [41]:

$$SQNR_{max} = 1.76 - 12.9 + 50 \cdot \log(OSR), \quad (4.3)$$

which implies that doubling the OSR in $\Delta\Sigma$ modulation can provide a promising SQNR gain of 15 dB in comparison to 3 dB/octave without noise shaping.

4.1. Overview

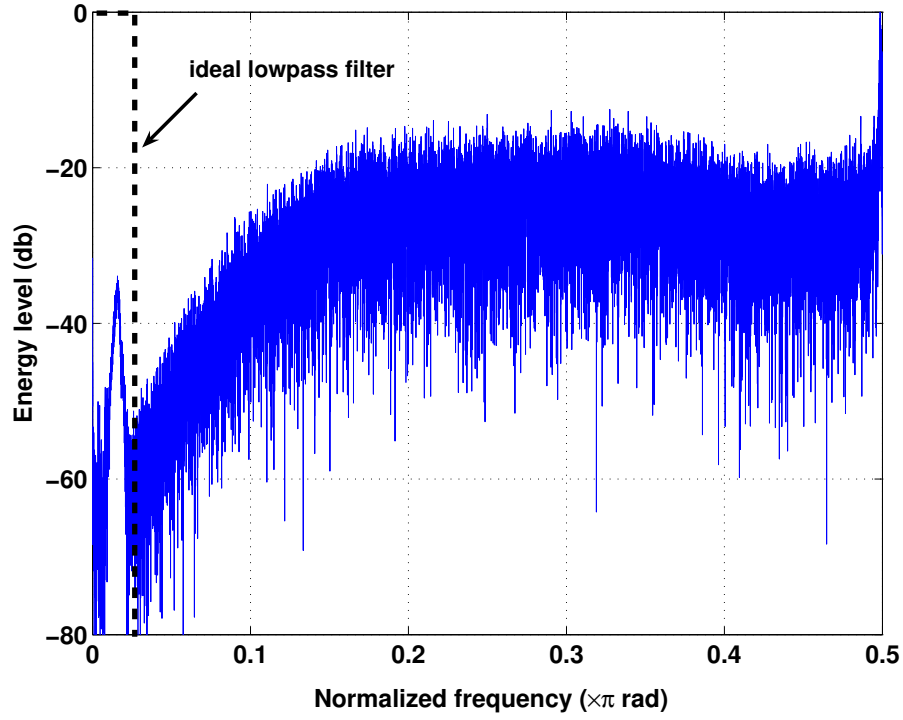


Figure 4.2: Noise shaping effect in $\Delta\Sigma$ modulation

Nowadays, commercial systems commonly employ 8 to 10-bit Nyquist ADCs to fulfill a favorable system dynamic range [42]. Based on equation 4.1 and 4.3, the $\Delta\Sigma$ ADC with $OSR = 20$ can achieve a comparable SQNR of 53.9 dB. For an ultrasonic transducer with 100 % fractional bandwidth, the prescribed sampling rate would be around $60 \cdot f_0$, which is consistent with the conclusive sampling rate of $64 \cdot f_0$ in [43].

4.1.2 Beamformer architecture

The $\Delta\Sigma$ beamformer proposed by Freeman *et al.* employs an economic post-reconstruction strategy as illustrated in Figure 4.3. In particular, the required time delay is fulfilled by applying appropriate sample (tap) selection directly on the modulator output, *i.e.* the single-bit sample stream in each Rx-channel. Multi-

4.1. Overview

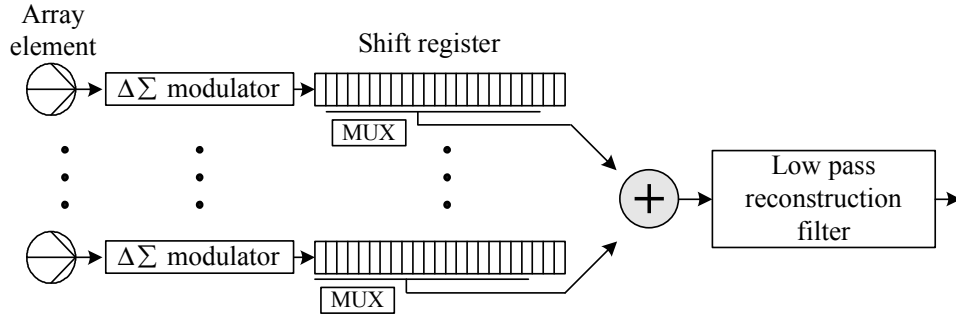


Figure 4.3: Diagram of a post-reconstruction $\Delta\Sigma$ beamformer

bit signal reconstruction (removal of modulated quantization noise) is performed simply after beamforming summation across the array [7]. Consequently, only one low pass FIR filter is needed in the system, and the channel summation adder can be efficiently implemented by a parallel counter consisting of a few full-adders. Nonetheless, it is worth noticing that the quantization noise is still present in the output after channel summation. The post-reconstruction $\Delta\Sigma$ beamformer thereby requires an unfavorable beamforming frequency, which is as high as the modulator sampling rate (*i.e.* $f_{BF} = f_s$).

In principle, the multi-bit reconstruction should be performed prior to beamforming summation as required in the pre-reconstruction strategy. And a reduced beamforming frequency at the Nyquist rate (*i.e.* $f_{BF} = f_N$) is allowed in a pre-reconstruction $\Delta\Sigma$ beamformer. Unfortunately, the use of a costly long tap FIR filter per channel, as shown in Figure 4.4, would considerably increase the system cost and overshadow the advantages of $\Delta\Sigma$ beamformer. A more wise implementation simplifies the FIR filter in each Rx-channel to a few accumulators based on polyphase decomposition, however, it inevitably increases the complexity of delay control logic and requires a much more complicated multi-bit adder for beamforming summation [40, 44].

Obviously, the post-reconstruction $\Delta\Sigma$ beamformer in practice can be more

4.1. Overview

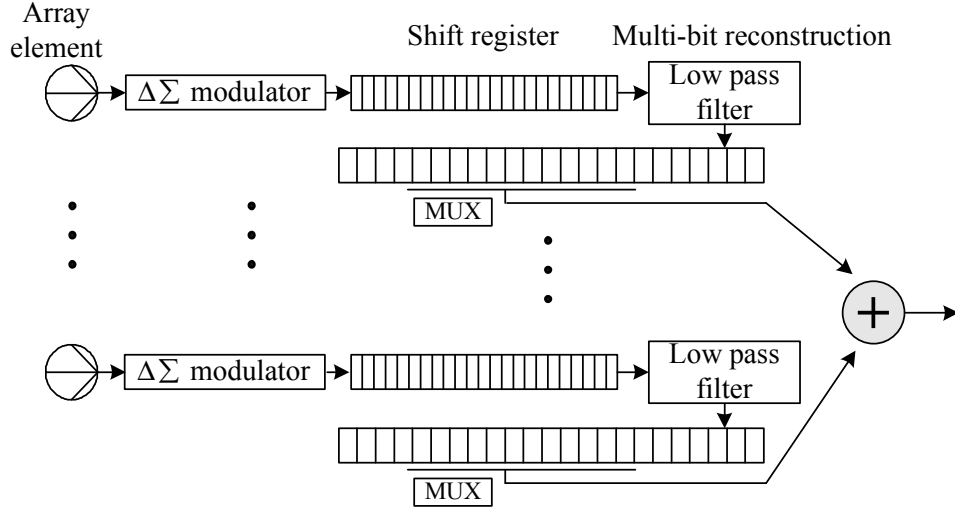


Figure 4.4: Diagram of a pre-reconstruction $\Delta\Sigma$ beamformer

competitive attributed to its compact and economic implementation structure.

4.1.3 Dynamic focusing artifacts

In principle, swapping the sequential order of signal alignment (beamforming) and low pass filtering would produce identical results, known as the commutative property, in a linear time-invariant (LTI) system [45]. However, the commonly used dynamic receive focusing technique in modern digital ultrasound systems is a time-variant operation, which undesirably undermines the basis of this rearrangement.

As described in Section 2.3, the channel sample stream is delayed by time increments equal to multiples of the sampling period T_s . Assuming again that the time starts when firing of the last element for transmission is completed and a large enough memory is used to sequentially accommodate the modulator sampling outputs in an arbitrary Rx-channel, the tap number (address in the memory) of a particular sample would directly correspond to the absolute time delay applied on it. Similar with that in the heterodyning PRB, one sample is said to be

4.1. Overview

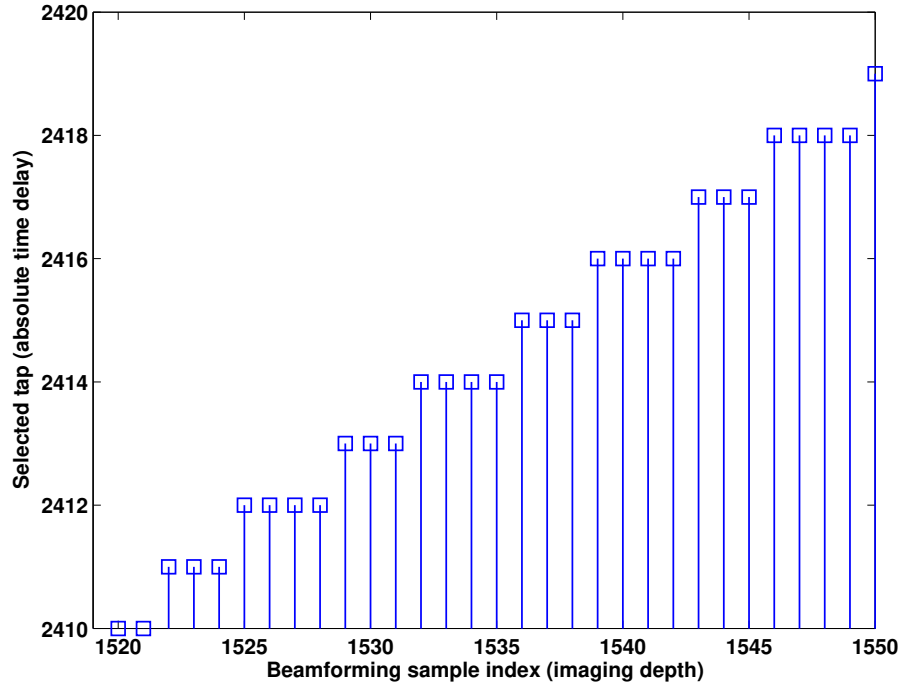


Figure 4.5: Sample selection in a digital beamformer with real time dynamic focusing

repeated if the quantized absolute delay remains unchanged as the imaging depth increases, *e.g.*, the 2414th tap in Figure 4.5 undergoes 3 repetitions. Past experience and extensive simulation results have demonstrated that the rearrangement of channel summation and low-pass filtering with repeated samples is feasible in a multi-bit dynamic focused beamformer, *i.e.* execution of interpolation filtering or demodulation filtering after channel summation [7, 30].

However, significant artifacts have been detected in the resulting image by applying the same repeat technique in a post-reconstruction $\Delta\Sigma$ beamformer. The time-variant operation, *i.e.* repeating samples in the delay line, disrupts the synchronization between modulator and reconstruction filter. More specifically, the filter injects unpredictable noise into the beamformed signal resulted from its false interpretation of repeated samples as extra difference from the modulator. The associated artifacts related to dynamic focusing apparently lead to a reduced con-

4.1. Overview

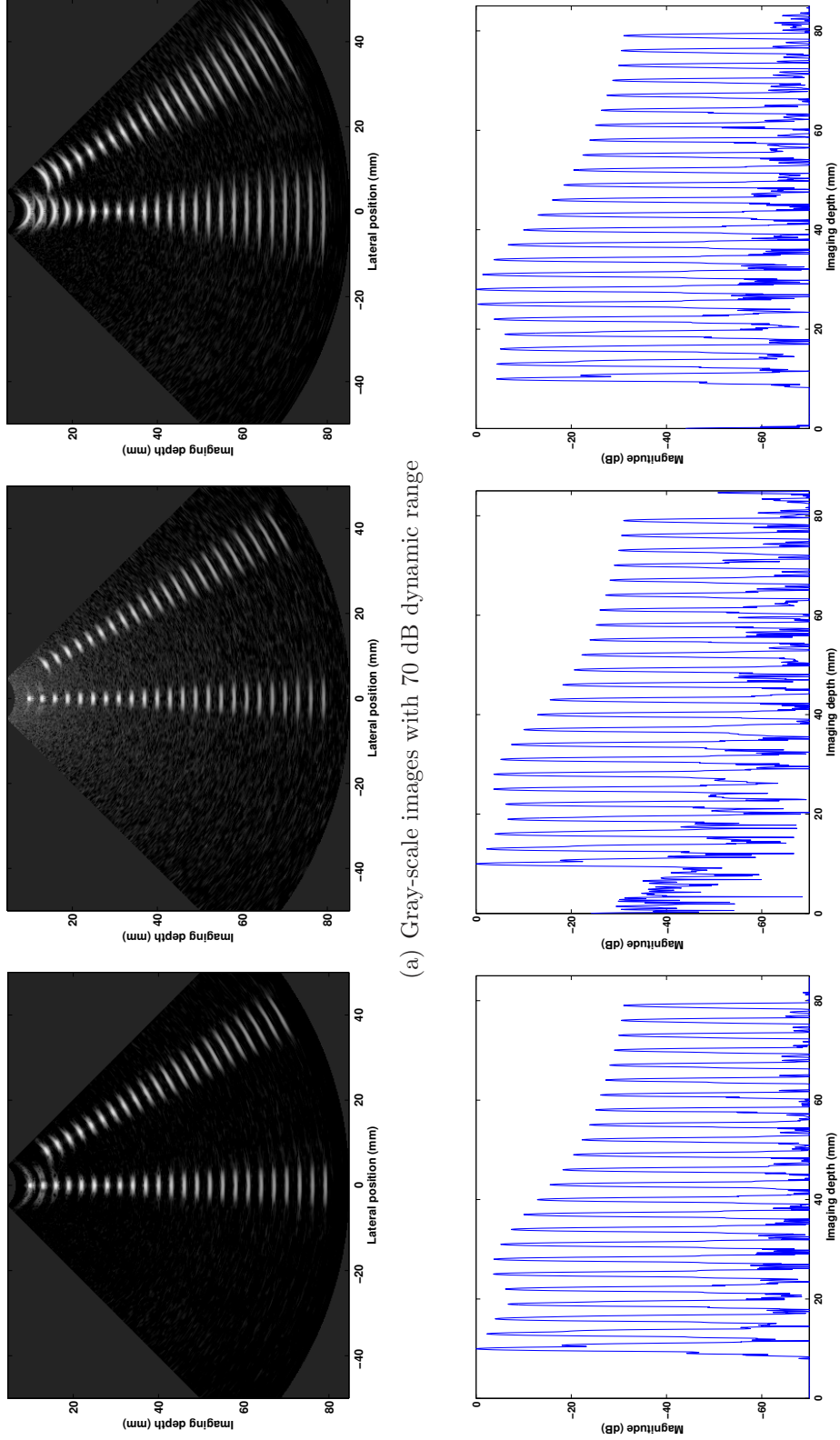
trast performance as reflected in Figure 4.6. It is also verified that applying receive static focusing (with LTI operations involved only) in a post-reconstruction $\Delta\Sigma$ beamformer is free of such artifacts, but it would lead to a significantly degraded lateral resolution.

Various approaches have been proposed to restore the image quality in the dynamic delayed post-reconstruction $\Delta\Sigma$ beamformer. Instead of repeating the previous sample, Freeman *et al.* proposed an insert-zero technique which attempts to keep the average signal power unaltered by inserting effective zeroes in the delay line [7,46]. Figure 4.7 illustrates the designated manipulation scheme of the sample stream in the insert-zero technique. The corresponding effectiveness is showed in Figure 4.8. Nevertheless, the digital samples stored in memory must be recoded to allow for a new signal level of zero. Table 4.1 presents the modified coding theme in the insert-zero technique. There are other efficient techniques capable of suppressing the dynamic focusing artifacts [30,36,37], each of which constitutes a low cost front-end solution by employing the post-reconstruction strategy.

Table 4.1: New coding theme in the insert-zero technique

stored samples	digital value	new coding theme
1	+1	10
0	-1	00
new level	0	01

4.1. Overview



(b) Central A-line plot

Figure 4.6: Field II simulation results produced by a $\Delta\Sigma$ beamformer employing dynamic focusing with pre-reconstruction (a) and post-reconstruction strategy (b), and employing static receive focusing with post-reconstruction strategy (c)

4.2. Compensated $\Delta\Sigma$ modulator with zero feedback

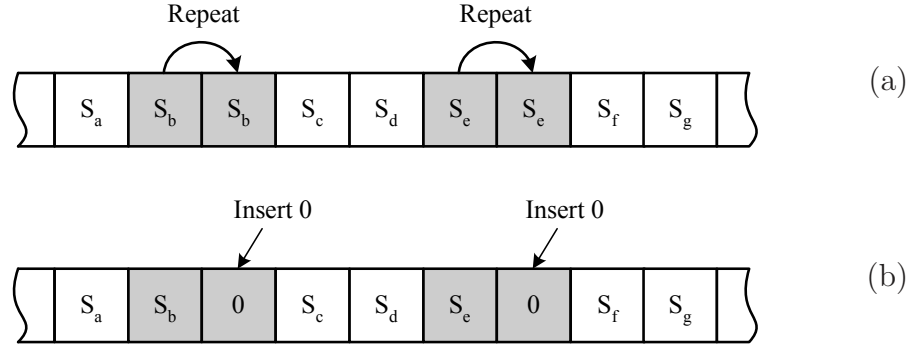


Figure 4.7: Stretch the sample stream by repeating the previous sample (a), and inserting an effective zero sample (b)

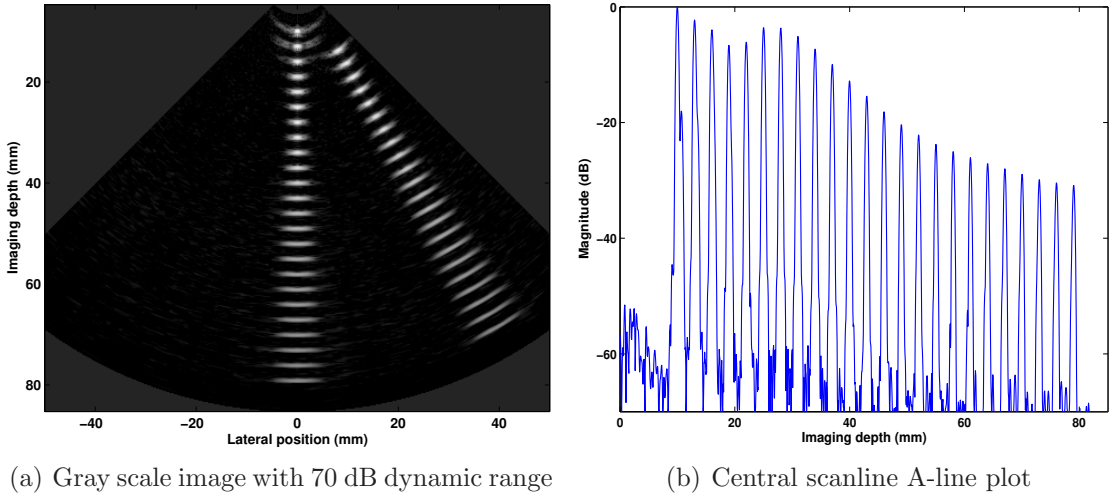


Figure 4.8: Field II simulation results produced by a $\Delta\Sigma$ beamformer with the insert-zero technique

4.2 Compensated $\Delta\Sigma$ modulator with zero feedback

Besides the insert-zero technique, Freeman *et al.* also developed a 2-X buffer modulator, in which a multiplexer, controlled by the delay logic of the beamformer, was used to choose between a normal or scaled-by-two magnitude to compensate for the repeated samples. Namely, normal (non-repeated) samples would have unity feedback, whereas samples later repeated in the delay structure would have

4.2. Compensated $\Delta\Sigma$ modulator with zero feedback

a feedback magnitude of two since each sample is encountered twice by the reconstruction filter [7]. To realize this compensation, a customized $\Delta\Sigma$ modulator with an additional multiplexer and an analog amplifier (or alternatively an extra DAC) is required, as depicted in Figure 4.9. Unfortunately, the accuracy of scaling an analog signal by two in practice is dependent on the fabrication process. Despite an improved image quality achievable by the 2-X buffer technique as compared to that of the uncompensated version, an increased noise floor has been detected when precise analog scaling cannot be achieved due to process variation [7].

4.2.1 Inverse insertion and zero feedback

As presented in [7], there are three ways of stretching the sample stream, *i.e.* repeating a sample, inserting an effective zero sample or splitting it into two equal parts (employed in the divided-by-2 technique). In fact, it is also possible to fulfill the sample stream stretching by inserting a sample, *e.g.* $-S_b$ or $-S_e$ in Figure 4.10(b), which is the inverse of the previous sample. Subsequently, a zero feedback level is required to take account of the inserted sample with the opposite sign. This procedure essentially ensures that the integrator in the compensated $\Delta\Sigma$ modu-

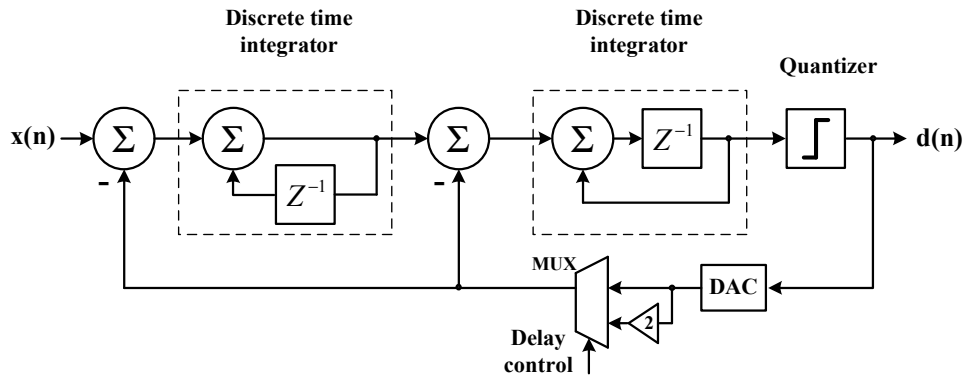


Figure 4.9: Schematics of the compensated $\Delta\Sigma$ modulator with 2-X buffer

4.2. Compensated $\Delta\Sigma$ modulator with zero feedback

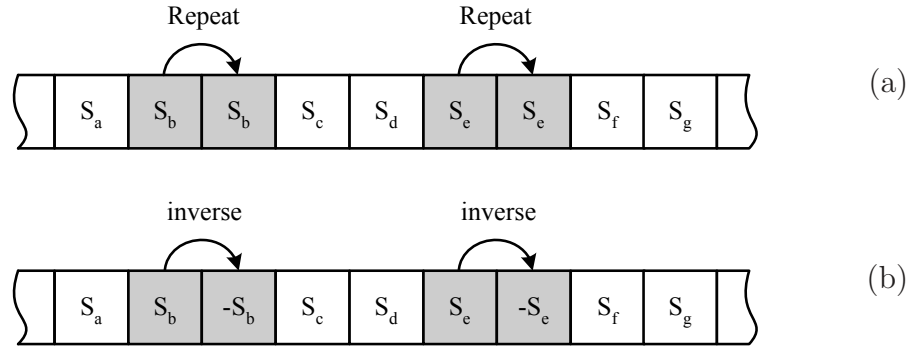


Figure 4.10: Stretch the sample stream by repeating (a) and inserting the inverse (b) of the previous sample

lator presents a faithful interpretation of the subsequently stretched modulator output sequence, which is to be reconstructed by the low-pass filter (or demodulator). Consider a similar controller is used here, as sketched in Figure 4.11, to choose the feedback level between a normal and zero magnitude. A sample of which the subsequent sample has the same quantized delay (*i.e.* conventionally repeated sample S_b or S_e in Figure 4.10(b)) would have zero feedback magnitude, whereas the normal (conventionally non-repeated) samples would have unity feedback.

The extra cost of generating the inverse sample for sample stream stretching could be minimal since only a one-bit digital inverter is required in individual channel. Moreover, scaling of the analog signal for feedback control is no longer required as the ground signal is readily available. As a result, the process/wafer dependent operation can be eliminated from the feedback path and would make compromise to the system robustness to circuit imperfection.

In fact, both designs imply that the quantized absolute time delay is allowed to remain unchanged, *i.e.* an arbitrary sample undergoes the repetition, by a maximum of one time only. Computation based on equation 2.3 indicates that the approximated delay by separation of the steering and focusing delay can meet

4.2. Compensated $\Delta\Sigma$ modulator with zero feedback

this requirement. Hence, these two approaches in principle are valid only in the relatively far field where f -number is larger than two.

4.2.2 Image quality evaluation

Field II software simulation was carried out for performance evaluation [32]. A 64-element phased array with $f_0 = 3.5$ MHz was used to sample the echo at $f_s = 64 \times f_0 = 224$ MHz with floating point accuracy. The simulated RF raw data were then converted to the $\Delta\Sigma$ modulator output sequences. Figure 4.12 and 4.13 indicate that beamformers employing the 2-X buffer and zero feedback modulators can both yield a satisfactory noise level, which is considerably lower than that produced by the uncompensated modulator. The noise in the range very close to the transducer surface is due primarily to the violation of the large f -number assumption in equation 2.3.

For the $\Delta\Sigma$ beamforming emulation, the Acuson data set was digitally interpolated by a factor of 16, thus obtaining an effective sampling rate of $f_{eff} = 13.89 \times 16 = 222.2$ MHz. Figure 4.14 indicates that both compensated modulators can achieve a close beamforming performance in terms of lateral resolution, and

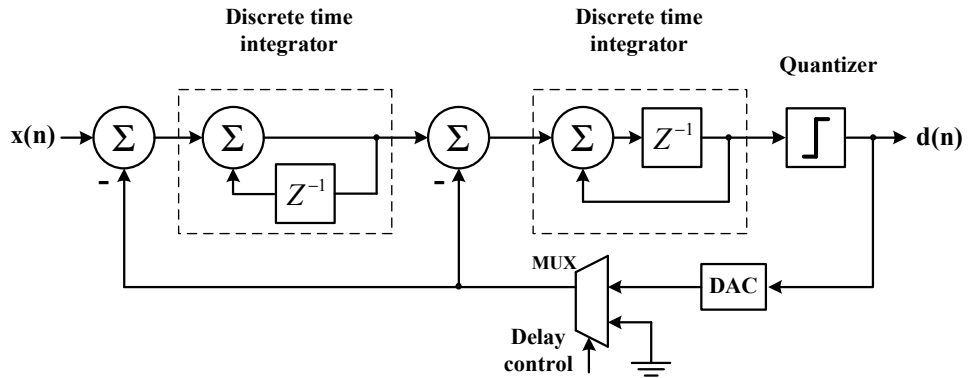


Figure 4.11: Schematics of the compensated $\Delta\Sigma$ modulator with zero feedback

4.2. Compensated $\Delta\Sigma$ modulator with zero feedback

noise level in comparison to those of the pre-reconstruction $\Delta\Sigma$ beamformer.

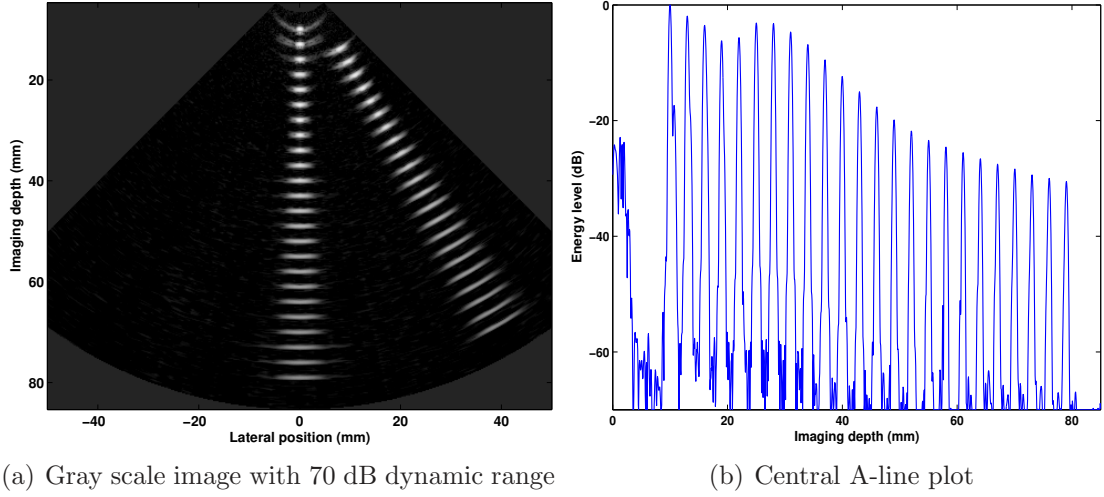


Figure 4.12: Field II simulation results by $\Delta\Sigma$ beamforming with the 2-X buffer $\Delta\Sigma$ modulator

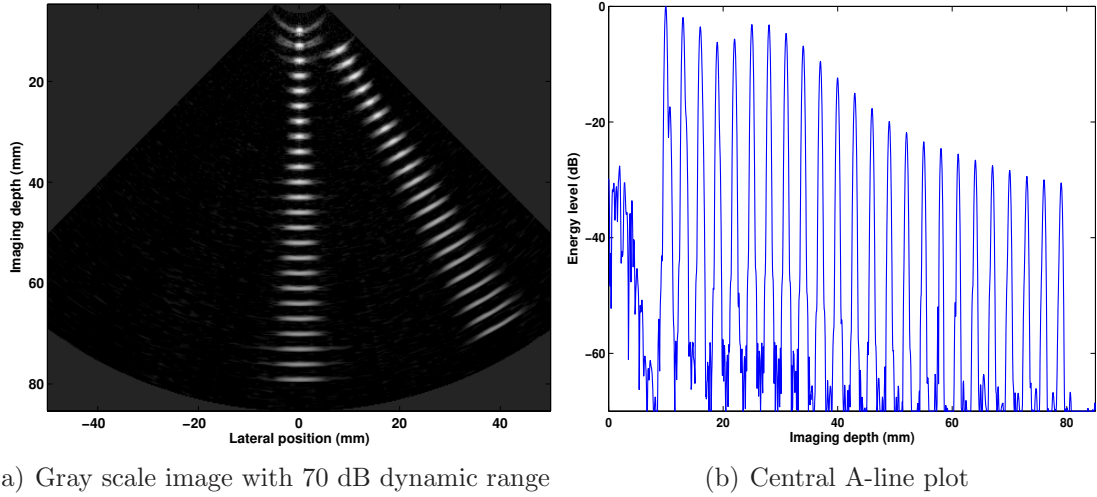


Figure 4.13: Field II simulation results by $\Delta\Sigma$ beamforming with the zero feedback $\Delta\Sigma$ modulator

4.2.3 Return-to-zero DAC implementation

In practical design of a high speed modulator, continuous-time implementation (CT modulator) is generally more attractive as compared to its discrete-time (DT)

4.2. Compensated $\Delta\Sigma$ modulator with zero feedback

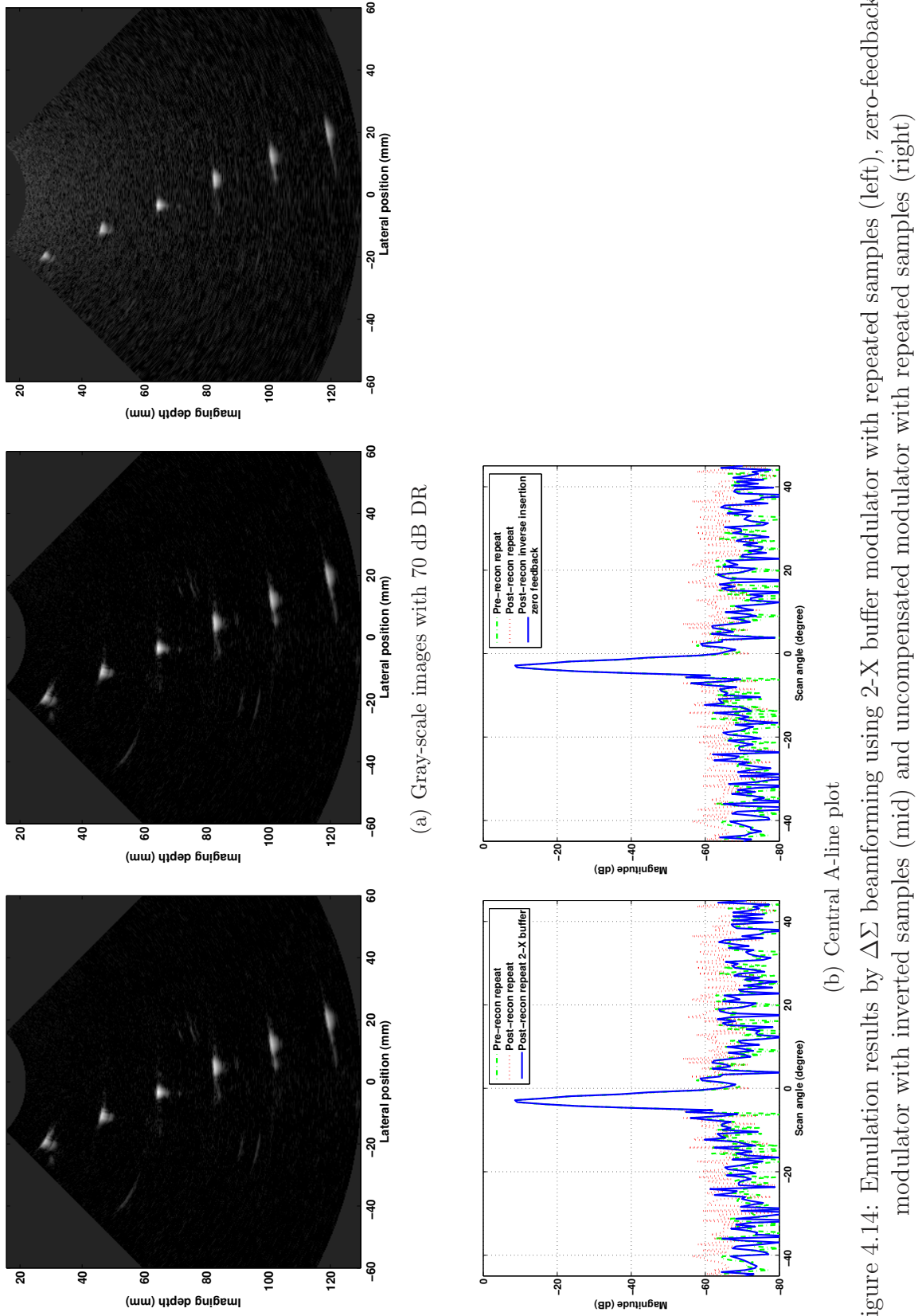


Figure 4.14: Emulation results by $\Delta\Sigma$ beamforming using 2-X buffer modulator with repeated samples (left), zero-feedback modulator with inverted samples (mid) and uncompensated modulator with repeated samples (right)

4.2. Compensated $\Delta\Sigma$ modulator with zero feedback

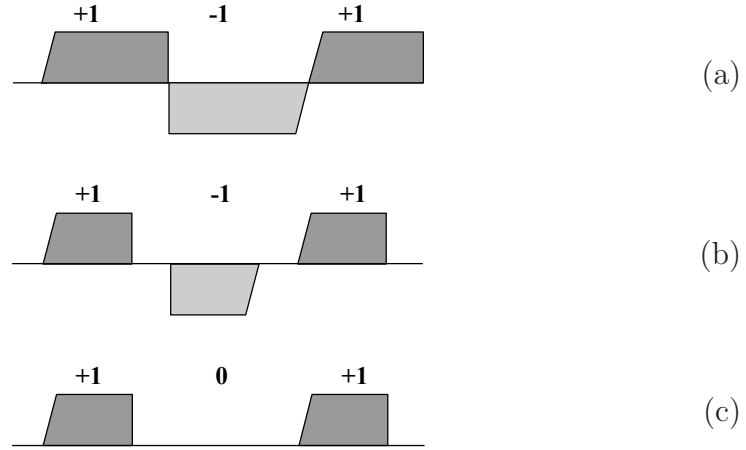


Figure 4.15: Generated pulses by a NRZ DAC (a), a RZ DAC (b) and a controlled RZ DAC (c)

counterpart, whose clock rate is limited by the op-amp settling requirements [47]. However, CT $\Delta\Sigma$ modulators in practice are sensitive to the shape of DAC pulses. The corresponding modulation performance thereby is contaminated by the fact that DAC pulses have unequal rise and fall time [48]. In order to resolve this asymmetry pulse problem, the return-to-zero (RZ) DACs have been widely used in the design of high speed CT $\Delta\Sigma$ modulators. By resetting feedback level to zero after a prescribed duration, as depicted in Figure 4.15(b), the RZ DAC ensures pulse error-free modulation [49]. The required zero feedback level thus can be conveniently obtained by disabling the DAC trigger clock at specified instants in a system employing RZ DACs, as depicted in Figure 4.15(c). In a preferred embodiment, added simplicity can be achieved by shifting the controller to enable/disable the DAC operation, as shown in Figure 4.16, so that the the digital multiplexer can be obviated.

4.3. Beamforming with asynchronous delay update

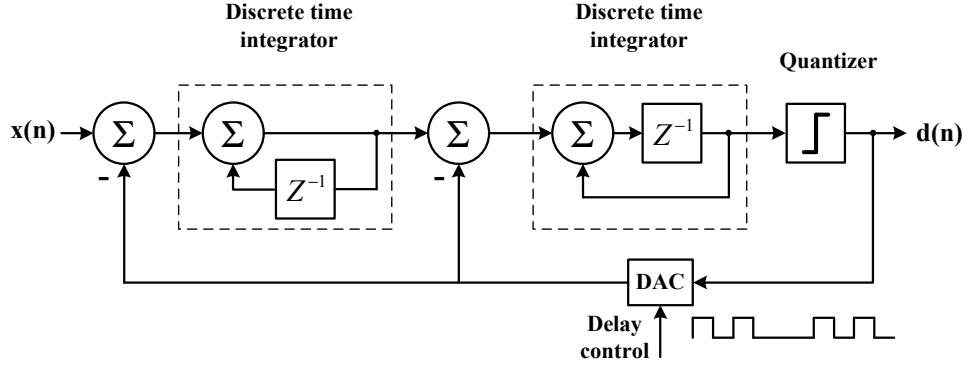


Figure 4.16: Schematic implementation of the zero feedback by a RZ DAC

4.3 Beamforming with asynchronous delay update

Figure 4.8 shows that the dynamic focusing artifacts can be satisfactorily suppressed by the insert-zero technique with conventional (uncompensated) $\Delta\Sigma$ modulators. However, bit growth due to the new discrete level inevitably increases the adder complexity and memory size. The symmetrical-hold technique was thereby proposed to achieve a single-bit solution by inserting ± 1 in a pair of Rx-channels simultaneously. In particular, cancellation of inserted values of opposite sign is fulfilled in the channel summation stage, which ensures that the ultimate image is identical to the image obtained by applying the insert-zero technique. Synchronization of the insertion in a pair of Rx-channels is maintained by making further manipulation on equation 2.3, *i.e.* quantizing the steering and focusing delay respectively, for the delay calculation [30, 39]. By bundling two successive samples as a group, another empirical technique inserts consecutive ± 1 in a particular Rx-channel to stretch the sample stream. However, it inevitably leads to a reduced delay resolution, which corresponds to half of the sampling rate. Thus, a single-bit solution with minimum compromise of the beamforming performance is desirable.

4.3. Beamforming with asynchronous delay update

4.3.1 The asynchronous delay update method

Existing digital beamforming systems capable of performing receive dynamic focusing usually update the time delay among all Rx-channels simultaneously. In order to realize the single-bit signal alignment with suppressed artifacts, the proposed asynchronous delay update method (ADUM) employs a novel delay update theme, which allows the relative delay in a particular Rx-channel to be updated only when no sample or even number of samples needs to be inserted. Assuming that at a time N_i samples need to be inserted into the sample stream, the proposed ADUM would have an identical sample selection behavior, *i.e.* applying the same delay, with the usual real time dynamic focusing method with repeated samples, provided that N_i is an even number; in case that only one sample ($N_i = 1$) needs to be inserted, *e.g.* the sample S_b in Figure 4.17, stretching of sample stream (delay update) is postponed until another sample insertion requirement, *i.e.* the sample S_e , occurs in the same Rx-channel. Consequently, two accumulative vacancies can be filled by a pair of consecutive ± 1 as illustrated in Figure 4.17(b); for N_i being an odd number larger than 1, the insertion process would always be fulfilled in two steps: insertion of $N_i - 1$ (an even number) samples followed by insertion of the remaining one sample. Thus, once upon completing $N_i - 1$ samples insertion with consecutive ± 1 , the same situation occurs as if only one sample needs to be inserted. Hence, insertion of the ± 1 pair can always be assured in the ADUM for an arbitrary value of N_i larger than zero.

Figure 4.18 shows the associated sample selection in the proposed ADUM. When the insertion process is postponed, *e.g.* the 1528th beamforming sample, the required delay is not updated as usual. Namely, instead of repeating the 2412nd sample once again as requested by the repeat technique, the ADUM selects the

4.3. Beamforming with asynchronous delay update

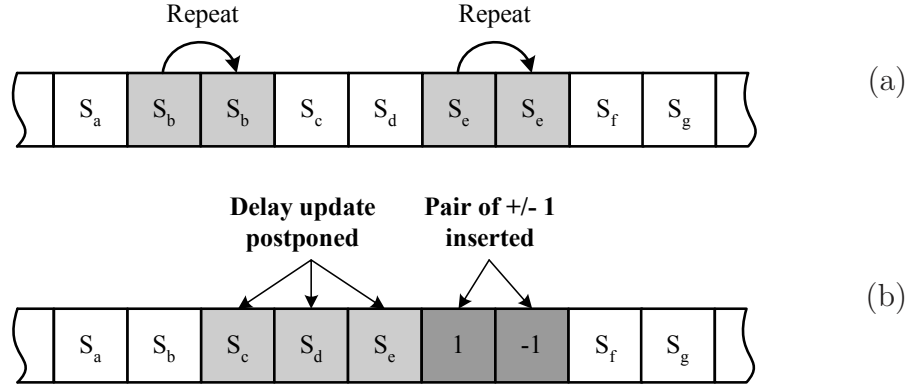


Figure 4.17: Stretch the sample stream in the repeat technique (a) and the ADUM (b)

subsequent sample, *i.e.* the 2413rd sample, to produce the stretched delay line. As a result, the 2412nd sample is nominally repeated twice so that a pair of ± 1 in practice will be inserted. Obviously, there is a maximum of only one tap error in the ADUM sample selection (delay update) in comparison to the normal real time dynamic focusing employing the repeat technique.

4.3.2 Image quality evaluation

Using the same sets of simulated and real ultrasound RF data, the resulting images produced by the proposed ADUM are shown in Figure 4.19 and 4.20. The images produced by the inserting ± 1 technique with half delay resolution method (HDRM) proposed in [37] as well as the symmetrical-hold technique proposed in [30] are plotted aside for comparison. Clearly, all these methods successfully suppress the dynamic focusing artifacts by achieving a close noise level with that in a pre-reconstruction $\Delta\Sigma$ beamformer. The symmetrical-hold technique yet suffers a degraded beamforming performance in the relatively near field due to violation of the large f -number assumption, as reflected in Figure 4.20(b). With a half delay resolution at $1/(32 \cdot f_c)$, the HDRM is still able to obtain a comparable beamforming

4.3. Beamforming with asynchronous delay update

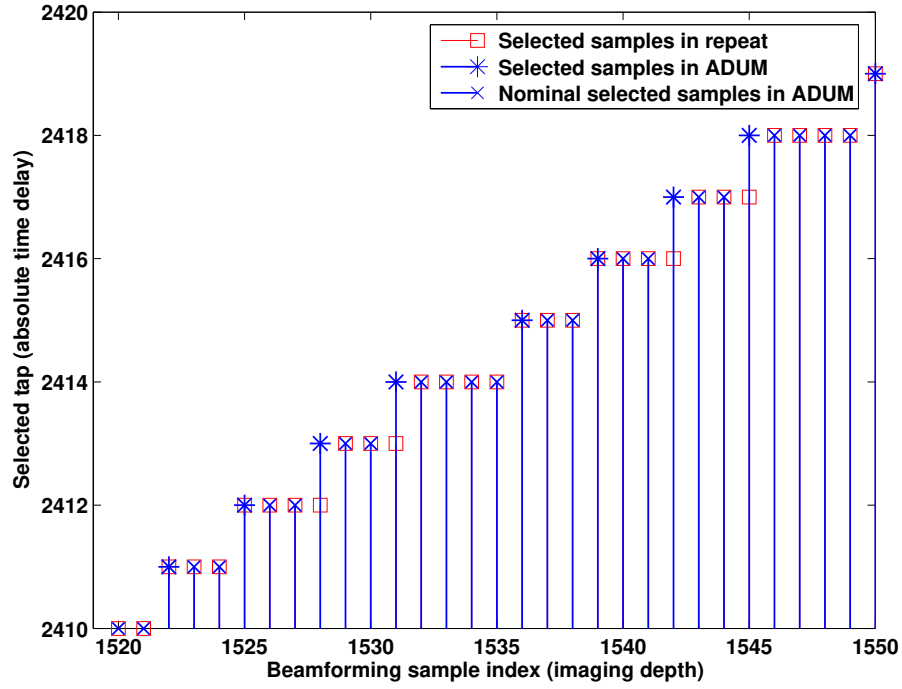


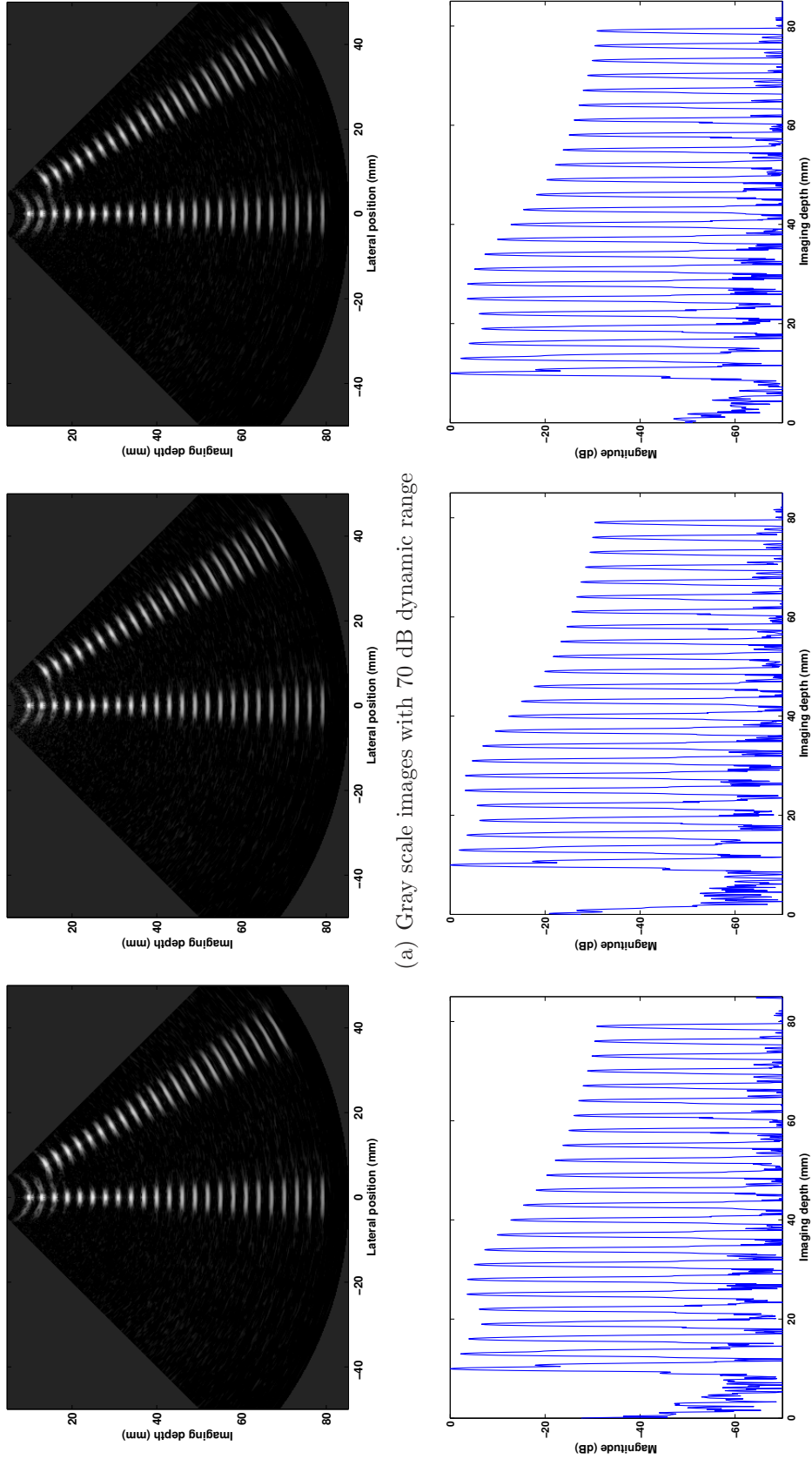
Figure 4.18: Sample selection in a particular channel for the ADUM and the repeat technique

performance with the pre-reconstruction $\Delta\Sigma$ beamformer. This grace performance acutally lies in the advantage that $1/(32 \cdot f_c)$ has already provided sufficient delay resolution for high performance ultrasound digital beamforming. By allowing for the echo broadband effects, further performance enhancement can be utopia even with an improved delay resolution at $1/(64 \cdot f_c)$. However, in a system employing third or higher order $\Delta\Sigma$ modulator with a reduced OSR, it is expected that the ADUM would attain a superior beamforming performance over the HDRM benefited from its higher delay resolution.

4.3.3 An implementation issue

Notice that in the delay (tap selection) calculation for ADUM, both the previous and subsequent samples need to be taken into consideration, thus resulting in

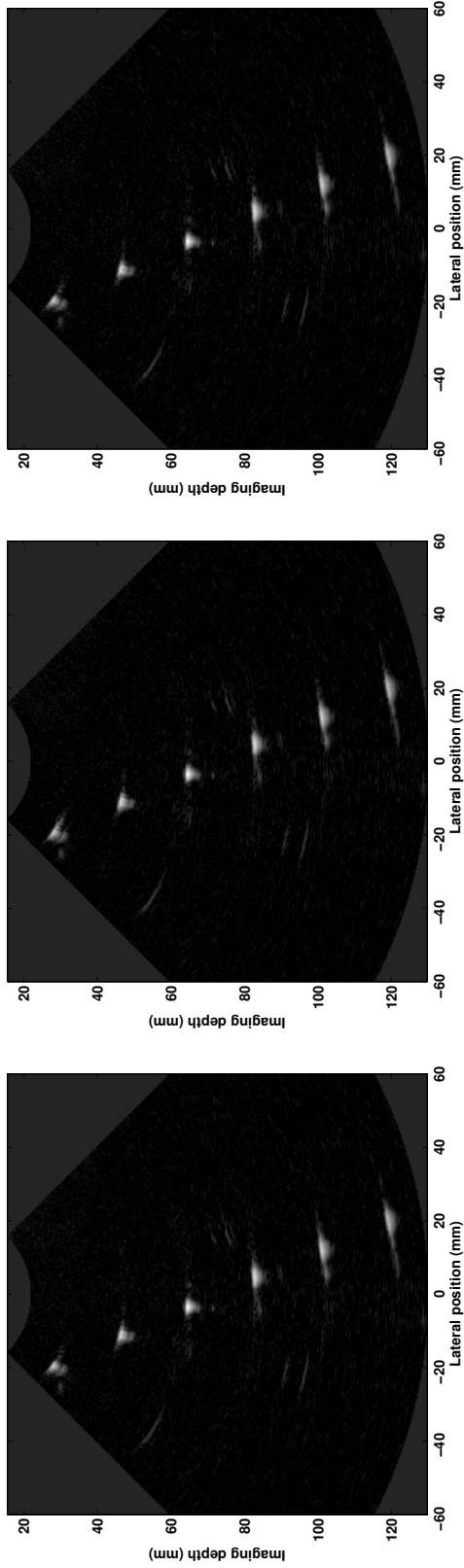
4.3. Beamforming with asynchronous delay update



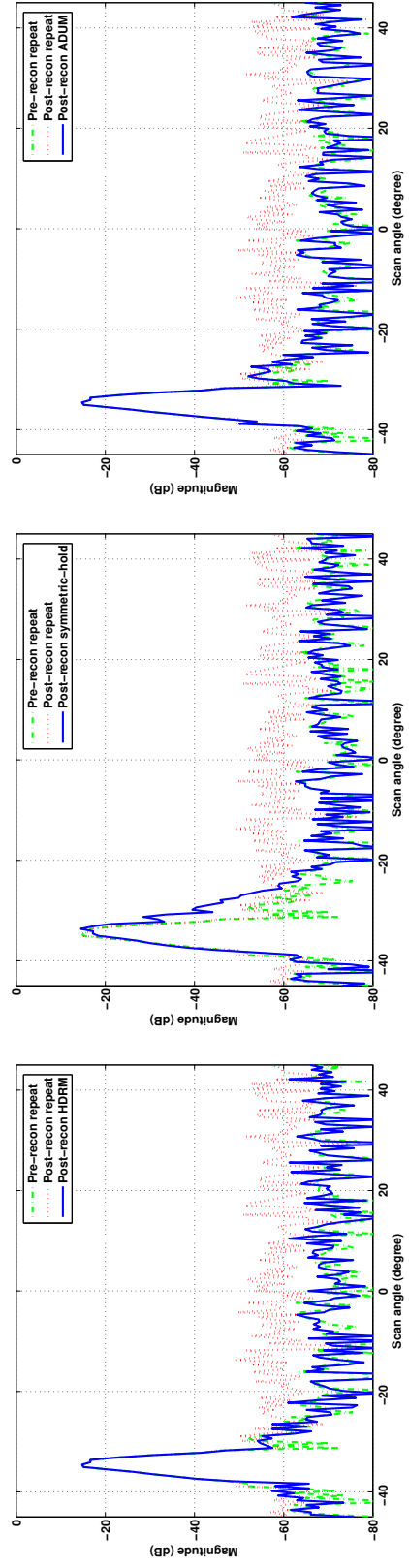
(b) A-line plots of the central scanline

Figure 4.19: Field II simulation results by $\Delta\Sigma$ beamforming employing the HDRM (left column), symmetrical-hold (mid column) and ADUM (right column).

4.3. Beamforming with asynchronous delay update

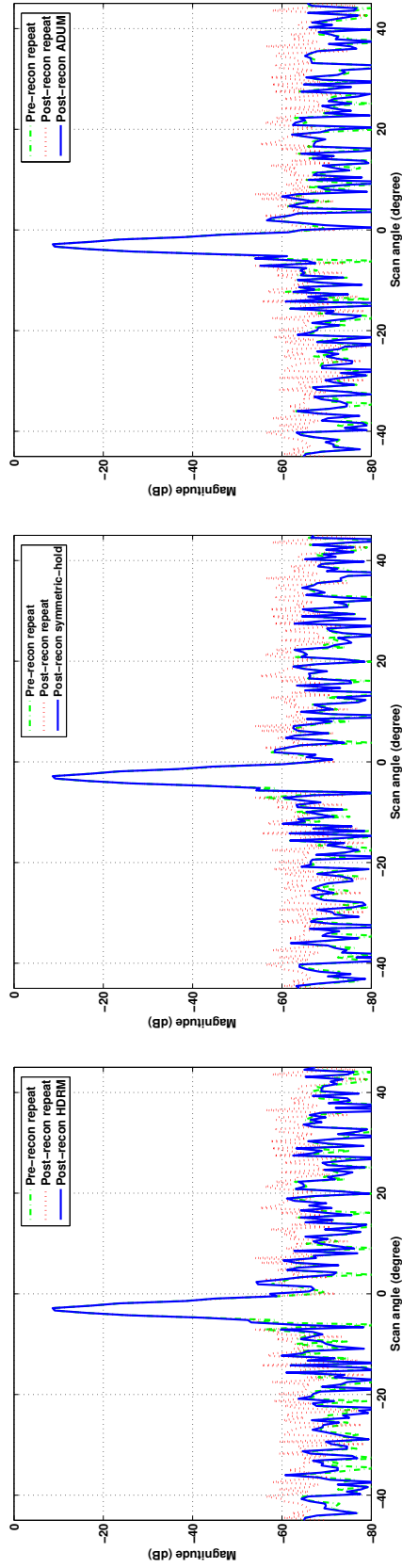


(a) Gray scale images with 70 dB dynamic range



(b) Cross-section views of the 1st wire target by applying various insert ± 1 techniques

4.3. Beamforming with asynchronous delay update



(c) Cross-section views of the 3rd wire target by applying various insert ± 1 techniques

Figure 4.20: Phantom study results by applying the HDRM (left column), symmetrical-hold technique (mid column) and ADUM (right column).

4.4. Modified zone-based dynamic focusing

an increased calculation complexity compared to the HDRM. However, by taking account of the extreme high working frequency in an oversampling $\Delta\Sigma$ beamformer system, the required time delay (tap selection number) is usually considered to be pre-calculated and stored in a LUT in the preferred embodiment. More specifically, the LUT is composed of a digital value (*e.g.*, '1') to represent the starting positions of the ± 1 values insertion and another digital value (*e.g.*, '0') to represent positions for the normal samples. Therefore, the ADUM delay calculation in practice will not increase the system cost and complexity.

4.4 Modified zone-based dynamic focusing

Real time dynamic focusing provides premium image quality since each imaging point is in faultless focus in the receive beamforming. However, the exorbitant working frequency in a post-reconstruction $\Delta\Sigma$ beamformer, which is identical with the modulator sampling rate, has tremendously increased the workload for delay calculation. Generally, a $\Delta\Sigma$ beamformer sampling at $64 \cdot f_0$ would have to afford 16 times more delay calculation load as compared to an interpolation beamformer working at $4 \cdot f_0$. For a transducer with $f_0 = 3.5$ MHz, the required time delay needs to be updated $N_{du} = 15 \times 64 \times 2 \times f_0 / c \approx 43,636$ times per channel for an imaging depth of 15 cm. Assuming a frame rate of 15, $N_{du} \times 15 = 654,580$ updates need to be accomplished for individual Rx-channel within one second. To apply real time dynamic focusing in $\Delta\Sigma$ beamforming thus incurs a demanding computation load, or alternatively requests a huge LUT. A rational way to bypass this obstacle with minimum compromise of image quality is to employ the zone-based dynamic focusing in $\Delta\Sigma$ beamforming.

4.4. Modified zone-based dynamic focusing

4.4.1 Boundary artifacts

Zone-based dynamic focusing makes a greatly reduced effort in delay calculation by updating the relative time delay on occasion when the ongoing beamforming sample enters into a new focal zone [50, 51]. Figure 4.21 illustrated this delay update theme. A set of relative delay, typically with reference to the central element, is computed based on a selected internal focal point (usually located at the zone central position). In the receive beamforming, this particular delay set is applied to all beamforming samples within the range of the corresponding zone. As a result, the relative time delay of the central element keeps unaltered zero, whereas its absolute time delay undergoes a linear increment as imaging points penetrating into deeper area inside a particular focal zone.

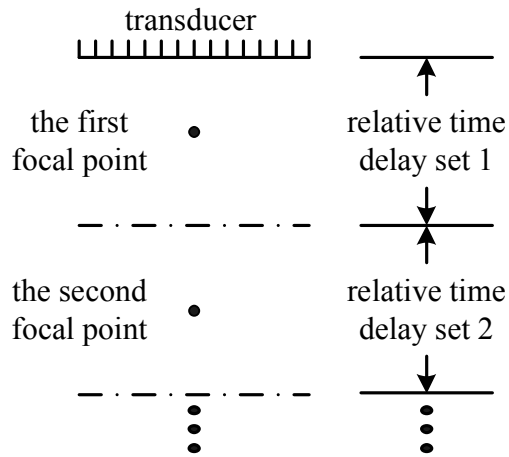


Figure 4.21: Delay update in zone-based dynamic focusing

Since the delay is updated only when the imaging point enters a new focal zone, the zone-based dynamic focusing technique employs a distinct scheme to stretch the sample stream. Figure 4.22 shows the associated sample selection theme at the boundary of two adjacent focal zones. The constant relative time delay applied inside a particular focal zone yields a uniformly ascending sample

4.4. Modified zone-based dynamic focusing

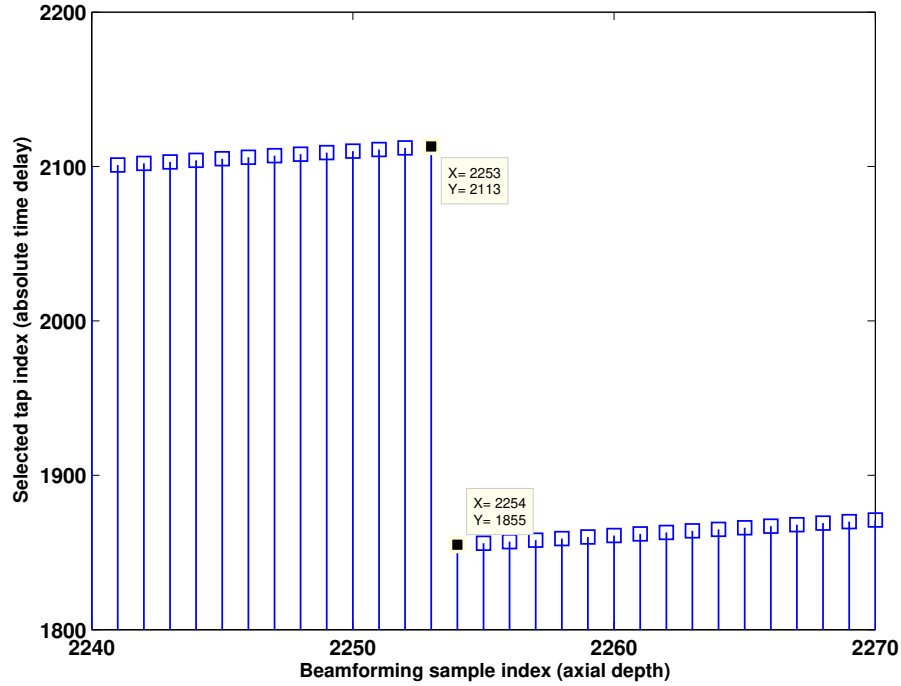


Figure 4.22: Sample selection in a particular Rx-channel in zone-based dynamic focusing with a zone depth of 5 mm

selection sequence, yet the delay reduction in the subsequent focal zone leads to a remarkable regress of the selected sample index. Thus, stretching of the sample stream is fulfilled by sequentially repeating quite a few samples in the previous zone, *e.g.* samples with indices ranging from the 1855 to 2113 in Figure 4.22.

By applying the insert-zero technique, consecutive zeroes thus are inserted into the delay line to replace the repeated samples. Simulation results indicate that the unfriendly artifacts persist, particularly in the near-field range, at the boundary of adjacent focal zones. Further investigation reveals that too many consecutive samples are artificially set to be zero in the delay line, thereby leading to an unfaithful interpretation of received echoes on the borders of two neighboring zones. And the artifacts are more critical in the near field where the number of inserted zeroes is relatively large, as illustrated in Figure 4.26.

4.4. Modified zone-based dynamic focusing

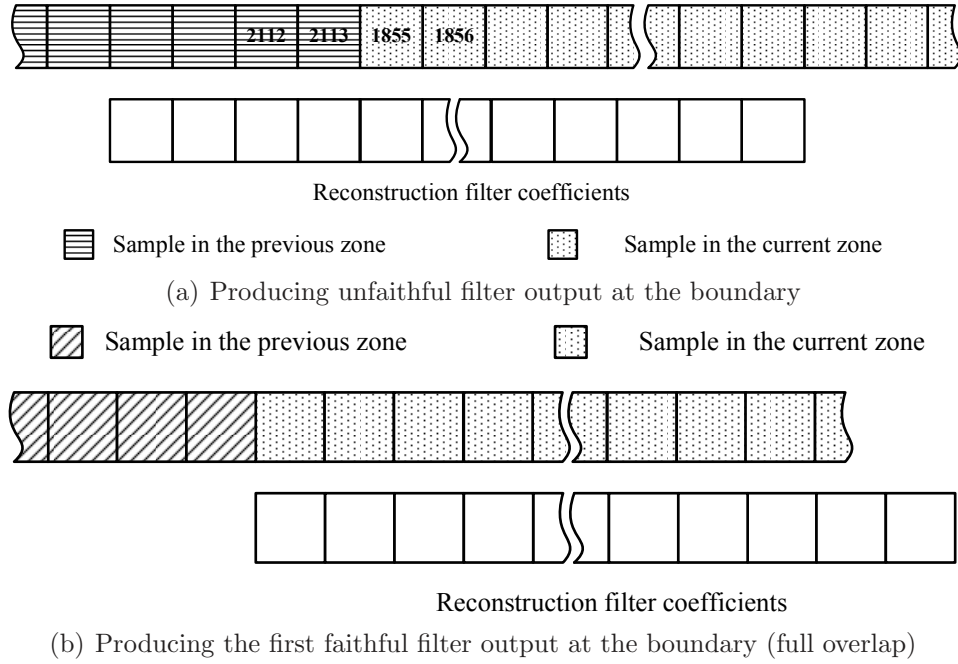


Figure 4.23: Direct sharing of reconstruction filter in the conventional zone-based dynamic focusing

It is worth noticing that the relative time delay keeps constant within an arbitrary focal zone and the sample stream stretching only needs to be executed at the zone boundaries. Namely, only linear time-invariant operation is performed inside each focal zone. Sharing of the reconstruction filter might as well produce error free results by employing the post-reconstruction strategy inside the range of a particular focal zone. However, sharing the filter in this direct manner would employ unfaithful filter output samples for final image formation. Figure 4.23 illustrates this misoperation on focal zone borderings. Apparently, the first reliable reconstructed sample to be used for final image formation in a particular zone can only be produced when there is full overlap of the filter coefficients and the delay line samples in the corresponding zone, as shown in Figure 4.23(b). And it has been found that the utilization of unfaithful samples for image formation is directly responsible for the boundary artifacts.

4.4. Modified zone-based dynamic focusing

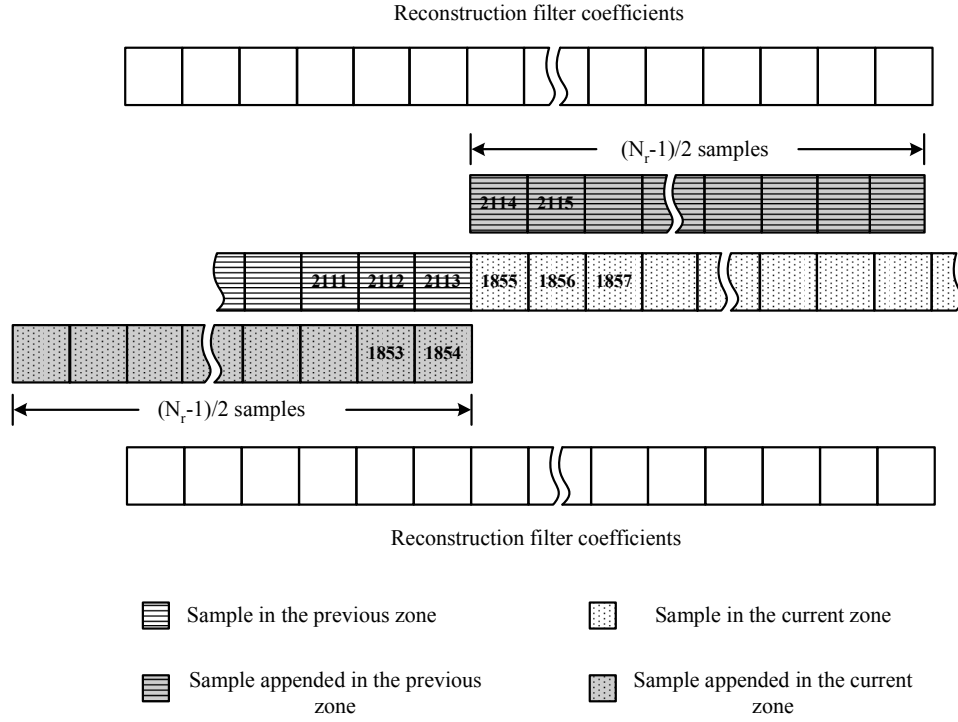


Figure 4.24: Appending samples in modified zone-based dynamic focusing

4.4.2 The solution

Since the number of faithful filter output samples is reduced by $N_r - 1$ for an arbitrary N_r -tap FIR filter due to its intrinsic group delay, the modified zone-based dynamic focusing method appends extra $N_r - 1$ samples to compensate such loss of an N_r -tap reconstruction filter. Assuming N_r being an odd number, $(N_r - 1)/2$ samples should be appended at both the entry and end of the segmental sample stream selected in a particular zone. In addition, the same relative delay inside the focal zone applies to the extra inserted samples, thus resulting in an extended uniformly ascending tap selection sequence as shown in Figure 4.24. As a result, the sample stream with appended samples can be passed through the reconstruction FIR filter and yield sufficient faithful samples for final image formation.

4.4. Modified zone-based dynamic focusing

In fact, the modified zone-based dynamic focusing technique enables the signal after multi-bit reconstruction to be accurately aligned by taking account of the group delay of the reconstruction filter. Hence, it should in principle achieve identical results with those obtained by a pre-reconstruction $\Delta\Sigma$ beamformer with the conventional zone-based dynamic focusing technique being applied.

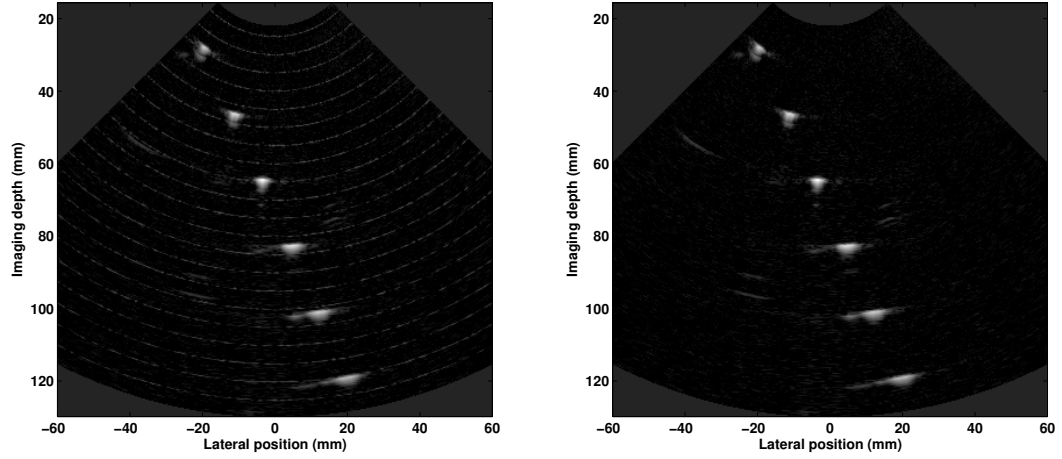
4.4.3 Image quality evaluation

Performance evaluation was carried out by both Field II simulation and phantom studies. Figure 4.25 and 4.26 indicate that the boundary artifacts have been successfully eliminated in the resulting images generated by the modified zone-based dynamic focusing technique a zone depth of 5 mm. It achieves a close beamforming performance in terms of the lateral resolution to that obtained by applying the real time dynamic focusing, as shown in Figure 4.26(c). Reduction in zone depth (i.e., an increase in number of focal zone) intuitively would increase the beamforming performance as the delay is updated more often. Additionally, as to be analyzed in the Section 4.5, the hardware saving (in terms of requirement memory to store the delay information) brought by a reduction in number of focal zone is marginal. Therefore, it is suggested that a relatively small zone depth (i.e., more number of focal zone) should be chosen so that minimal image quality is compromised.

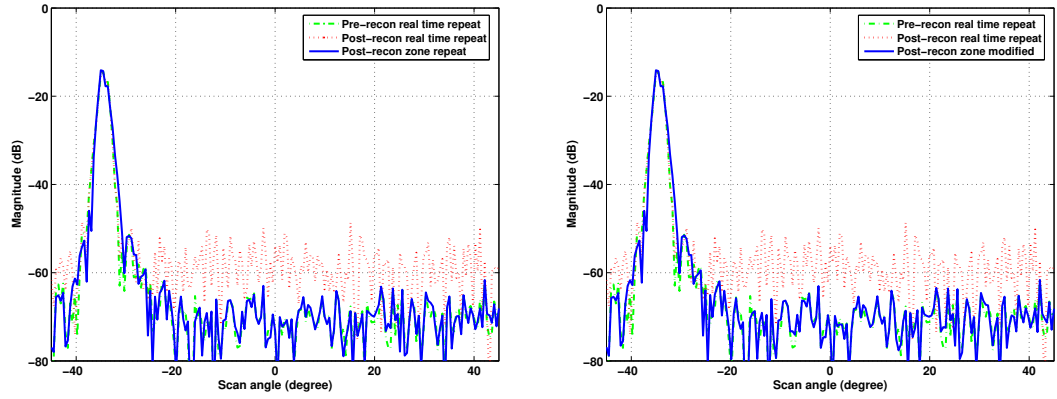
4.4.4 Implementation structure

Since extra processing of $N_r - 1$ samples is required on the bordering of two adjacent focal zones as reflected in Figure 4.24, an additional channel summation

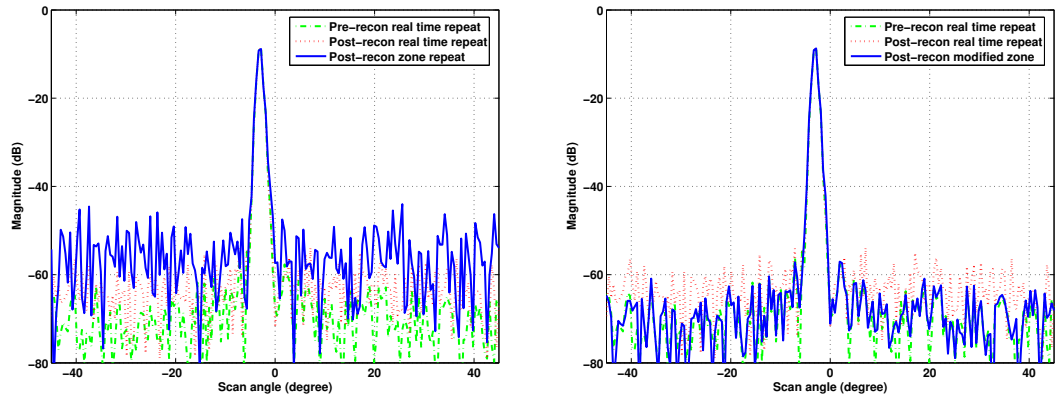
4.4. Modified zone-based dynamic focusing



(a) Gray scale images with 70 dB DR



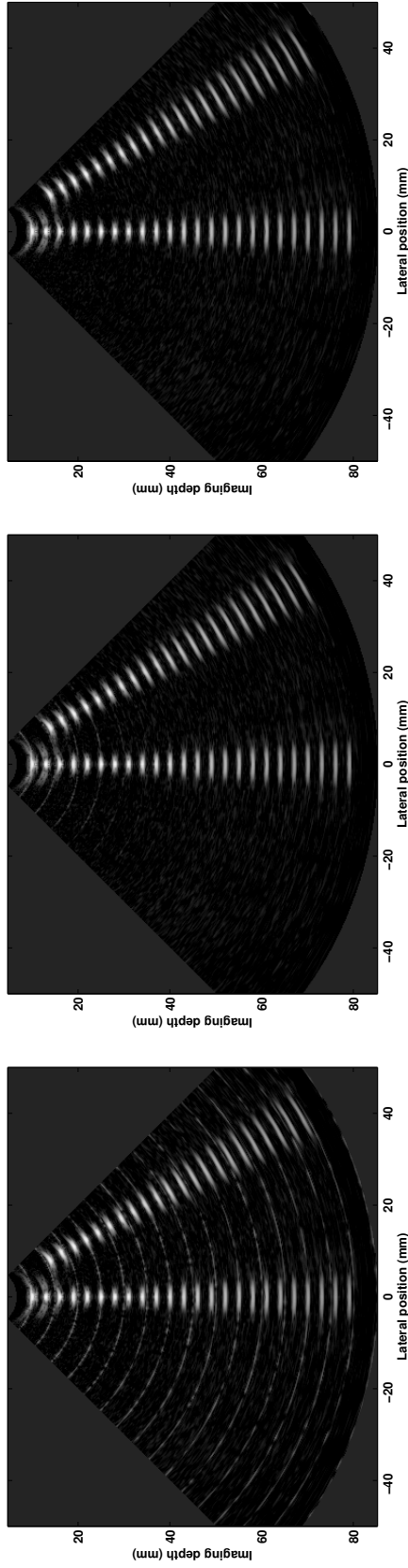
(b) Cross-section views of the 1st wire target (from the top)



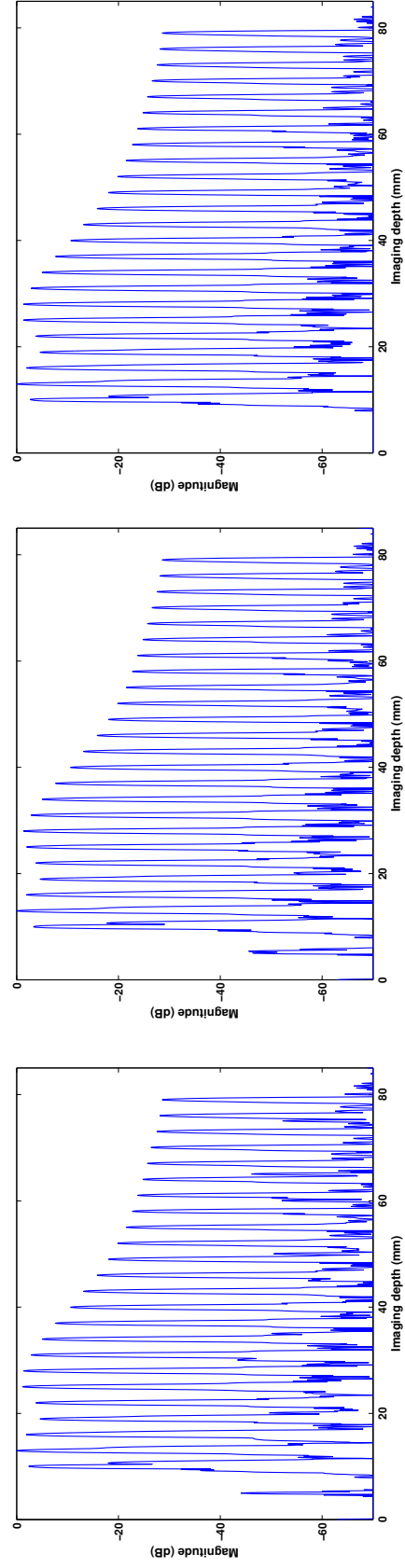
(c) Cross-section views of the 3rd wire target (from the top)

Figure 4.25: Emulation results by the conventional (left column) and modified (right column) zone-based dynamic focusing

4.4. Modified zone-based dynamic focusing



(a) Gray scale images with 70 dB dynamic range



(b) Corresponding A-mode plots of the central scanline

4.4. Modified zone-based dynamic focusing

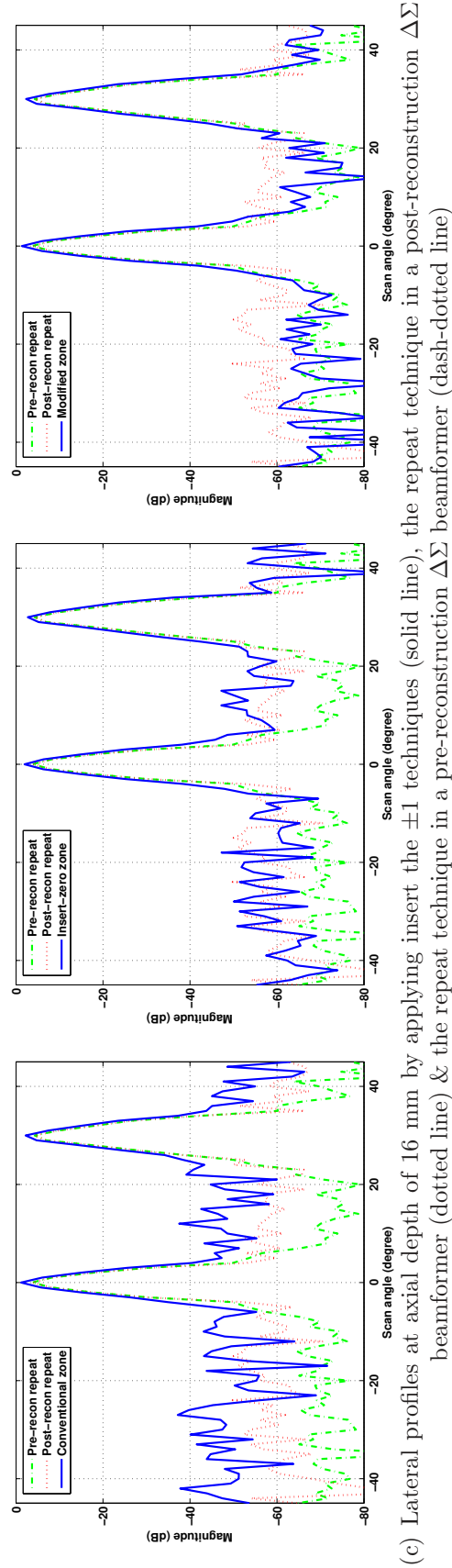


Figure 4.26: Field II simulation results by applying the repeat technique (left column), insert-zero technique (mid column) and modified zone-based dynamic focusing (right column).

4.5. Hardware resources

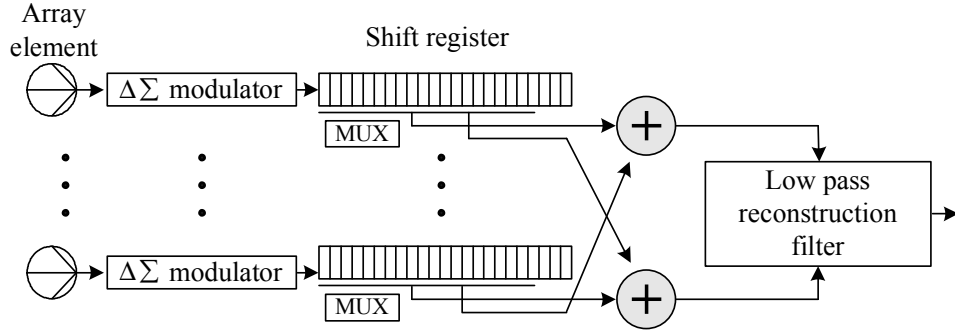


Figure 4.27: Diagram of the $\Delta\Sigma$ beamformer employing the modified zone-based dynamic focusing technique

adder is used to allow alternate processing of the sample stream so that the system synchronization can be maintained. Figure 4.27 illustrates the associated structure of a $\Delta\Sigma$ beamformer employing this theme. In practice, the considerable savings in delay calculation logic would outweigh the additional cost of the adder, which can be economically implemented by a parallel counter, and necessary buffers to accommodate the extra samples.

4.5 Hardware resources

To quantitatively compare the cost of various $\Delta\Sigma$ beamforming methods, the required hardware resources were estimated in terms of the equivalent gate counts and memory required to store the delay information (assuming all the methods using LUT to store the delay information). Table 4.2 lists the associated parameters in the estimation.

As some method presents obvious advantages over another method (e.g., the symmetrical hold method over the insert-zero method), the amount of the hardware resource of four representative methods, i.e., pre-reconstruction $\Delta\Sigma$ beamformer, $\Delta\Sigma$ beamformer with symmetrical holding, $\Delta\Sigma$ beamformer with block

4.5. Hardware resources

Table 4.2: Parameters used in the estimation of hardware resources

Parameter	Specification
Type of transducer	Linear
Number of active elements in receive	64
Transducer center frequency (MHz)	3.5
Transducer pitch (mm)	0.22
Sound speed (m/s)	1540
Sampling rate (MHz)	224
Imaging depth (cm)	15
Tap number of the reconstruction filter by direct implementation	160
Tap number of FIR filter followed by CIC decimation filter	30
Bit length of reconstructed sample before beamforming summation	8
Bit length of reconstructed sample after beamforming summation	12
Number of accumulator required in each channel in block based $\Delta\Sigma$ beamforming	10

based selection and $\Delta\Sigma$ beamformer with modified zone-based dynamic focusing would be estimated and compared.

Pre-reconstruction $\Delta\Sigma$ beamformer

Pre-reconstruction $\Delta\Sigma$ beamformer is selected as a reference. In principle, it can produce the best image quality among all these $\Delta\Sigma$ beamforming methods. Figure 4.28 illustrates the implementation structure of a pre-reconstruction $\Delta\Sigma$ beamformer. As the output of the $\Delta\Sigma$ modulator is merely ± 1 , the pre-reconstruction filter in each channel, requiring no multiplication, is implemented by a binary tree multi-operand adder. The adder output is truncated to 8 bit ready for beamforming sample selection. Only required samples, determined by the delay information,

4.5. Hardware resources

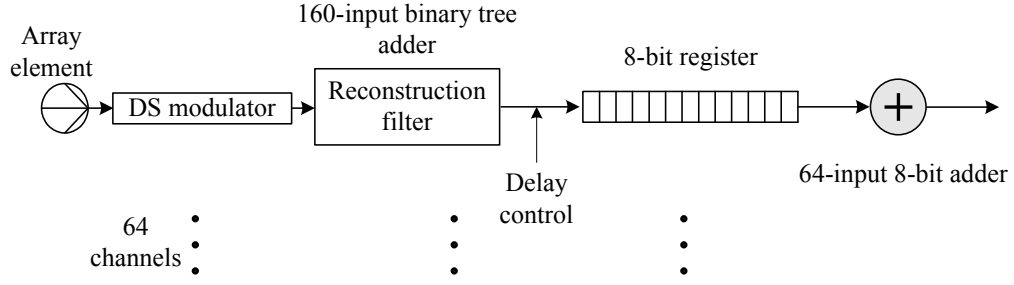


Figure 4.28: Implementation of a pre-reconstruction $\Delta\Sigma$ beamformer

are store in the subsequent 8-bit registers for beamforming summation. Based on a minimum f -number of two, the number of register required to accommodate the net dynamic delay among respective channels over the period of every beam is computed to be 8. Table 4.3 lists the required hardware resource for the pre-reconstruction $\Delta\Sigma$ beamformer. The gate count was obtained by synthesizing the building blocks using Synopsys® with AMS 0.35 μm process, which will be used throughout this estimation.

As computed in Chapter 4.4, the required number of delay update in each receive channel is 43,636 for an imaging depth of 15 cm. By using delta-coding, which stores the delay difference in consecutive beamforming samples, it is feasible to use 1 bit memory (e.g., either repeat using '1' or not repeat using '0') to store the delay information. Hence, the total required memory would be $43,636 \times 64 = 2,792,704$ bits.

$\Delta\Sigma$ beamformer with symmetrical holding

The symmetrical holding method presents the advantage over the insert-zero and divided-by-two methods as the single-bit merit is reserved [30]. It is also more preferred over the $\Delta\Sigma$ beamforming methods using compensated modulators due to the fact that only standard modulator is required. As compared to $\Delta\Sigma$ beamformer with ADUM, the cost difference might be negligible. Figure 4.29 illustrates

4.5. Hardware resources

Table 4.3: Estimated hardware resources for pre-reconstruction $\Delta\Sigma$ beamformer

Function block	Gates	Number	Subtotal
Reconstruction filter			
2-input 8-bit adder	30	80×64	153,600
2-input 9-bit adder	34	40×64	87,040
2-input 10-bit adder	38	20×64	48,640
2-input 11-bit adder	42	10×64	26,880
2-input 12-bit adder	46	5×64	14,720
2-input 13-bit adder	49	2×64	6,272
2-input 14-bit adder	53	2×64	6,784
2-input 15-bit adder	57	1×64	3,648
Beamformer adder			
64-input 8-bit adder	2,059	1	2,059
Delay line registers			
8-bit register	32	8×64	16,384
Total gate counts	366,027		
Total memory (bit)	2,792,704		

4.5. Hardware resources

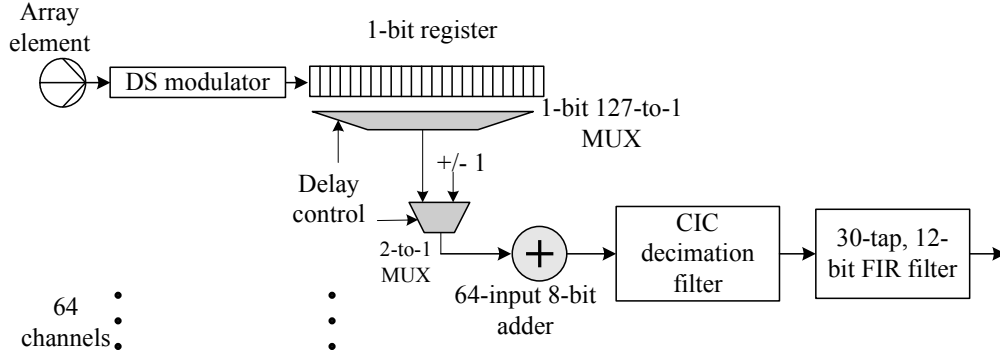


Figure 4.29: Implementation of $\Delta\Sigma$ beamformer with symmetrical holding

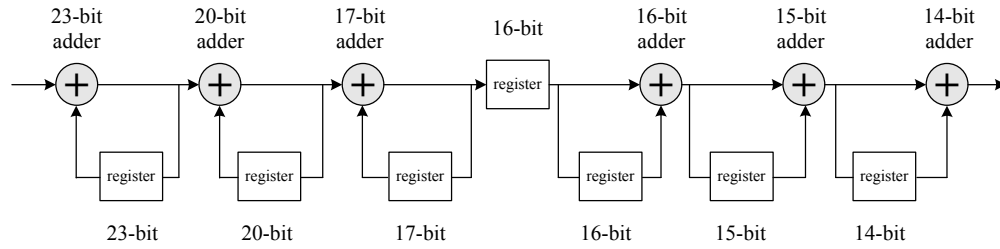


Figure 4.30: Implementation of a CIC filter

the implementation struction used in the estimation. The required delay is applied on the single-bit sample stream. The number of single-bit register required to accommodate the net dynamic delay is calculated to be 127. The reconstruction and decimation are realized by the commonly used Cascaded Integrator Comb (CIC) filter [52] followed by a normal FIR filter. The structure of the CIC filter, designed by MATLAB[®] toolbox, is shown in Figure 4.30. Table 4.4 lists the estimated hardware resources.

$\Delta\Sigma$ beamformer with block based selection

$\Delta\Sigma$ beamformer with block based selection enables a reduced beamforming frequency at the Nyquist rate. Hence, it also presents the potential to reduce the memory requirement for delay information storage. According to the listed parameters in Table 4.2, the required number of accumulator in each receive channel is 10 for a minimum beamforming frequency of 14 MHz.

4.5. Hardware resources

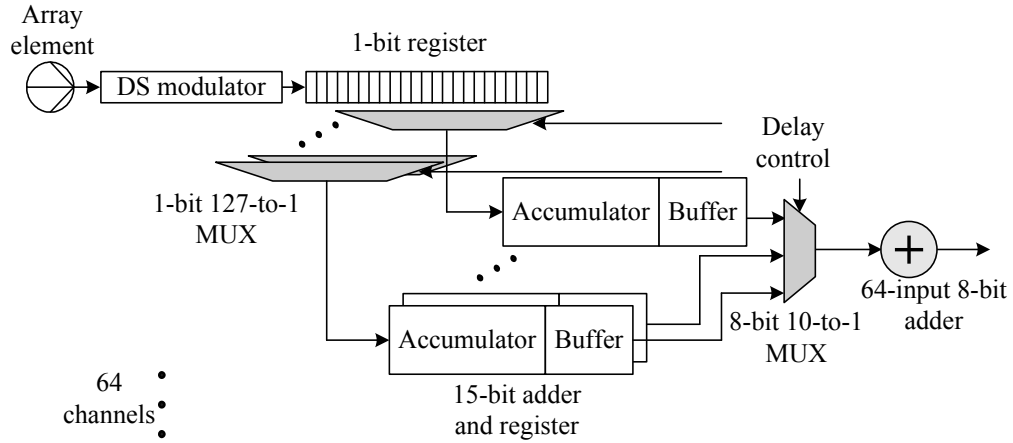


Figure 4.31: Implementation of a $\Delta\Sigma$ beamformer with block based selection

Notice that in Figure 4.31 7-bit memory (to select 1 from 127) is needed for store the delay information for each beamforming sample. Single-bit delta-coding cannot be used here due to a reduced beamforming frequency, which increases the delay difference between consecutive beamforming samples.

$\Delta\Sigma$ beamformer with modified zone-based dynamic focusing

Figure 4.32 illustrates the implementation of the proposed $\Delta\Sigma$ beamformer with modified zone-based dynamic focusing. The construction of the CIC filter is the same as that in the symmetrical holding method, although two of them are required here. The subsequent register is used as buffer to store the overlapped samples at the zone boundaries. The register length is just equal to the group delay the FIR filter as reflected in Table 4.6.

Summary

Table 4.7 is presented to summarize the estimated hardware resources. The gate counts ratio was calculated by taking the pre-reconstruction $\Delta\Sigma$ beamformer as reference. It is found that the symmetrical holding method achieves a significant

4.5. Hardware resources

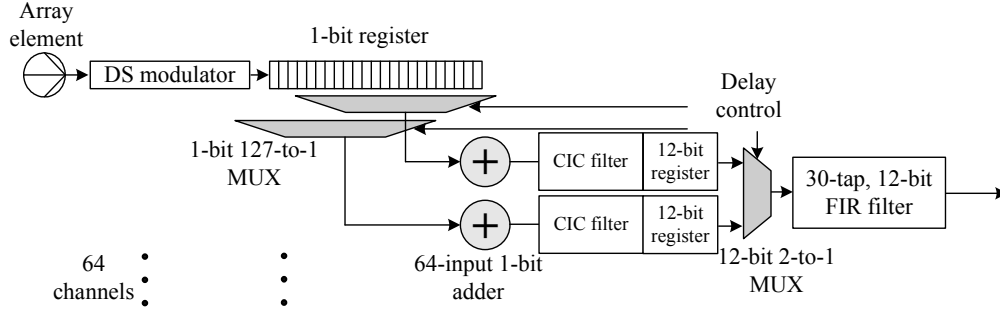


Figure 4.32: Implementation of a $\Delta\Sigma$ beamformer with modified zone-based dynamic focusing

reduction in gate counts but no savings in memory requirement. Block-based method achieve almost 50 % savings in both gate counts and required memory.

Only the proposed $\Delta\Sigma$ beamformer with modified zone-based dynamic focusing achieves a dramatic reduction in both gate counts and memory requirement. An increased the number of focal zone for better beamforming performance will not change the gate counts. The associated memory requirement for different number of focal zone is shown in Table 4.8. It shows that the extra memory savings in percentage brought by a reduction in number of focal zone is negligible (e.g., reduction from 40 zones to 10 zones provides 0.47 % extra savings in the required memory).

4.5. Hardware resources

Table 4.4: Estimated hardware resources for $\Delta\Sigma$ beamformer with symmetrical holding

Function block	Gates	Number	Subtotal
Reconstruction filter			
2-input 12-bit adder	46	30	1,380
2-input 12-bit multiplier	699	15	10,485
2-input 23-bit adder	88	1	88
2-input 20-bit adder	76	1	76
2-input 17-bit adder	64	1	64
2-input 16-bit adder	61	1	61
2-input 15-bit adder	57	1	57
2-input 14-bit adder	53	1	53
23-bit register	92	1	92
20-bit register	80	1	80
17-bit register	68	1	68
16-bit register	64	2	128
15-bit register	60	1	60
14-bit register	56	1	56
13-bit register	52	1	52
Beamformer adder			
64-input 1-bit adder	538	1	538
Delay line registers			
1-bit register	4	127 \times 64	32,512
Beamformer controller			
1-bit 127-to-1 MUX	158	64	10,112
1-bit 2-to-1 MUX	1.25	64	80
Total gate counts	56,042		
Total memory (bit)	2,792,704		

4.5. Hardware resources

Table 4.5: Estimated hardware resources for $\Delta\Sigma$ beamformer with block based selection

Function block	Gates	Number	Subtotal
Reconstruction filter			
2-input 15-bit adder	57	10×64	36,480
15-bit register	60	10×64	38,400
Beamformer adder			
64-input 8-bit adder	2,059	1	2,059
Delay line registers			
1-bit register	4	127×64	32,512
Beamformer controller			
1-bit 127-to-1 MUX	158	10×64	101,120
8-bit 10-to-1 MUX	90	1	90
Total gate counts	210,661		
Total memory (bit)	1,222,144		

4.5. Hardware resources

Table 4.6: Estimated hardware resources for $\Delta\Sigma$ beamformer with modified zone-based dynamic focusing

Function block	Gates	Number	Subtotal
Reconstruction filter			
2-input 12-bit adder	46	30	1380
2-input 12-bit multiplier	699	15	10,485
2-input 23-bit adder	88	2	176
2-input 20-bit adder	76	2	152
2-input 17-bit adder	64	2	128
2-input 16-bit adder	61	2	122
2-input 15-bit adder	57	2	114
2-input 14-bit adder	53	2	106
23-bit register	92	2	184
20-bit register	80	2	160
17-bit register	68	2	136
16-bit register	64	4	256
15-bit register	60	2	120
14-bit register	56	2	112
13-bit register	52	2	104
Beamformer adder			
64-input 1-bit adder	538	2	1,076
12-bit register	48	30	1,440
Delay line registers			
1-bit register	4	127×64	32,512
Beamformer controller			
1-bit 127-to-1 MUX	158	64	10,112
12-bit 2-to-1 MUX	15	1	15
Total gate counts	58,890		
Total memory (bit)	4,480		

4.5. Hardware resources

Table 4.7: Summary of hardware resources

	Pre-reconstruction	Symmetrical holding	Block based	Modified zone-based
Total gate counts	366,027	56,042	210,661	58,890
Gate counts ratio	1	0.153	0.576	0.161
Total memory for delay information (bit)	2,792,704	2,792,704	1,222,144	4,480
Memory ratio	1	1	0.438	0.0016

Table 4.8: Memory requirement in change of number of focal zone

Number of focal zone	10	20	30	40
Total memory for delay information (bit)	4,480	8,960	13,440	17,920
Memory ratio	0.0016	0.0031	0.0047	0.0063

4.6 Conclusion

Oversampled $\Delta\Sigma$ beamformers present the potential to dramatically reduce the size and complexity of ultrasound machine front-end electronics. Several efficient approaches, namely employing the compensated $\Delta\Sigma$ modulator with zero-feedback, insert ± 1 technique with ADUM and the modified zone-based dynamic focusing technique, are proposed to suppress the unfriendly dynamic focusing artifacts in a post-reconstruction $\Delta\Sigma$ beamformer. Therefore, the $\Delta\Sigma$ beamformer is capable of producing premium image quality, which makes it appealing as a potential cost effective frond-end solution for HUS.

Except for the sparse sampling technique (block-based method) and the modified zone-based dynamic focusing technique, all the other approaches so-far disclosed are essentially empirical. The insert-zero, divide-by-2 and insert ± 1 techniques attempt to stretch the sample stream with its moving average unaltered. Whereas, the compensated $\Delta\Sigma$ modulators force the integrator output to track the associated stretched stream (with either repeated or inverted samples) by adjusting the feedback level accordingly. Therefore, they do share the same trait that outputs of the modulator integrators represent a sufficiently faithful interpretation of the moving average of the subsequently stretched sampling stream. By complying with this principle, qualified images can be obtained by suppressing the dynamic focusing artifacts to a decent level below the system dynamic range.

Table 4.9 presents a brief summary of existing dynamic focused $\Delta\Sigma$ beamforming techniques with various configurations. In practice, the modified zone-based dynamic focusing technique requires less complex logic and enables a substantially reduced memory requirement for delay information storage. Hence, it is suitable for low-cost-targeted system and could be potentially employed in HUS in the

4.6. Conclusion

future.

Nonetheless, it is prudent to bear in mind that development of a high sampling rate second-order $\Delta\Sigma$ modulator suitable for medical ultrasonic imaging may incur an increased price with the state-of-the-art VLSI technology. A majority of existing designs of the low-pass second-order $\Delta\Sigma$ modulator are actually suitable for applications in the audio range. A recently reported design based on a 0.35 CMOS process produces a measured peak SQNR of merely 37 dB at a sampling rate of 200 MHz [43]. And a more optimistic design achieves a maximum SQNR of 48 dB in the post-layout simulation operating at 250 MHz [53]. For a transducer with $f_0 = 7.5$ MHz, however, the favorable sampling rate would be even as high as $f_s = 64 \cdot f_0 = 480$ MHz, which yields a formidable challenge in design with contemporary low cost CMOS processes [43]. In addition, performance evaluation in the reported designs has been restricted to feed of the low-pass input signals, whereas ultrasound echoes are of the bandpass characteristic in nature. Therefore, extensive testing and measurement by using the real ultrasound echoes still need to be done before a feasible configuration can be finalized.

In conclusion, the appealing features of $\Delta\Sigma$ beamformer presents its potential application in HUS, provided that development of the required high sampling rate $\Delta\Sigma$ modulator at affordable price can be fulfilled in the near future.

4.6. Conclusion

Table 4.9: Summary of various $\Delta\Sigma$ beamforming techniques with dynamic receive focusing

	beamforming frequency	delay update frequency	delay resolution	delay line bit-width	remarks
Repeat	$64 \cdot f_0$	$64 \cdot f_0$	$\frac{1}{64 \cdot f_0}$	1	significant dynamic focusing artifacts
Repeat with 2-X buffer modulator	$64 \cdot f_0$	$64 \cdot f_0$	$\frac{1}{64 \cdot f_0}$	1	suppressed artifacts, customized modulator, slightly degraded near-field performance
Inverse inversion with zero-feedback modulator	$64 \cdot f_0$	$64 \cdot f_0$	$\frac{1}{64 \cdot f_0}$	1	suppressed artifacts, customized modulator, slightly degraded near-field performance
Insert-zero	$64 \cdot f_0$	$64 \cdot f_0$	$\frac{1}{64 \cdot f_0}$	2	suppressed artifacts, increased bit-width
Divided-by-2	$64 \cdot f_0$	$64 \cdot f_0$	$\frac{1}{64 \cdot f_0}$	2	suppressed artifacts, increased bit-width
Symmetrical- hold	$64 \cdot f_0$	$64 \cdot f_0$	$\frac{1}{64 \cdot f_0}$	1	suppressed artifacts, slightly degraded performance in near-field
Insert ± 1 with HDRM	$64 \cdot f_0$	$32 \cdot f_0$	$\frac{1}{32 \cdot f_0}$	1	suppressed artifacts, degraded delay resolution

4.6. Conclusion

Table 4.9 – continued from previous page

	beamforming frequency	delay update frequency	delay resolution	delay line bit-width	comment
Insert ± 1 with ADUM	$64 \cdot f_0$	$64 \cdot f_0$	$\frac{1}{64 \cdot f_0}$	1	suppressed artifacts
Non-uniform sampling	$< 64 \cdot f_0$	$64 \cdot f_0$	$\frac{1}{64 \cdot f_0}$	1	suppressed artifacts, huge memory for clock generator
Modified zone-based	$64 \cdot f_0$	very low	$\frac{1}{64 \cdot f_0}$	1	suppressed artifacts, simple delay control logic, substantially reduced memory requirement
Block based	$4 \cdot f_0$	$4 \cdot f_0$	$\frac{1}{64 \cdot f_0}$	block selection	suppressed artifacts, reduced memory requirement, complicated delay control logic

Chapter 5

Digital beamforming based on the bandpass sampling principle

This chapter reviews the principle of the bandpass sampling technique. Based on the assumption that received echoes are relatively narrow-band signals, the bandpass sampling principle allows a reduced beamforming frequency to be used, thus leading to a reduction in computational requirement. Two preferred embodiments are proposed to reduce the data processing rate in a post-filtering baseband PRB and a pre-reconstruction $\Delta\Sigma$ beamformer with block-based delay respectively.

5.1 Bandpass sampling principle

The earlier discussion in Chapter 3 and 4 on the configuration of the digital beamformer is based on the low-pass signal processing principle and therefore the Nyquist sampling criteria has to be satisfied. As indicated in equation 2.1, however, the received echo takes on the bandpass nature, which can be modelled as an amplitude modulated (AM) signal with a finite bandwidth. In addition, the carrier frequency is known as the transducer resonance frequency f_0 . Hence, it is

5.1. Bandpass sampling principle

intuitively feasible to apply the bandpass sampling principle in digital beamformation.

The associated benefits are the reduced sampling rate of the ADCs in all Rx-channels [54] and the reduction in data throughput, which leads to a saving in the digital memory used to store the echo samples. The following discussion reviews the principle of bandpass sampling, which serves as a theoretical basis for its application in digital beamformation.

Bandpass sampling, also termed intermediate frequency (IF) sampling or harmonic sampling, has been widely used in digital communication and radar system. The bandpass sampling theorem states that: a signal of bandwidth f_B , occupying the frequency range between $f_0 - f_B/2$ and $f_0 + f_B/2$, can be uniquely reconstructed from the samples if sampled at a rate f_s which complies with [45]:

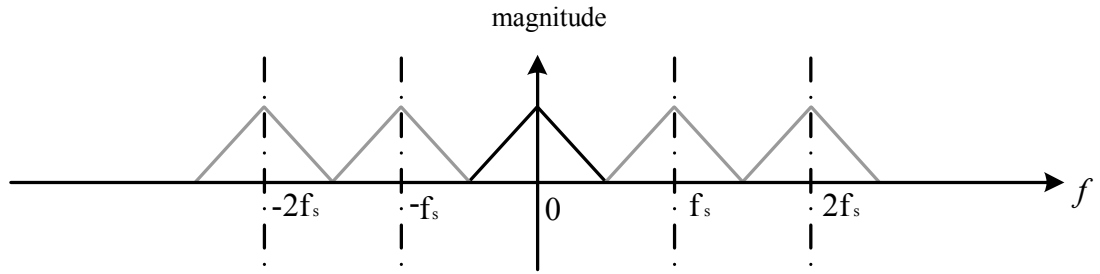
$$\frac{2 \times f_0 + f_B}{q + 1} \leq f_s \leq \frac{2 \times f_0 - f_B}{q}, \quad (5.1)$$

where q is an arbitrary positive integer ensuring that $f_s \geq 2 \cdot f_B$. Unlike the low-pass sampling scheme, which requires $f_s \geq 2 \cdot f_0 + f_B$ to avoid spectral ambiguity as depicted in Figure 5.1(a) and 5.1(b), the bandpass sampling scheme enables a potential sampling rate less than f_0 provided that f_B is sufficiently small.

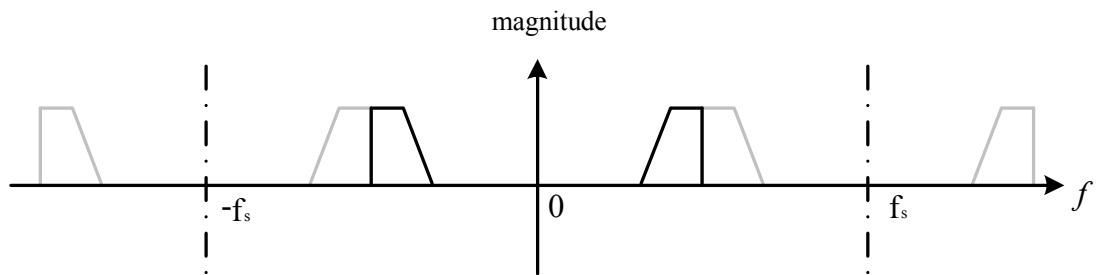
Figure 5.1(c) plots the resulting spectral replications due to discrete time sampling in the bandpass sampling scheme. This example illustrates that there are spectral replications lying in between the original analog signal spectrum, which is distinctive from the low-pass sampling scheme as reflected in Figure 5.1(b).

As equation 5.1 is subject to $f_s \geq 2 \cdot f_B$, thus yielding $(2 \cdot f_0 - f_B)/q \geq 2 \cdot f_B$, there is a maximum fractional bandwidth of 66.7 % for the bandpass sampling

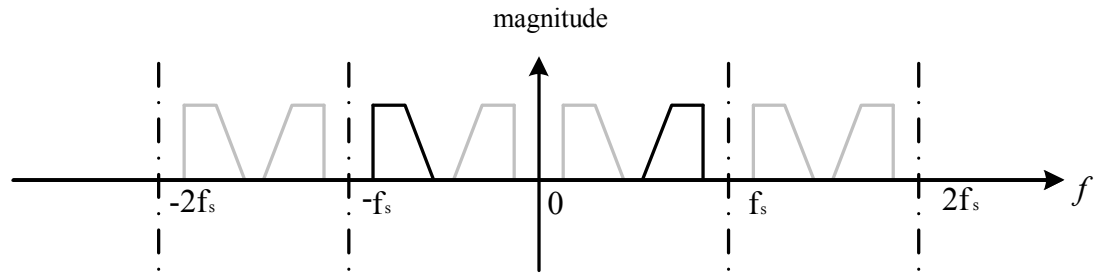
5.1. Bandpass sampling principle



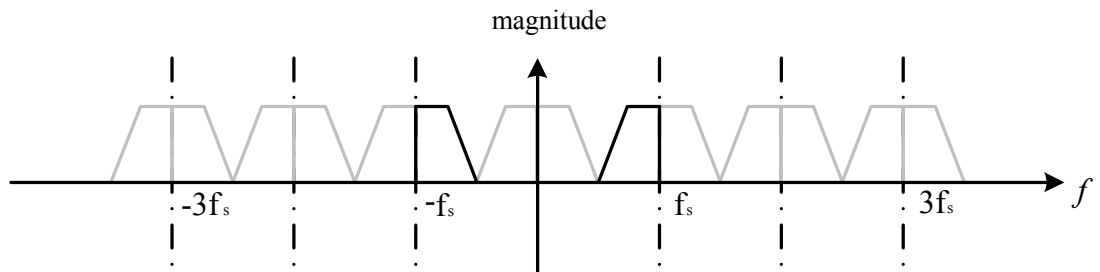
(a) Sample a low-pass signal in the low-pass sampling scheme



(b) Sample a bandpass signal in the low-pass sampling scheme with $f_s = 2 \cdot f_0 + f_B$



(c) Sample a bandpass signal in the bandpass sampling scheme



(d) Sample a bandpass signal in the bandpass sampling scheme with maximum fractional bandwidth with $f_B = \frac{2}{3}f_0$, $f_s = \frac{4}{3}f_0$

Figure 5.1: Spectra of discrete-time signals with dark lines representing the spectrum of the original analog signal and the gray lines representing the spectral replications due to discrete time sampling

5.2. Application in ultrasonic beamformation

technique to be applicable (*i.e.*, $q = 1$ yields $f_B \leq \frac{2}{3}f_0$). Figure 5.1(d) shows the spectrum with all spectral replications butting against each other at this critical fractional bandwidth. A sampling rate of $4 \cdot f_0/3$ is feasible at the moment to digitize the signal without aliasing [45, 54].

5.2 Application in ultrasonic beamformation

In early 1990s, Song *et al.* [55] proposed a modified quadrature sampling technique, enabling ADCs in respective Rx-channels to work at a reduced sampling rate. Based on the relative narrow-band assumption, the modified quadrature sampling technique performs digital sampling at half of the Nyquist rate of the received echoes without frequency aliasing. Although inexplicitly addressed, the modified quadrature sampling technique essentially achieves a reduction in sampling rate as well as beamforming frequency by applying the bandpass sampling principle. Song's proposal thus can be, to the best of the author's knowledge, the earliest effort made to employ the bandpass sampling principle in ultrasonic beamformation.

With such a low sampling rate, the required delay resolution is achieved by employing the pipelined-sampled-delay-focusing (PSDF) scheme [17], referred to as the non-uniform sampling technique in Chapter 2. Accordingly, the required delay is fulfilled by wisely controlling the sampling instances of the ADCs. Song *et al.* suggested that the sampling rate should comply with $f_0 < f_s < 2 \cdot f_0 - f_B$, which is dependent on the fractional bandwidth of the transducer. Based on the envelope of the received ultrasound RF signal in a particular Rx-channel, preliminary experimental results obtained by employing the modified quadrature sampling technique

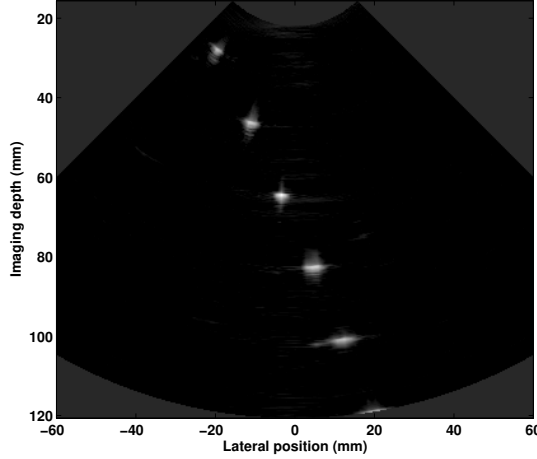
5.2. Application in ultrasonic beamformation

are visually close to those from the conventional low-pass sampling technique [55]. However, no quantitative results or B-mode images were provided.

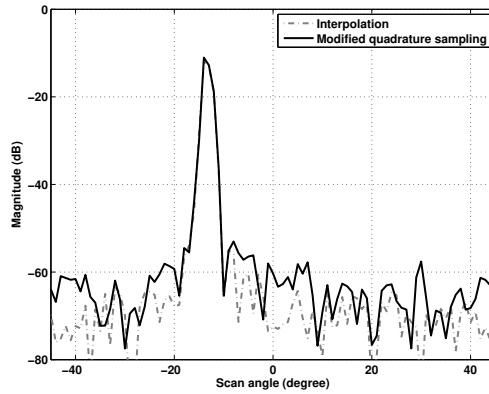
To further investigate its associated beamforming performance, real ultrasound data emulation was carried out by using the Acuson data set. To emulate the non-uniform sampling scheme, the echo samples were upsampled by an interpolation factor of 8 (*i.e.* with an effective delay resolution of $1/f_{eff} = 1/13.9 \times 8 \approx 1/(31.8 \times f_0)$). Only required samples were selected to produce the final beamforming output, where the ultimate beamforming frequency was set to be $13.9/3 = 3.68$ MHz $= 1.32 \times f_0 \approx 4 \cdot f_0/3$. Thus, the results obtained should in principle be identical with those achieved by the modified quadrature sampling technique in which the sample rate is 3.68 MHz and the delay resolution of the SCG is $1/f_{eff} \approx 1/(31.8 \times f_0)$. Figure 5.2 indicates that the reduced sampling rate and/or beamforming frequency lead to a degraded contrast resolution, which is more pronounced in the axial range as reflected in Figure 5.2(c), whereas the spatial resolution is comparable to that from the conventional interpolation beamforming technique with the equivalent delay resolution.

Without SCG, it is also feasible to uniformly sample the echoes at the reduced rate while achieving a favorable delay resolution by digital interpolation. However, the limited usable frequency band as well as the large interpolation factor would require a relatively long-tap FIR filter for sharp roll-off filtering. The costly FIR filter thus might overshadow the hardware savings from the reduced sampling rate. Consequently, the reduced sampling rate arising from the bandpass sampling principle might be unappealing in interpolation based digital beamforming techniques.

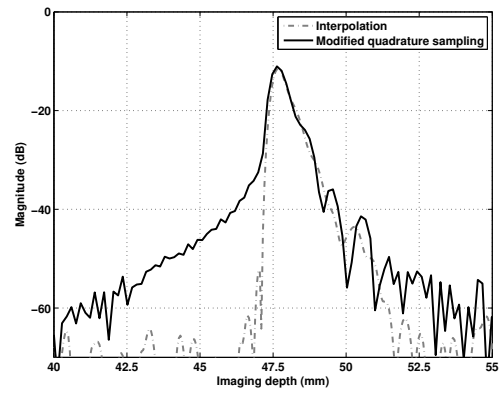
5.2. Application in ultrasonic beamformation



(a) Gray scale image with 60 dB dynamic range



(b) Lateral profile of the 2nd wire target
(from the top)



(c) Axial profile of the 2nd wire target
(from the top)

Figure 5.2: Phantom study results produced by the modified quadrature sampling technique

5.2.1 The modified approach

Notice that digital beamforming is virtually a multi-rate operation involves digital re-sampling (*i.e.* sampling rate conversion). In other words, the sample rate of the delay line, which determines the delay resolution, and the data rate of the beamforming output (*i.e.* the beamforming frequency) are not necessarily to be the same. Therefore, the data rate of the delay lines in respective Rx-channels might maintain at a relatively high frequency (above the Nyquist rate or

5.2. Application in ultrasonic beamformation

even higher for a favorable delay resolution in time-domain digital beamformers), whereas the data rate of the beamforming output is running at a reduced rate based on the bandpass sampling principle. Intuitively, only useful samples required for the ultimate beamforming output as well as their associated delays need to be computed and/or stored in the memory. A reduced computation load can be achieved with a reduced beamforming frequency, which takes on a practical significance in any systems using digital signal processors (DSPs) for the required front-end processing [56].

In pulse-echo B-mode imaging, ultrasound transducers with fractional bandwidth larger than 50 % are usually used to obtain a favorable axial resolution. Some researchers suggested that sharp roll-off filtering can be performed to meet the narrow-band assumption [6]. However, this approach lacks practical significance due primarily to the poor performance of analog filtering, or alternatively the costly digital FIR filters. Therefore, no extra filtering will be considered in the subsequent analysis and simulation. In addition, a preferred beamforming frequency at $f_{BF} = 4 \cdot f_0/3$ (*i.e.* $q = 1$ in equation 5.1) will be employed to minimize the factual aliasing effects, which in principle allows a maximal fractional bandwidth of 66.7 % (*i.e.* $f_B = 2 \cdot f_0/3$). As compared to the low-pass signal sampling scheme with $f_{BF} \geq 2 \cdot f_0 + f_B = 8 \cdot f_0/3$, the bandpass sampling scheme results in a half beamforming frequency.

As described in Chapter 2, Agarwal *et al.* proposed a post-filtering baseband PRB in which the demodulation low-pass filters can be saved by a factor of N_e . To further reduce the computational complexity, a reduced beamforming frequency at $4 \times f_0/3$ was suggested to benefit the development of low-end systems where the substantial reduction in cost and power consumption is needed and a small degradation in image quality would be acceptable [23]. It is essentially an embodiment

5.2. Application in ultrasonic beamformation

of the bandpass sampling principle in the post-filtering baseband PRB.

Nonetheless, as the echo signal within the band of $[\frac{2 \cdot f_0}{3}, \frac{4 \cdot f_0}{3}]$ can be reserved for final image formation only, digital beamformers employing the bandpass sampling principle (with either a reduced sampling rate or reduced beamforming frequency only) are susceptible to a degraded performance due primarily to the aliasing effects and narrower functional bandwidth. In practice, it might be useful in some specific applications, such as in the monitoring mode or duplex scanning mode in which a reasonable B-mode image quality is acceptable [1, 6], to lower the power consumption and/or computational requirement. The following section describes the practical embodiment of this principle in a pre-reconstruction $\Delta\Sigma$ beamformer with block-based delay.

5.2.2 Embodiment in a $\Delta\Sigma$ beamformer

As described in Chapter 4, a pre-reconstruction $\Delta\Sigma$ beamformer can produce error-free dynamic focused images. However, it requires a costly long-tap FIR filter per channel to remove the modulated quantization noise prior to beamforming summation. Han *et al.* proposed a novel architecture for implementation of the pre-reconstruction $\Delta\Sigma$ beamformer [44, 57]. In this approach, time delay is fulfilled on the block-based sample selection. Supposing that each Rx-channel is equipped with an N_r -tap reconstruction filter, then N_r consecutive samples as a block would be selected (according to the required beamforming delay) to pass through the reconstruction filter. Since the output sequence of the $\Delta\Sigma$ modulator consists of merely ± 1 , an efficient digital filter can be realized with a simple accumulator. In particular, the long-tap FIR filter can be replaced with a simple accumulator to add the filter coefficients only.

5.2. Application in ultrasonic beamformation

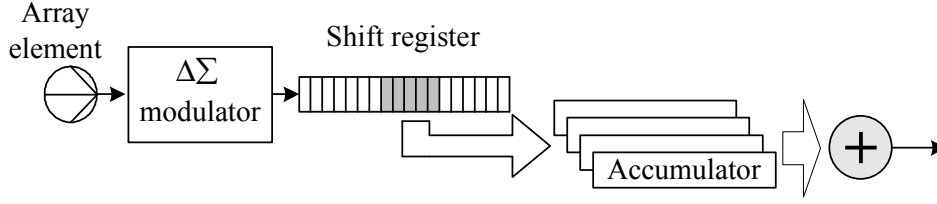


Figure 5.3: Schematics of a $\Delta\Sigma$ beamformer with block-based delay

Based on the Nyquist criteria, Han *et al.* suggested a beamforming frequency of $f_{BF} = 4 \cdot f_0$, *i.e.* the data rate of beamforming output sequence is $4 \cdot f_0$. More precisely, a minimum beamforming frequency of $f_{BF_{min}} = 2 \cdot f_0 + f_B$ in principle is required. In order to maintain system synchronization, therefore, the number of accumulator N_a required per channel to process the modulator output samples in parallel can be given by [44, 57]:

$$N_a = \lceil N_r / OSR \rceil = \lceil N_r \cdot f_{BF_{min}} / f_s \rceil, \quad (5.2)$$

where $\lceil \cdot \rceil$ rounds up the number to the nearest integer and $OSR = f_s / f_{BF_{min}}$. Figure 5.3 shows the scheme of this efficient implementation. As compared to the conventional multi-bit DAS beamformer, the $\Delta\Sigma$ beamformer with block-based delay requires smaller hardware complexity since no complicated digital multiplication or convolution is involved. Tomov *et al.* later developed a compact $\Delta\Sigma$ beamformer with the sparse sampling technique [40], which essentially uses a similar concept.

In practice, N_r is a large number, *e.g.* Han chose $N_r = 160$, as high performance filtering is needed to remove the high frequency quantization noise in $\Delta\Sigma$ modulation. Thus, it undesirably results in a large N_a . Based on the preceding

5.3. Conclusion

discussion, a reduced beamforming frequency, given by:

$$f'_{BF_{min}} = \frac{2 \cdot f_0 + f_B}{q + 1} , \quad (5.3)$$

can be achieved. Consequently, the number of accumulators per channel can be calculated by:

$$N'_a = \left\lceil N_r / OSR' \right\rceil = \left\lceil N_r \cdot f'_{BF_{min}} / f_s \right\rceil , \quad (5.4)$$

Let $q = 1$ to account for the relatively wide-band nature of the ultrasound echoes in B-mode imaging, equation 5.3 and 5.4 yield:

$$N'_a = \left\lceil \frac{4 \cdot N_r f_0}{3 \cdot f_s} \right\rceil , \quad (5.5)$$

which is approximately half of that in Han's proposal as given by:

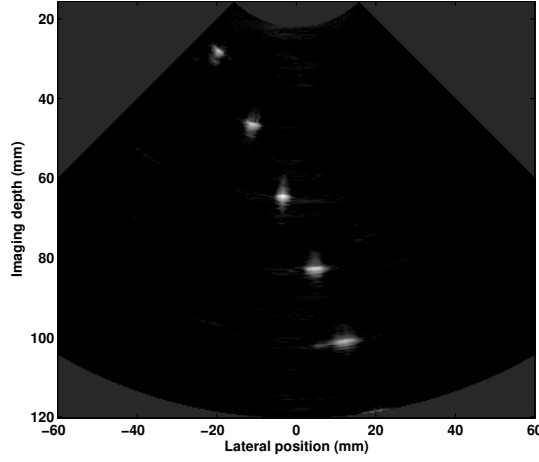
$$N_a = \left\lceil \frac{8 \cdot N_r f_0}{3 \cdot f_s} \right\rceil . \quad (5.6)$$

Figure 5.4 presents the phantom study results by using the Acuson data set. The sampling rate of the $\Delta\Sigma$ modulator was $f_s = 222.2$ MHz and $N_r = 181$. The beamforming frequency was set to be $f_{BF} = 13.9/3$ MHz $\approx 4 \cdot f_0/3$, thus yielding $N'_a = 4$ based on equation 5.5. Similarly, the resulting image suffers from a degraded contrast resolution as reflected in Figure 5.4(b) and 5.4(c).

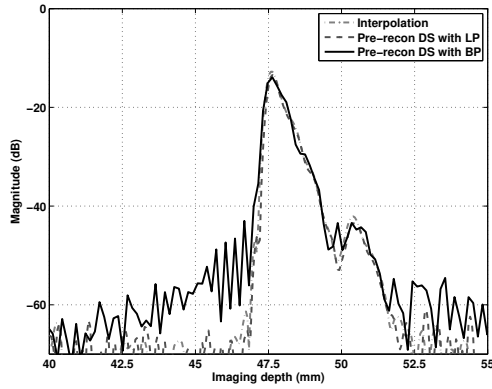
5.3 Conclusion

As typical ultrasound echoes in medical ultrasound imaging take on the nature of bandpass signals, it is feasible to apply the bandpass sampling principle in ultra-

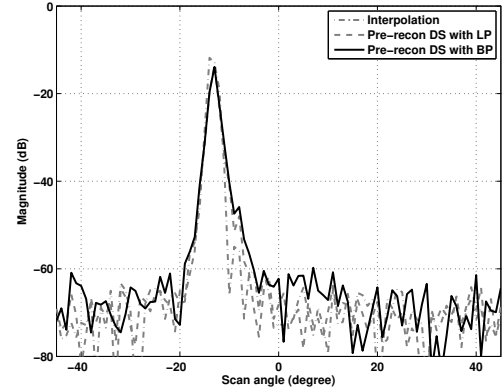
5.3. Conclusion



(a) Gray scale image with 60 dB dynamic range



(b) Lateral profile of the 2nd wire target
(from the top)



(c) Axial profile of the 2nd wire target
(from the top)

Figure 5.4: Phantom study results produced by a pre-reconstruction $\Delta\Sigma$ beamformer with a reduced beamforming frequency. Interpolation, Pre-recon DS with LP and Pre-recon DS with BP represent respectively the interpolation beamforming, block-based DS beamforming proposed by Han *et al.* and the Han's method at a reduced beamforming frequency with bandpass sampling principle being applied

5.3. Conclusion

sonic beamformation. Instead of digitizing the echo signal with a reduced sampling rate in a straightforward manner, the proposed method calls for a reduced beamforming frequency. Consequently, a reduced power consumption and/or computational load as well as data throughput can be achieved. This takes on a practical significance in a system employing DSPs for the front-end signal processing.

However, digital beamforming techniques, including techniques employing the reduced beamforming frequency as well as the modified quadrature sampling technique, suffer from a degraded contrast resolution in B-mode imaging due primarily to the spectral aliasing and/or a narrower functional bandwidth. It is concluded that in applications which do not require very high B-mode image quality, the reduced beamforming frequency arising from the bandpass sampling scheme, would be beneficial since a significant reduction in power consumption, computational workload and/or hardware resources can be achieved.

In addition, narrow-band pulses with quite a few cycles are usually employed in color flow and spectral Doppler imaging [3, 58]. The limited functional bandwidth in principle is no longer an obstruct in these narrow-band applications. The associated performance to apply the bandpass sampling principle, particularly in CFI using digital beamforming techniques for dynamic receive focusing, will be investigated in the future.

Chapter 6

Conclusion and suggested future work

This chapter presents the preferred front-end solution for a low cost digital beamforming system as a conclusive summary of this work. It concludes with the suggested future work in design and development of the digital beamforming system for potential deployment in the development of HUS.

6.1 The preferred front-end solution

This thesis attempts to seek a cost effective front-end solution by exploring a variety of efficient digital beamforming techniques as well as their implementations.

The proposed fully digital heterodyning PRB gains a particular advantage for the system employing multi-bit Nyquist ADCs, in that only one digital multiplier and necessary digital buffers are required in an arbitrary Rx-channel. The echo phase coherence among Rx-channels is achieved by the phase compensation residing in the heterodyning stage. Therefore, ADCs in respective Rx-channels are

6.1. The preferred front-end solution

allowed to sample the echo signal slightly above the Nyquist rate for high performance digital beamforming, provided that the fractional bandwidth of transducer is no more than 100 %. Simulation and phantom study results show that the developed heterodyning PRB can produce reasonable gray scale image quality in terms of spatial (measured by - 6 dB beamwidth) and contrast resolution with dramatically reduced computational complexity. Hence, the heterodyning PRB may find its application in the development of low-end ultrasound systems (e.g., HUS), where a small image quality degradation is tolerable.

The post-filtering baseband PRB disclosed by Agarwal *et al.* achieves a very close performance as compared to the conventional interpolation beamformer and pre-filtering baseband PRB. If a small degradation in image quality could be acceptable, the bandpass sampling principle might be employed with a reduced beamforming frequency to achieve a significant reduction in computational load and data rate in the post-filtering baseband PRB. Such savings in practice are more valued in a DSP based beamforming system design with extended programmability and reduced cost, which may facilitate the widespread use of ultrasound technology in distributed diagnosis and home healthcare [23].

In addition, oversampled $\Delta\Sigma$ ultrasound beamformer presents the great potential to dramatically reduce the complexity of system front-end electronics. Several techniques have been proposed in this thesis, enabling a $\Delta\Sigma$ beamformer with the efficient post-reconstruction strategy to produce premium image quality. The modified zone-based dynamic focusing technique is particularly appealing in practice due to its significantly reduced effort in delay calculation (or memory requirements). Nonetheless, it is prudent to keep in mind the challenge in the development of a high sampling rate $\Delta\Sigma$ modulator. The associated benefits by employing $\Delta\Sigma$ beamformer into the system would result in significant savings in

6.2. Future work

the hardware cost provided that the modulator development will not incur extra cost into the system.

In conclusion, both the heterodyning PRB and post-filtering baseband PRB can achieve a significant reduction in computational complexity and/or hardware cost. As a low-cost solution, they present the potential for the development of the first generation of the HUS since there are well-established techniques for design of 8 to 10-bit multi-bit Nyquist ADCs working at 30 MHz range. Nonetheless, the produced image quality still needs to be evaluated by clinicians before clinical usage. On the other hand, development of a $\Delta\Sigma$ beamformer suitable for the envisioned HUS can be carried out as the long-term effort.

6.2 Future work

The presented work so far is primarily focused on the receive beamforming. To constitute the entire front-end solution, it is natural to extend our research work into the transmit side. To achieve cost reduction by higher front-end integration, the compact design requirement has aroused the interest in employing the low voltage coded excitation system and efficient transmit apodization in transmit beamforming system.

6.2.1 Low voltage coded excitation system for compact front-end design

In modern ultrasound machines, a high driving voltage is usually used to excite the array elements so as to obtain an advantageous signal-to-noise ratio (SNR)

6.2. Future work

and favorable penetration depth. Due to the peak power constraints arising from the risk of causing tissue damage, the SNR in practice is often limited due to the consideration of patient safety factors. O'Donnell developed the coded excitation technique to increase the transmission power by using a longer encoded pulse to excite the transducer element [22]. Through appropriate pulse compression, it achieves significant improvements in the SNR and penetration depth with minimal compromise of the spatial resolution.

A recent paper reported that in a coded excitation system, it is feasible to excite the array elements with a reduce voltage level (*e.g.* $V_{pp} = 10$ V) while keeping the SNR similar to that in a conventional pulse-echo system employing high driving voltage (*e.g.* $V_{pp} = 80$ V) [59]. The waning voltage level in practice may ease the compact integration of the front-end transmitter as high-voltage pulsers in the conventional pulse-echo system are no longer required.

On the other hand, front-end receivers employing $\Delta\Sigma$ modulators take the advantage in their reduced size and complexity. Therefore, for high integration of the whole front-end (including transmitter and receiver), a low voltage coded excitation system based on $\Delta\Sigma$ modulation has been proposed by the research team in our lab. The preferred embodiment employs the post-reconstruction strategy by performing low pass filtering using only one FIR filter after channel summation. However, it requires a decoder in individual Rx-channel for pulse compression, referred to pre-compression as illustrated in Figure 6.1.

Apparently, it is desirable to perform the pulse-compression after beamforming so that only one decoder is required as depicted in Figure 6.2. Unfortunately, the post-compression technique will degrade the code performance due to the delay update in dynamic receive focusing [60–62]. The continued effort in this work

6.2. Future work

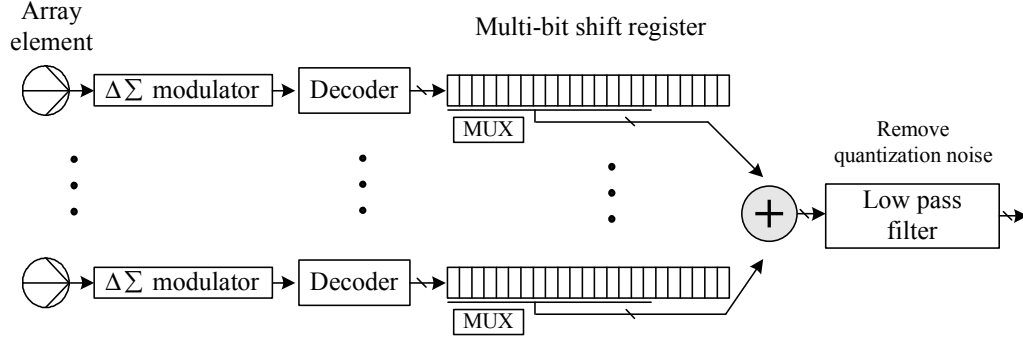


Figure 6.1: Diagram of a $\Delta\Sigma$ based coded excitation system with pre-compression & post-reconstruction

attempts to seek an efficient approach to compensate/minimize this degraded code performance so that a qualified image can be produced by the system employing the post-reconstruction & post-compression strategy.

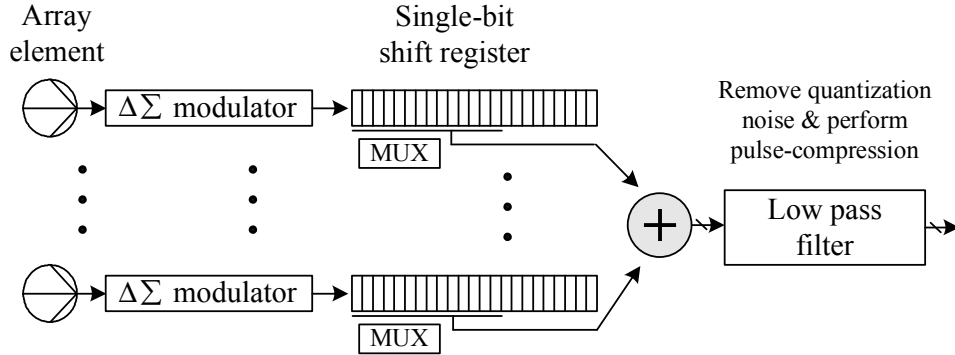


Figure 6.2: Diagram of a $\Delta\Sigma$ based coded excitation system with post-compression & post-reconstruction

6.2.2 Efficient transmit apodization

Array apodization is a well-established technique for improving the system lateral and contrast resolution. In principle, element weighting should be applied in both the transmit and receive beamforming. In most mid-range and low-end commercial systems, however, the element weighting is only fulfilled on receive due to the fact that high-voltage pulser as well as high-voltage linear amplifiers are required for

6.2. Future work

transmit apodization. Figure 6.3 shows the amplitude weighting theme, in which the signal in channel 2 was amplified by a factor of two to fulfill the transmit apodization.

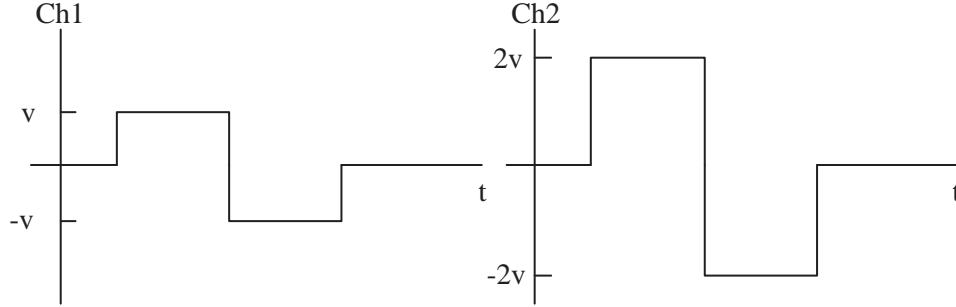


Figure 6.3: Apodization by amplitude weighting

Cincotti *et al.* [63] disclosed an economic approach to realize the transmit apodization by varying the length of the excitation electric pulses. They have demonstrated that the amplitude of the transmitted wave is approximately linear proportional to the duration of the excitation pulse. Hence, transmit apodization can be fulfilled by choosing a series of excitation pulses, which have a constant amplitude but different pulse durations. Figure 6.4 illustrates this scheme, in which the excitation pulse in channel 2 has a doubled duration as compared to that in channel 1 while possessing the same amplitude v .

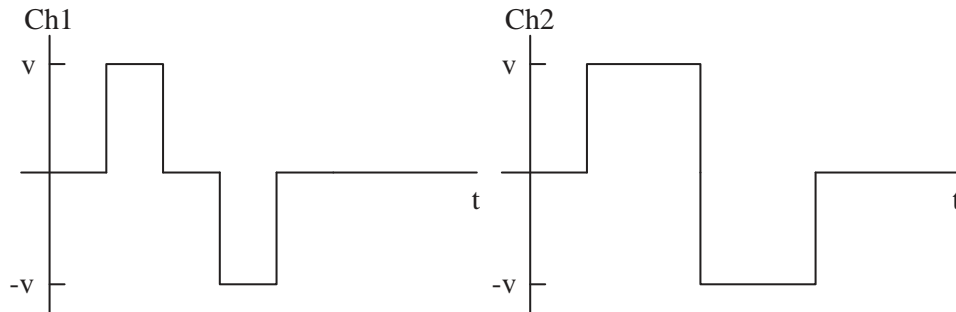


Figure 6.4: Apodization by changing the pulse width

Unlike realization of the receive apodization by digital multipliers with fa-

6.2. Future work

vorably high accuracy, to continuously adjust the pulse duration is prohibitively expensive. Cincotti *et al.* presented the numerical simulation results, but they did not tell the corresponding quantized durations in the experimental study. Therefore, it is desirable to find out the minimum number of the discrete levels for quantization of the variant time durations.

For our proposed low voltage system for compact front-end design, coded excitation approach qualifies a significantly reduced excitation voltage level [59]. Thus, applying transmit amplitude weighting in a coded excitation system is undesirable due to the fact that it utilizes high driving voltages for apodization and would counteract the benefits of a qualified waning voltage. Therefore, the feasibility of applying the pulse width apodization in a low voltage coded excitation system needs to be explored.

Notice that the excitation signal in a binary coded excitation system is generated by convolving the coding kernel (e.g., Golay sequence) and the base sequence (typically a square waveform) [64]. Figure 6.5 presents an illustrative example, with only first 3 digits (1, 1, -1) of the coding kernel being shown, and base sequence being a bipolar square wave to generate the excitation signal. The base sequence length is $4 \times T_{ts}$ and each digit of the coding kernel always has a length of T_{ts} , where T_{ts} is minimum controllable pulse duration provided by the pulser in transmit circuitry. Applying the concept of pulse width control for apodization, it is feasible to generate the excitation signal by the base sequence with reduced length, as shown in Figure 6.6. The corresponding effects on the beamforming performance and resulting hardware savings will be investigated.

6.2. Future work

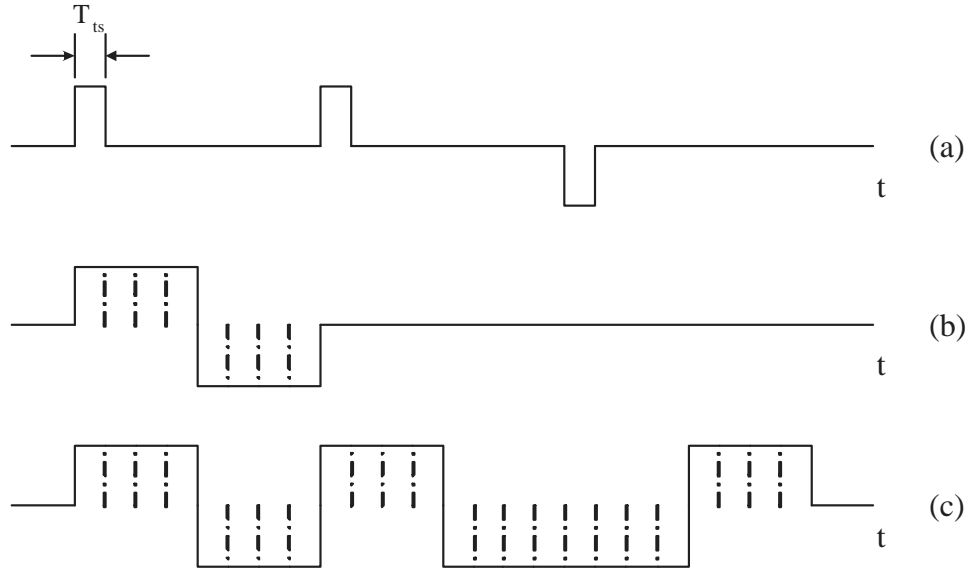


Figure 6.5: Generation of (c) the encoded excitation signal by convolving (a) the coding kernel and (b) the base sequence

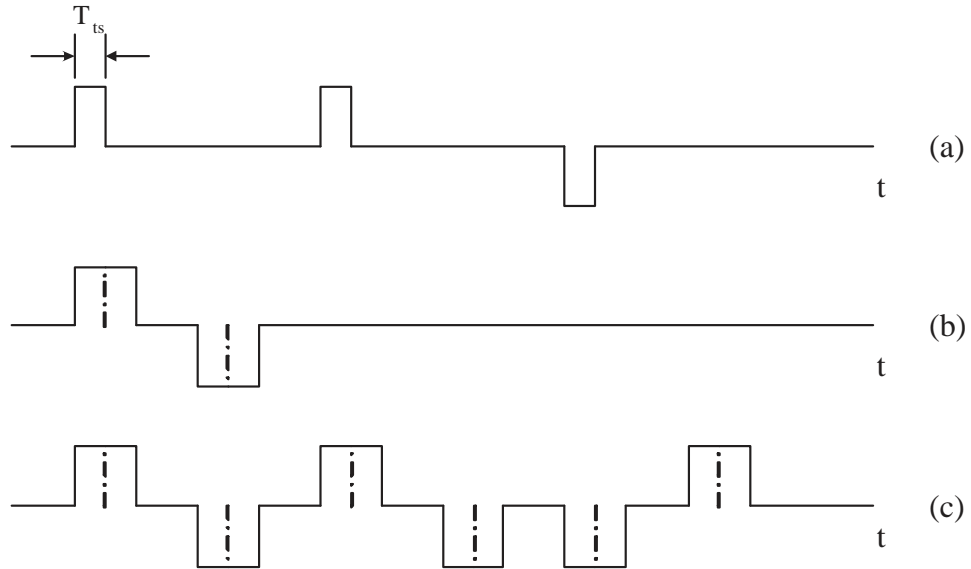


Figure 6.6: Generation of (c) the encoded excitation signal by changing the duration of (b) base sequence while keeping (a) the coding kernel unaltered

Bibliography

- [1] Y.-M. Yoo, Y. Kim, A. Agarwal, and D.-G. Sim, “Home ultrasound system,” U.S. Patent 6,867,720, Nov., 2005.
- [2] W. R. Hedrick, D. L. Hykes, and D. E. Starchman, *Ultrasound Physics and Instrumentation*, 3rd ed. St. Louis, MO: Mosby, 1995.
- [3] C. Kasai, K. Namekawa, A. Koyano, and R. Omoto, “Real-time two-dimensional blood flow imaging using an autocorrelation technique,” *IEEE Trans. Sonics Ultrason.*, vol. SU-32, no. 3, pp. 458–464, 1984.
- [4] D. H. Evans, *Doppler Ultrasound: physics, instrumentation, and signal processing*. New York: John Wiley & Sons, 2000.
- [5] D. H. Johnson and D. E. Dugeon, *Array Signal Processing: concepts and techniques*. Englewood Cliffs, NJ: Prentice-Hall, 1993.
- [6] K. Ranganathan, M. K. Santy, T. N. Blalock, J. A. Hossack, and W. F. Walker, “Direct sampled I/Q beamforming for compact and very low-cost ultrasound imaging,” *IEEE Trans. Ultrason., Ferroelect., Freq. Contr.*, vol. 51, no. 9, pp. 1082–1094, 2004.
- [7] S. R. Freeman, M. K. Quick, M. A. Morin, C. R. Anderson, C. S. Desilets, T. E. Linnenbrink, and M. O’Donnell, “Delta-sigma oversampled ultrasound beamformer with dynamic delays,” *IEEE Trans. Ultrason., Ferroelect., Freq. Contr.*, vol. 46, no. 2, pp. 320–332, 1999.
- [8] M. O’Donnell, *et al.*, “Real-time phased array imaging using digital beam forming and autonomous channel control,” in *Proc. IEEE Ultrason. Symp.*, 1990, pp. 1499–1502.
- [9] W. E. Engeler, M. O’Donnell, J. T. Pedicone, and J. J. Bloomer, “Dynamic phase focus for coherent imaging beam formation,” U.S. Patent 5,111,695, May, 1992.

Bibliography

- [10] R. G. Pridham and R. A. Mucci, "Digital interpolation beamforming for low-pass and bandpass signals," in *Proc. IEEE*, June 1979, pp. 904–919.
- [11] R. A. Mucci, "A comparison of efficient beamforming algorithms," *IEEE Trans. Acoust., Speech, Signal Processing*, vol. ASSP-32, pp. 548–557, 1984.
- [12] D. Lipschutz, "Delay interpolator for digital phased array ultrasound beamformers," U.S. Patent 5,345,426, Sept., 1994.
- [13] S. R. Freeman, "An oversampled ultrasound beamformer for low-power, portable scanners," Ph.D. dissertation, University of Michigan, Ann Arbor, 1998.
- [14] J. E. Powers, D. J. Phillips, M. A. Brandestini, and R. A. Sigelmann, "Ultrasound phased array delay lines based on quadrature sampling techniques," *IEEE Trans. Sonics Ultrason.*, vol. SU-27, no. 6, pp. 287–294, 1980.
- [15] R. G. Pridham and R. A. Mucci, "Shifted sideband beamformer," *IEEE Trans. Acoust., Speech, Signal Processing*, vol. ASSP-27, no. 6, pp. 713–722, 1979.
- [16] W.-H. Cho and Y. B. Ahn, "Multi-order sampling for digital beamforming of wide-band signals," *IEEE Trans. Ultrason., Ferroelect., Freq. Contr.*, vol. 43, no. 3, pp. 216–223, 1996.
- [17] J.-H. Kim, T.-K. Song, and B.-P. Song, "Pipelined sampled-delay focusing in ultrasound imaging systems," *Ultrason. Imag.*, vol. 9, pp. 75–91, 1987.
- [18] M. O'Donnell, W. E. Engeler, J. J. Bloomer, and J. T. Pedicone, "Methods and apparatus for digital phased array imaging," U.S. Patent 4,983,970, Jan., 1991.
- [19] S.-H. Chang, S.-B. Park, and G.-H. Cho, "Phase-error-free quadrature sampling technique in the ultrasonic B-scan imaging system and its application to the synthetic focusing system," *IEEE Trans. Ultrason., Ferroelect., Freq. Contr.*, vol. 40, no. 3, pp. 216–223, 1993.
- [20] B. A. J. Angelsen, *Ultrasound Imaging: waves, signals, and signal processing*. Trondheim, Norway: Emantes, 2000.
- [21] K. Ranganathan and W. F. Walker, "A novel aperture design method for improved depth of field in ultrasound imaging," in *Proc. IEEE Ultrason. Symp.*, Oct. 2001, pp. 1543–1546.

Bibliography

- [22] M. O'Donnell, "Coded excitation system for improving the penetration of real-time phased-array imaging systems," *IEEE Trans. Ultrason., Ferroelect., Freq. Contr.*, vol. 39, no. 3, pp. 341–351, 1992.
- [23] A. Agarwal, F. K. Schneider, Y.-M. Yoo, and Y. Kim, "New demodulation method for efficient phase rotation beamforming," *IEEE Trans. Ultrason., Ferroelect., Freq. Contr.*, vol. 52, no. 5, pp. 870–880, 2006.
- [24] J. E. Volder, "The CORDIC trigonometric computing technique," *IRE Trans. Electron., Comput.*, vol. EC-8, no. 3, pp. 330–334, 1959.
- [25] X.-B. Hu, R. G. Harber, and S. C. Bass, "Expanding the range of convergence of the CORDIC algorithm," *IEEE Trans. Comput.*, vol. 40, no. 1, pp. 13–21, 1991.
- [26] S. H. Maslak, "Acoustic imaging apparatus," U.S. Patent 4,140,022, Feb., 1979.
- [27] S. H. Maslak and J. N. Wright, "Phased array acoustic imaging system," U.S. Patent 4,550,607, Nov., 1985.
- [28] S. H. Maslak and H. G. Larsen, "Dynamically focused linear phased array acoustic imaging system," U.S. Patent 4,699,009, Oct., 1987.
- [29] G. Manes, P. Tortoli, F. Andreuccetti, G. Avitabile, and C. Atzeni, "Synchronous dynamic focusing for ultrasound imaging," *IEEE Trans. Ultrason., Ferroelect., Freq. Contr.*, vol. 35, no. 1, pp. 14–21, 1988.
- [30] P.-C. Li, J.-J. Huang, H.-L. Liu, and M. O'Donnell, "A dynamic focusing technique for delta-sigma based beamformers," *Ultrason. Imag.*, vol. 22, pp. 197–205, 2000.
- [31] D. I. Havelock, "Sensor array beamforming using random channel sampling: The aggregate beamformer," *J. Acoust. Soc. Am.*, vol. 114, no. 4, pp. 1997–2006, 2003.
- [32] J. A. Jensen, "Field: A program for simulating ultrasound systems," *Med. Biol. Eng. Comput.*, vol. 4, no. suppl. 1, pp. 351–353, 1996.
- [33] R. Carotenuto, G. Loi, and M. Pappalardo, "A new extrapolation technique for resolution enhancement of pulse-echo imaging systems," *IEEE Trans. Ultrason., Ferroelect., Freq. Contr.*, vol. 49, no. 3, pp. 374–382, 2002.

Bibliography

- [34] F. Zhang, Y.-M. Yoo, L. M. Koh, and Y. Kim, "Nonlinear diffusion in laplacian pyramid domain for ultrasonic speckle reduction," *IEEE Trans. Med. Imag.*, vol. 26, no. 2, pp. 200–211, 2007.
- [35] S. R. Freeman, M. O'Donnell, T. E. Linnenbrink, M. A. Morin, M. K. Quick, and C. S. Desilets, "Beamformed ultrasonic imager with delta-sigma feedback control," U.S. Patent 5,964,708, Oct., 1999.
- [36] M. Kozak and M. Karaman, "Digital phase array beamforming using single-bit delta-sigma conversion with non-uniform oversampling," *IEEE Trans. Ultrason., Ferroelect., Freq. Contr.*, vol. 48, no. 4, pp. 922–931, 2001.
- [37] K. W. Rigby, "Delta-sigma beamforms with minimal dynamic focusing artifacts," U.S. Patent 6,366,227, Apr., 2002.
- [38] M. Inerfield, G. R. Lockwood, and S. L. Gaverick, "A sigma-delta-based sparse synthetic aperture beamformer for real-time 3-D ultrasound," *IEEE Trans. Ultrason., Ferroelect., Freq. Contr.*, vol. 49, no. 2, pp. 243–254, 2002.
- [39] P.-C. Li, J.-J. Huang, S.-E. Chen, Y.-L. Gau, and T.-Y. Chu, "Focus control method for delta-sigma based image formation device," U.S. Patent 6,895,123, May, 2005.
- [40] B. G. Tomov and J. A. Jensen, "Compact FPGA-based beamformer using oversampled 1-bit A/D converters," *IEEE Trans. Ultrason., Ferroelect., Freq. Contr.*, vol. 52, no. 5, pp. 870–880, 2005.
- [41] D. A. Johns and K. Martin, *Analog Integrated Circuit Design*. New York: John Wiley & Sons, 1997.
- [42] B. D. Steinberg, "Digital beamforming in ultrasound," *IEEE Trans. Ultrason., Ferroelect., Freq. Contr.*, vol. 39, no. 6, pp. 716–721, 1992.
- [43] M. Inferfield, "Sigma-delta modulation in real-time three-dimensional sparse synthetic aperture ultrasound imaging systems," Ph.D. dissertation, Case Western Reserve University, 2002.
- [44] H.-S. Han, H.-J. Park, and T.-K. Song, "A new architecture for ultrasound sigma-delta modulation beamformer," in *Proc. IEEE Ultrason. Symp.*, Oct. 2002, pp. 1631–1634.
- [45] R. G. Lyons, *Understanding Digital Signal Processing*. Englewood Cliffs, NJ: Prentice-Hall, 1997.

Bibliography

- [46] S. R. Freeman, M. O'Donnell, T. E. Linnenbrink, M. A. Morin, M. K. Quick, and C. S. Desilets, "Beamformed ultrasonic imager with delta-sigma feedback control," U.S. Patent 6,867,720, Mar., 2005.
- [47] R. Schreier and G. C. Temes, *Understanding Delta-Sigma Data Converters*. Hoboken, NJ: John Wiley & Sons, 2004.
- [48] R. Adams, "Design and implementation of an audio 18-bit analog-to-digital converter using oversampling techniques," *J. Audio Eng. Soc.*, pp. 153–166, 1986.
- [49] J. A. Cherry and W. M. Snelgrove, *Continuous-Time Delta-Sigma Modulators for High Speed A/D Conversion: theory, practice and fundamental performance limits*. Kluwer Academic Publishers, 1999.
- [50] W. A. Anderson, "Ultrasonic imaging system utilizing dynamic and pseudo-dynamic focusing," U.S. Patent 4,241,610, Dec., 1980.
- [51] F. L. Thurstone and O. T. Von Ramm, "A new ultrasound imaging technique employing two-dimensional electronic beam steering (for medical diagnosis)," in *Proc. 5-th Int. Symp. Acoust. Holograph. Imag.*, July 1973, pp. 249–259.
- [52] E. B. Hogenauer, "An economical class of digital filters for decimation and interpolation," *IEEE Trans. Acoust., Speech, Signal Processing*, vol. ASSP-29(2), pp. 155–162, 1981.
- [53] B. Shem-Tov, M. Kozak, and E. G. Friedman, "A 250 MHz delta-sigma modulator for low cost ultrasound/sonar beamforming applications," in *Proc. IEEE Int. Conf. Electron. Circuits Syst.*, Dec. 2004, pp. 113–116.
- [54] R. G. Vaughan, N. L. Scott, and D. R. White, "The theory of bandpass sampling," *IEEE Trans. Signal Processing*, vol. 39, no. 9, pp. 1973–1984, 1991.
- [55] T.-K. Song and S.-B. Park, "A new digital phased array system for dynamic focusing and steering with reduced sampling rate," *Ultrason. Imag.*, vol. 12, pp. 1–16, 1990.
- [56] Y. Kim, J. H. Kim, C. Basoglu, and T. C. Winter, "Programmable ultrasound imaging using multimedia technologies: a next-generation ultrasound machine," *IEEE Trans. Inform. Technol. Biomed.*, vol. 1, no. 1, pp. 19–29, 1997.
- [57] H.-S. Han, H.-J. Park, and T.-K. Song, "Sigma-delta beamformer and method with reduced artifact," U.S. Application Patent 20 040 189 499, Sept., 2004.

Bibliography

- [58] S. R. Freeman, M. K. Quick, M. A. Morin, C. R. Anderson, C. S. Desilets, T. E. Linnenbrink, and M. O'Donnell, "Heterodyning technique to improve performance of delta-sigma-based beamformers," *IEEE Trans. Ultrason., Ferroelect., Freq. Contr.*, vol. 46, no. 4, pp. 771–790, 1999.
- [59] Y.-M. Yoo, W.-Y. Lee, and T.-K. Song, "A low voltage portable system using modified golay sequences," in *Proc. IEEE Ultrason. Symp.*, Oct. 2001, pp. 1469–1472.
- [60] R. Bjerngaard and J. A. Jensen, "Should compression of coded waveforms be done before or after focusing?" in *Proc. SPIE Med. Imag.*, vol. 4687, Apr. 2002, pp. 47–58.
- [61] T. Azuma, Y. Miwa, and S. ichiro Umemura, "Subaperture decoding to enhance performance of coded excitation," in *Proc. IEEE Ultrason. Symp.*, Oct. 2002, pp. 1669–1672.
- [62] R. Y. Chiao and X. Hao, "Coded excitation for diagnostic ultrasound: a system developers perspective," *IEEE Trans. Ultrason., Ferroelect., Freq. Contr.*, vol. 52, no. 2, pp. 160–170, 2005.
- [63] G. Cincotti, G. Cardone, P. Gori, and M. Pappalardo, "Efficient transmit beamforming in pulse-echo ultrasonic imaging," *IEEE Trans. Ultrason., Ferroelect., Freq. Contr.*, vol. 46, no. 6, pp. 1450–1458, 1999.
- [64] R. Y. Chiao and L. J. Thomas, "Ultrasonic imaging system with beamforming using unipolar or bipolar coded excitation," U.S. Patent 6,155,980, Dec., 2000.

Appendix A

Derivation of equation 2.3

Redraw Figure 2.4 and rewrite equation 2.2 as follows:

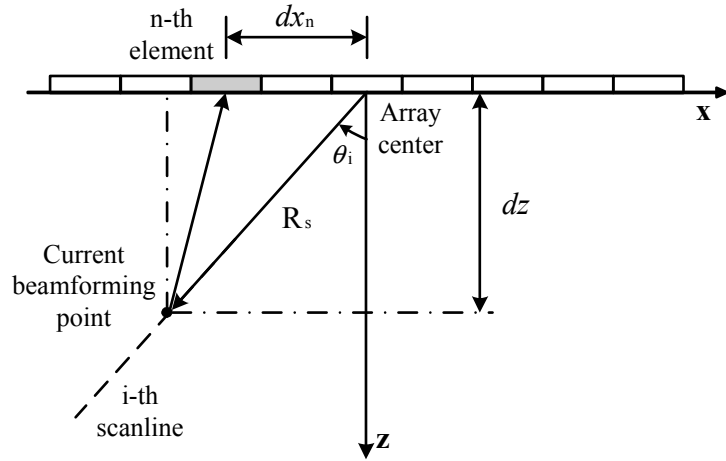


Figure A.1: Delay computation for receive beamforming

$$\tau_{n,abs} = (R_s + \sqrt{dz^2 + (R_s \cdot \sin \theta_i - dx_n)^2})/c , \quad (\text{A.1})$$

Let $f(x_n) = \sqrt{dz^2 + (R_s \cdot \sin \theta_i - dx_n)^2}$, thus equation A.1 can be denoted as:

$$\tau_{n,abs} = (R_s + f(x_n))/c . \quad (\text{A.2})$$

According to the Taylor series expansion:

$$f(x_n) = f(0) + f'(0) \cdot x_n + \frac{f''(0) \cdot x_n^2}{2!} + \dots, \quad (\text{A.3})$$

and notice that:

$$f(0) = R_s, \quad (\text{A.4})$$

$$f'(0) = f'(x_n)|_{x_n=0} = \frac{x_n - R_s \sin \theta}{\sqrt{x_n^2 + R_s^2 - 2x_n R_s \sin \theta}} \Big|_{x_n=0} = -\sin \theta \quad (\text{A.5})$$

$$f''(0) = f''(x_n)|_{x_n=0} = \frac{\sqrt{x_n^2 + R_s^2 - 2x_n R_s \sin \theta} - \frac{(x_n - R_s \sin \theta)^2}{\sqrt{x_n^2 + R_s^2 - 2x_n R_s \sin \theta}}}{x_n^2 + R_s^2 - 2x_n R_s \sin \theta} \Big|_{x_n=0} = \frac{\cos^2 \theta}{R_s}. \quad (\text{A.6})$$

Substituting A.4, A.5 and A.6 into A.3 yields:

$$f(x_n) \approx R_s - x_n \cdot \sin \theta + \frac{x_n^2 \cdot \cos^2 \theta}{2R_s}, \quad (\text{A.7})$$

in which higher order terms are neglected. Substituting A.7 into equation A.2 yields:

$$\tau_{n,abs} = (-x_n \cdot \sin \theta_i + \frac{x_n^2 \cos^2 \theta_i}{2R_s} + 2R_s)/c, \quad (\text{A.8})$$

which is exactly equation 2.3.

Appendix B

Derivation of equation 3.23

Redraw Figure 3.9(b) as follows:

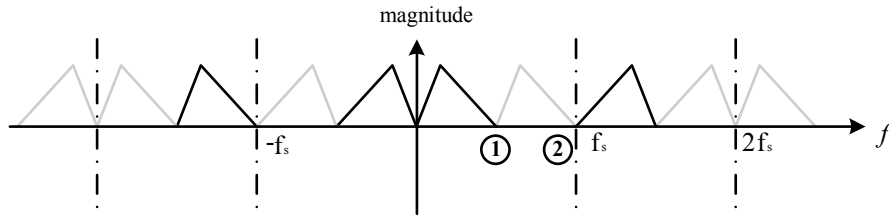


Figure B.1: Spectrum of the partial demodulated signal in heterodyning PRB with dark lines representing the spectrum of the original analog signal and gray lines representing the replicative spectra due to discrete time sampling

To avoid aliasing due to discrete time sampling, the spectral translation involved in the partial demodulation stage should comply with:

$$-f_H - f_r + f_s \geq f_H - f_L , \quad (\text{B.1})$$

$$-f_L - f_r + f_s \leq f_L + f_r \quad (\text{B.2})$$

at node ① and ② respectively as shown in Figure B.1. They can be rewritten as:

$$3 \cdot f_H - f_L \leq f_s \leq 2 \cdot (f_H + f_L) . \quad (\text{B.3})$$

Apparently, $3 \cdot f_H - f_L \leq 2 \cdot (f_H + f_L)$ should hold to make equation B.3 rational,

thus yielding $f_H \leq 3 \cdot f_L$ (*i.e.* a maximum fractional bandwidth of 100 %). Notice that $f_H + f_L = 2 \cdot f_0$ and $f_H - f_L = f_B$, equation B.3 can be rewritten as:

$$2 \cdot (f_0 + f_B) \leq f_s \leq 4 \cdot f_0 , \quad (\text{B.4})$$

subject to $f_H \leq 3 \cdot f_L$.